INFORMATION TO USERS

This manuscript has been reproduced from the microfilm master. UMI films the text directly from the original or copy submitted. Thus, some thesis and dissertation copies are in typewriter face, while others may be from any type of computer printer.

The quality of this reproduction is dependent upon the quality of the copy submitted. Broken or indistinct print, colored or poor quality illustrations and photographs, print bleedthrough, substandard margins, and improper alignment can adversely affect reproduction.

In the unlikely event that the author did not send UMI a complete manuscript and there are missing pages, these will be noted. Also, if unauthorized copyright material had to be removed, a note will indicate the deletion.

Oversize materials (e.g., maps, drawings, charts) are reproduced by sectioning the original, beginning at the upper left-hand corner and continuing from left to right in equal sections with small overlaps. Each original is also photographed in one exposure and is included in reduced form at the back of the book.

Photographs included in the original manuscript have been reproduced xerographically in this copy. Higher quality 6" x 9" black and white photographic prints are available for any photographs or illustrations appearing in this copy for an additional charge. Contact UMI directly to order.

UMI

A Bell & Howell Information Company
300 North Zeeb Road, Ann Arbor MI 48106-1346 USA
313/761-4700 800/521-0600

FROM PULSED TO CONTINUOUS WAVE CAVITY RING-DOWN SPECTROSCOPY

A DISSERTATION
SUBMITTED TO THE DEPARTMENT OF ELECTRICAL ENGINEERING
AND THE COMMITTEE ON GRADUATE STUDIES
OF STANFORD UNIVERSITY
IN PARTIAL FULFILLMENT OF THE REQUIREMENTS
FOR THE DEGREE OF
DOCTOR OF PHILOSOPHY

By
Barbara A. Paldus
May 1998

UMI Number: 9901568

UMI Microform 9901568
Copyright 1998, by UMI Company. All rights reserved.

This microform edition is protected against unauthorized copying under Title 17, United States Code.

UMI
300 North Zeeb Road
Ann Arbor, MI 48103

© Copyright 1998 by Barbara A. Paldus
All Rights Reserved

I certify that I have read this dissertation and that in my opinion it is fully adequate, in scope and quality, as a dissertation for the degree of Doctor of Philosophy.

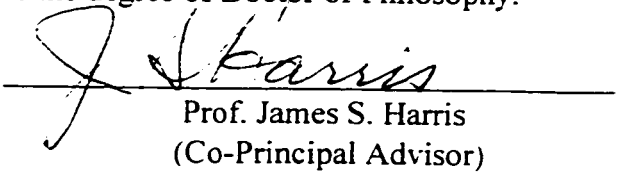

Prof. James S. Harris
(Co-Principal Advisor)

I certify that I have read this dissertation and that in my opinion it is fully adequate, in scope and quality, as a dissertation for the degree of Doctor of Philosophy.

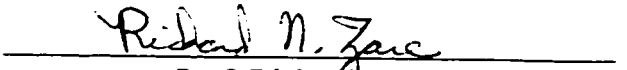

Prof. Richard N. Zare
(Co-Principal Advisor)

I certify that I have read this dissertation and that in my opinion it is fully adequate, in scope and quality, as a dissertation for the degree of Doctor of Philosophy.

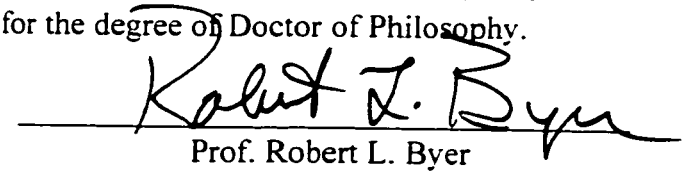

Prof. Robert L. Byer

I certify that I have read this dissertation and that in my opinion it is fully adequate, in scope and quality, as a dissertation for the degree of Doctor of Philosophy.

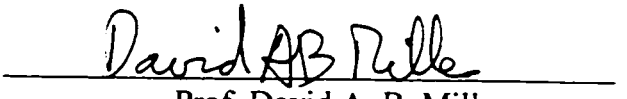

Prof. David A. B. Miller

Approved for the University Committee on Graduate Studies:

Abstract

Cavity ring-down spectroscopy (CRDS), a non-invasive, species specific, and spatially resolved laser-based spectroscopy, is a new entrant to the field of high sensitivity spectroscopy. In traditional CRDS, a pulse of laser light is injected into a high-finesse optical cavity, that is either empty (background), or contains the sample of interest. The rate of decay of light exiting the resonator is measured, and yields the resonator losses, which include absorption by the sample species. By measuring the ring-down rate as a function of wavelength, a spectrum of the sample can be obtained.

This thesis provides not only an overview of CRDS theory, including a novel scattering matrix approach to model second-order interference effects such mode beating, but also describes a series of fundamental experiments which illustrate the power and simplicity of pulsed laser CRDS, and the evolution of CRDS to new sensitivity limits using continuous-wave lasers. Laser and optical resonator stabilization schemes for optimum performance are presented for several different laser sources that have allowed sensitivity improvements of two orders of magnitude and will permit CRDS to reach its fundamental sensitivity limite: the shot-noise detection limit.

Preface

A strong need exists for high sensitivity, compact spectroscopic methods that can serve as diagnostics in situations ranging from trace pollutant detection, to studies of harsh environments exhibiting high temperatures and strong luminous backgrounds. Cavity ring-down spectroscopy (CRDS), a laser-based spectroscopy that is noninvasive, species specific, and spatially resolved, is ideally suited for trace gas detection. CRDS was first implemented in 1988 by Deacon and O'Keefe using a pulsed dye laser (P-CRDS), and used to detect weak vibrational overtones of molecular oxygen in the air. The number and diversity of CRDS applications in chemistry has seen phenomenal growth since its inception, owing mostly to its simplicity.

In P-CRDS, a pulse of laser light is injected into a high-finesse resonator that is either empty (for background measurement), or contains the sample of interest (for measurement of the desired spectrum). The rate of decay of light exiting the resonator is measured; this rate is directly proportional to the resonator losses, which include absorption by the desired species. By measuring the rate of decay as a function of laser source wavelength, a spectrum of the desired species is obtained. P-CRDS has several limitations: pulsed lasers are typically bulky and expensive; repetition rates of pulsed lasers rarely exceed kHz rates, making real-time spectral acquisition impossible; pulsed lasers have fundamentally broad linewidths, making high resolution P-CRDS difficult; and, light throughput in P-CRDS is very low, limiting sensitivity, especially in the infrared where few photon counting detectors exist. Because of these limitations of P-CRDS, in 1994 Lehmann proposed the concept of CW-CRDS, i.e. CRDS using continuous wave (CW) lasers.

This work focuses not only on applying CRDS to the detection of water vapor

in harsh environments (e.g., premixed methane-air flames), static environments (e.g., gas cells), and environments having many interfering species (e.g., ambient air), but also on furthering CRDS technology. A new theoretical approach to CRDS using scattering matrices has been implemented, which can account not only for multi-mode excitation of the resonator, but also for the effects of laser noise on the output ring-down signals. Fabry-Perot diode lasers stabilized via optical feedback were used for the first time to perform CW-CRDS. Such systems will enable compact, practical CW-CRDS systems to be realized in the future. CW-CRDS was also demonstrated using a ring resonator locked to an external cavity diode laser to eliminate potential sources of noise. Heterodyne detection of CRDS signals, as proposed by Levenson, has been investigated and produced a 30 dB improvement in signal-to-noise. This dissertation describes in detail the theory and experiments listed above.

Acknowledgements

Looking back on my years at Stanford, I do not know whom to thank first. This section is therefore but a feeble effort to show my appreciation to all who have made this work possible. I would like to thank Dr. J. S. "Coach" Harris for adopting me into his group, when my first advisor left Stanford at the end of my M. S. degree. Thanks to the Harris group 'open research environment', I was given the freedom to pursue an interdisciplinary research program, which resulted in this work. The self-motivation and self-guidance that I have learned have been an invaluable Ph. D. experience which I will always cherish. Secondly, I would like to thank Prof. R. N. Zare, my co-advisor, for making this research possible. Thanks to Prof. Zare's guidance, unflagging enthusiasm, and, above all, support, I was able to pursue a new direction in cavity ring-down spectroscopy, altogether different from his group's previous work. Thank you for believing in me, when I didn't believe myself. I am also grateful to Prof. A. E. Siegmann, Dr. M. D. Levenson, Prof. R. L. Byer, Prof. A. Schwettman, Prof. Y. Yamamoto and Prof. M. M. Fejer for teaching me to love lasers, optics, noise, and 'hero' experiments.

I would like to thank a number of present and past, Harris, Zare, and Byer group members for their seemingly unending patience, enthusiasm, support, and vision. Drs. P. Zalicki and Y. Ma first introduced me to the concepts of CRDS. Dr. C. W. Rella, Dr. G. Woods, and E. C. W. Lee, first suffered with me in trying to perform CRDS using a free-electron laser. Dr. J. Martin taught me a great deal about optical feedback effects in laser diodes, German precision engineering, and experimental spectroscopy in general. Dr. J. Xie showed me not only the joys of aligning and running OPOs but also the art of optimal and painless resonator alignment - thank you also for the

numerous CW-CRDS discussions! Dr. T. G. Owano and E. Wahl taught me about the analysis of flames and burners, the horrors of LabView, and especially how not to burn the lab building to the ground. All that I know about low-noise photodetector design, Pound-Drever locking, and not building my electronics on the floor, I owe to the instruction Dr. C. C. Harb, and all that I know about building and assembling monolithic ring resonators I learned from Dr. B. Willke. To both of you, thanks also for introducing me to the world of noise! I am grateful to Dr. T. G. Spence for all his sleepless nights spent in helping me acquire data, in performing the subsequent analysis, and for keeping me sane during the last few months of my degree. I would like to thank Prof. K. K. Lehmann, for his careful and critical review of all my preprints. I am grateful to P. Glorieux for helping me derive and understand the RDC theory presented here. Thanks also to W. Martin: UNIX guru, LaTeX guru, C++ guru, and how-to-take-apart-almost-anything guru. Also, many thanks to my office mates in both CIS and chemistry for putting up with my ever-messy desks. To all my other friends, classmates, roommates, qualsmates, and labmates, my sincerest thanks, and deepest apologies for not thanking you individually!

The administrative skills of Liz Edlund, Gail Chun-Creeck, Kelly Koucky, and Lu Miao were most helpful. The support and help of the CIS technical staff have not gone unappreciated: thank you all for the parts, the advice, the training, and most of all the unistrut cutting!

I am also grateful to both my reading and orals committees for taking the time to ponder over my work, to keep me honest, and to give me so much insightful feedback that shaped the final form of this thesis, and in bringing attention to the the many details that I would otherwise have overlooked.

The work for this dissertation was funded by the Advanced Research Project Agency through the Optical Material Center under contract # MDA972-94-1-0003, by the Department of Energy under contract # DE-FG03-92ER14303, by Office of Scientific Research in the Air Force, under contract # AF-F49620-97-1-0316, and a NSERC 1967 Centennial Fellowship.

I would like to thank my parents, Eva and Josef Paldus, and my god-parents,

Magda and William van Cleemput, for their unending love and encouragement, without which I would have given up long ago. Thanks for standing by me, especially in the trying times of the early years at Stanford. This thesis is dedicated to you.

Finally, I would also like to dedicate this thesis to my beloved grandmother, Zdena, and to my high school guidance counselor, Doreen Weis, who suggested engineering as a career in the first place. I cherish my memories of you, and will always keep the lessons that you taught me close to my heart.

Thanks to you all, and God bless!

Contents

Abstract iv

Preface v

Acknowledgements vii

1 Introduction 1

1.1 From Sunlight to Modern Linear Absorption Spectroscopy 1

1.1.1 The 17th Century: The Age of Newton 2

1.1.2 The 18th Century: The Age of Infrared and Ultraviolet Enlightenment 3

1.1.3 The 19th Century: Frauenhofer, Kirchhoff, and the Birth of Spectroscopy 4

1.1.4 Early 20th Century Spectroscopy 7

1.2 20th Century Technological Breakthroughs 9

1.2.1 The Laser 10

1.2.2 Semiconductor Integrated Circuits 11

1.2.3 Optical Coating Technology 13

2 Spectroscopic Analysis and Measurement 14

2.1 Absorption Spectroscopy 15

2.1.1 Fourier-Transform Spectroscopy 16

2.1.2 Laser Spectroscopy 19

2.1.3 Measurement Techniques 20

2.2 Ultrasensitive Absorption Spectroscopies 27
2.2.1 Multipass Cell Absorption Spectroscopy 28
2.2.2 Frequency Modulation Spectroscopies 30
2.2.3 Photoacoustic Spectroscopy 34

3 Basics of CRDS **35**
3.1 Overview of Linear Resonator Theory 35
3.1.1 Optical Resonator Stability and Modes 36
3.1.2 Transverse Modes 38
3.1.3 Longitudinal Modes 40
3.2 Introduction to CRDS Theory 41
3.2.1 A Simplistic View: The Bullet Model 41
3.2.2 A More Sophisticated View: RDC Transfer Functions 42
3.2.3 Some Notes on Mode-Matching 45
3.2.4 CRDS Experiments and Advantages 46
3.2.5 CRDS Sensitivity 47
3.3 Precursors of CRDS: Mirror Reflectometers 49
3.4 Pulsed Cavity Ring-Down Spectroscopy (PCRDS) 52
3.5 Continuous-Wave Cavity Ring-down Spectroscopy (CW-CRDS) . . . 57

4 Advanced Theory: Scattering Matrices **62**
4.1 Notation 62
4.2 Elementary Transmission Matrices 65
4.2.1 Mirrors 66
4.2.2 Absorbers 67
4.3 RDC Transmission Matrices 67
4.3.1 Propagation Method 67
4.3.2 Steady-State Approach 71
4.4 Simulations 73
4.5 Experimental Results 79

5 CRDS in Hostile Environments **82**
5.1 Apparatus and Experimental Method 83
5.2 Results and Discussion 86
5.3 Summary 94

6 CRDS using a Frequency-Stabilized Laser Diode **95**
6.1 AOM Stabilization of Laser Diodes 97
6.2 Apparatus and Experimental Method 99
6.3 Results and Discussion 102
6.4 Summary 107

7 Cavity-Locked Ring-Down Spectroscopy **109**
7.1 Cavity-Locked CW-CRDS 111
7.2 Experimental Setup 112
7.2.1 Ring Cavity CW-CRDS Optical Setup 112
7.2.2 Locking using the Pound-Drever-Hall Technique 117
7.3 Results and Discussion 119
7.4 Summary 125

8 Optical Heterodyne Detection in CRDS **126**
8.1 Experimental Setup 128
8.2 Results and Discussion 130
8.3 Summary 134

9 Conclusions **135**
9.1 Summary 135
9.2 Future Work 136
9.2.1 Shot-Noise-Limited Detection 136
9.2.2 Optical Locking 137
9.2.3 Access to Fundamental Transitions 137
9.2.4 Applications 138

Bibliography **139**

List of Tables

2.1 Light sources in the Ultraviolet. f=fixed frequency, t=tunable, CC=color center, PE=pulsed excimer, P=pulsed, CW=continuous wave, Semi=semiconductor 21

2.2 Light sources in the Visible. f=fixed frequency, t=tunable, CW=continuous wave, P=pulsed, Semi=semiconductor 23

2.3 Light sources in the infrared. f=fixed frequency, t=tunable, ion=argon or krypton ion laser, CC=color center, CW=continuous wave, P=pulsed, Semi=semiconductor. 26

2.4 Typical Intrinsic Detector Material [110]. DC=depends on composition. 27

2.5 Comparison of several ultrasensitive detection techniques. 28

4.1 Parameter set used in simulations of CRDS using a Gaussian input beam, for a typical physical system. HWHM=half width half maximum, t_{rt}=cavity round-trip time. 77

5.1 Line assignments for water vapor hot band transitions from (J,K_a,K_c) to (J',K_a', K_c'). 87

5.2 Line assignments for water vapor transitions (J,K_a,K_c) to (J',K_a', K_c'). Doublets are listed under one reference number; primes indicate weaker lines. 88

List of Figures

2.1 (a) Generic spectroscopes, and (b) a typical Fourier-Transform spectrometer. 18

2.2 Experimental setups for (a) multipass cell spectroscopy, (b) FM modulation spectroscopy, (c) intracavity laser absorption spectrosopy, and (d) photoacoustic spectroscopy. 29

3.1 (a) Linear optical resonator formed by two identical circular mirrors, having spherical curvature. These mirrors are characterized by their radius r_m, radius of curvature, r_c, and separation d. (b) Mode structure of linear optical resonator. (c) Stability diagram for optical resonator. 36

3.2 Laguerre-Gaussian modes for a spherical resonator. 37

3.3 (a) Bullet model of pulsed CRDS. (b) Frequency domain model of pulsed CRDS for Dirac delta function comb and Airy function comb . 41

3.4 Reflectrometry setups by (a) Herbelin *et al.* [29] for phase shift detection, (b) Anderson *et al.* [5] for decay-time detection, and (c) Rempe *et al.* [73] for decay-time detection. 51

4.1 (a) Linear system with 'input' and 'output' waves, and (b) linear systems notation conventions. 63

4.2 (a) Mirror transmission and reflection, and (b) absorption by a sample. 66

4.3 (a) Wave propagation mode, and (b) steady-state wave model. 69

4.4 (a) FT space excitation picture, and (b) magnitude of the input field (left top corner), magnitude of the output field (right top corner), magnitude of the input and output field for very small times where the output field is magnified 1000 times (left bottom corner), detail of the magnitude of the output field (right bottom corner). Only a single longitudinal and transverse mode is excited. 75
4.5 FT space excitation picture, and (a) magnitude of the input field (left top corner), magnitude of the output field (right top corner), magnitude of the input and output field for very small times shere the output field is magnified 1000 times (left bottom corner), detail of the magnitude of the output field (right bottom corner). Two longitudinal modes corresponding to a single transverse mode (TEM_{00}) are excited. . . . 76
4.6 (a) FT space excitation picture, and (b) magnitude of the output field (top), of an ideal detector, magnitude of the output field (middle) for a bad detector, detail (bottom) in time of the magnitude of the output field for a good (bottom waveform) and bad (bottom waveform) detector. Two transverse modes (TEM_{00} and TEM_{01}) corresponding to two longitudinal mode frequencies are excited. 78
4.7 (a) Setup for mode-beating demonstration, (b) experimental decays, and (c) resonator theory predicted mode-beating. 80

5.1 (a) Generation of near-infrared light in the master oscillator stage of an optical parametric oscillator; (b) experimental setup used to measure water vapor in a gas cell, in a propane torch flame and in a plane methane burner flame. 84
5.2 Schematic of Meker type burner used in flat flame experiment. 86
5.3 Spectra of water vapor in (a) a vacuum cell at 20 Torr and 300 K, (b) a propane torch flame at atmospheric pressure and 2000 K, and (c) a plane methane burner flame at atmospheric pressure and 5000 K. . . 89
5.4 Spectra of water vapor generated by a plane methane burner at (a) 0.12 cm, (b) 3.1 cm ,and (c) 10.0 cm above the burner grid. 90

5.5 Water vapor temperature as a function of distance from a plane methane burner grid. 91
5.6 Water vapor mole fraction as a function of distance from a plane methane burner grid. 92

6.1 (a) Linewidth for a free-running LD (solid) and for a LD under feedback (36 dB feedback) from a ring-down cavity (dashed). (b) LD linewidth as a function of external cavity length for only first order feedback: L_{ext} = 215 cm (solid), L_{ext} = 100 cm (dashed), and L_{ext} = 55 cm (dash-dotted). The feedback level is 50 dB in all three cases. (c) LD linewidth for only first order (50 dB) feedback (solid) and both first (50 dB) and zeroth (50 dB) order feedback (dashed). 99
6.2 Laser diode cavity ring-down spectroscopy setup using acousto-optic modulator feedback stabilization. 100
6.3 (a) LD linewidth as a function of wavelength (50 dB feedback), (b) LD spectral output at 813.2 nm (dashed) and 813.6 nm (solid). 103
6.4 Ring-down waveforms showing cavity throughput as recorded on (a) an oscilloscope (300 shots averaged) and (b) a multichannel scalar (5000 shots averaged). 104
6.5 Spectrum of (a) water vapor in room air and (b) 5 Torr water vapor in a cell previously evacuated to below 1 mTorr. Spectra based on HITRAN96 are shown as dashed lines. Weakest lines occur at p1 (813.391 nm) and p2 (813.452 nm). Transitions are labeled as (J',K_a',K_c') $\leftarrow$ (J,K_a,K_c). 106

7.1 CW-CRDS setup using a ring resonator locked to an external cavity diode laser source. 112

7.2 CW-CRDS experimental setup (a) optical system, and (b) cavity locking system. In (a) note the following abbreviations: AOM = acousto-optic modulator, BE=Beam Expander, BS= Beam Splitter, ISO = isolator, $\lambda/2$ = halfwave plate, L1= lens f=50 mm, L2 = lens f=1270 mm, L3 = lens f= 60 mm, PBS=polarizing beam splitter, PM = phaser modulator, PSP = polarization separation prism, WM = wavelength meter. In (B) note the follwing abbreviations: BPF = band-pass filter, HPF = high-pass filter, LPF = low-pass filter, PM=phase modulator, PZT = piezoelectric actuator, VCO = voltage controlled oscillator. . 114

7.3 (a) Frequency response of the mode cleaner cavity design obtained by sweeping the cavity length through one free spectral range, and (b) CCD images of transverse modes for unoptimized cavity allignment. . 118

7.4 Spectral Density of laser-cavity frequency fluctuation response for a locked system. 120

7.5 (a) Ring-down decays recorded on an oscilloscope with 2 shots and 256 shots, (b) residual from an exponential fit of a 256-shot waveform (magnified 100 times), (c) residual from a simulated exponential decay of a low-pass filter (magnified 100 times), and (d) dependence of $\sigma_{\ln \tau}$ on the number of shots averaged (measured =solid line, predicted = dashed line). 122

7.6 Spectrum of water vapor in room air obtained using a ECDL locked to the ring-down cavity. Spectrum based on HITRAN96 is shown in dashed lines. Weakest lines occur at 833.206 nm and 833.674 nm. Transitions are labeled as (J',K'_a, K'_c)$\leftarrow$ (J,K_a,K_c). 124

8.1 CRDS setup using (a) single detector or (b) dual differential heterodyne detection for RDC output signals. 128

8.2 Apparatus for heterodyne detection CRDS. The RDC is described in the previous chapter. 129

8.3 Three successive traces of the RF current amplitude on a linear scale. Note that the exponential decay of the field amplitude is twice that seen by direct detection. 131
8.4 Averages of 256 ring-down decays for direct detection and heterodyne detection with time scale of the latter halved to equalize decay times. The insert show signal power levels for unoptimized single detector heterodyne detection. For direct detection, the signal did not exceed the technical noise. 132
8.5 Spectrum of water vapor in room air obtained using a ECDL locked to the ring-down cavity, and single detector heterodyne detection. Spectrum based on HITRAN96 is showed in dashed lines, and transitions are indicated. 133
8.6 Signal-to-noise ratio of heterodyne detector signals for the single detector scheme and the dual detector schemes. 134

Chapter 1

Introduction

"The open society, the unrestricted access to knowledge, the unplanned and uninhibited association of men for its furtherance - these are what may make a vast, complex, ever growing, ever changing, ever more specialized and expert technological world, nevertheless a human community." - J. Robert Oppenheimer, *Science and the Common Understanding, 1953.*

Scientific developments do not arise from a vacuum, but can be placed within an historical framework, in which new technologies both motivate and facilitate experiments. Cavity ring-down spectroscopy (CRDS) resulted from the advent of high reflectivity mirror, laser, and semiconductor technology breakthroughs. The chapter that follows offers a cursory summary of historical events that led to linear absorption spectroscopy on which CRDS is based in particular, and to a general understanding of spectroscopy itself, in general.

1.1 From Sunlight to Modern Linear Absorption Spectroscopy

For millennia, sunlight and its refraction into colorful rainbows, must have appealed to the mysticism of primitive man. Beautiful, but untouchable and ephemeral, light was attributed a supernatural significance by even the most sophisticated ancient

civilizations. Claudius Ptolemy of Alexandria (A. D. 130), one of the early founders of optics and astronomy, was familiar with the measurement of angles of incidence and angles of refraction, but failed to discover the simple laws of refraction. The study of light, color, and refraction remained primarily limited by technology: all observations were performed with the unaided human eye, and consequently suffered from its physical limitations.

Glass was first discovered by the Phoenicians, but its use was confined to storage vessels and ornaments. It was not until the 14th century that the quality and clarity of glass improved to the extent that optical instruments could be built. In the 15th century, the properties of convex glass led to the development of lenses, spectacles, and telescopes. Simultaneously, the Jesuit orders began promoting an "age of learning": they laid the foundation for scientific inquiry, and empowered future scientists against the politics of the Church. Into this nascent scientific world were born Nicolaus Copernicus (1473-1543) and Leonardo da Vinci (1452-1519). Copernicus used the power of glass to build telescopes and observe the stars. He proposed the first heliocentric theory which ignited heresy trials of scientists by the Catholic Church that culminated in the sentencing of Galileo in 1633. It was for this reason that da Vinci shrouded his work in secrecy, which perhaps delayed significant advances in the optical sciences for several centuries. Da Vinci not only rediscovered refraction of light, but also discovered persistence of vision and the stereoscopic effect of human eyes. He challenged the ancient belief that the eye is the source of illumination for objects perceived. More important, he postulated that both light and magnetism were wavelike in nature, and reported the dispersion of white light into its spectrum of colors.

1.1.1 The 17th Century: The Age of Newton

Glass technology advanced significantly in the 17th century with the development of flint glass, a clear lead glass that could be polished into lenses. Thus, Robert Hooke (1635- 1703) and Antonie van Leeuwenhoek (1632-1723) were able to build the first microscopes, while Johannes Kepler (1571-1630) improved the telescope. With

better quality glass also came better measurements of refraction, which lead to the formulation by Willebrord Snell (1591-1626) that the sines of the angles of incidence and refraction have a constant ratio. Based on this work, humanity could observe both the vastness of space and the complexity of the microbiological world.

But it was not until Sir Isaac Newton (1642-1727) that the next step toward understanding the composite nature of white light was undertaken. In his treatises in the *Transactions of the Royal Society* (1672) and *Optiks* (1704), Newton described the first modern spectrometer that was capable of measuring the first solar spectrum: when he used a slit with a lens placed in front of a prism, a series of differently colored images of the the slit appeared on a screen in back of the prism. Had glass quality been somewhat better, it is not unlikely that Newton would have observed Frauenhofer lines in his spectrum. Despite these great advances, Newton failed to realize that atoms and molecules absorb or emit only at characteristic wavelengths. In stark contrast to Huygen's assertion that light behaves light waves (1690), Newton postulated that all flames were of the same nature because the light was produced by corpuscular vibrations, and delayed the understanding of spectra for at least another century.

Perhaps of equal importance to Newton's discoveries in optics, was the impact on science of the formation of scientific societies in Europe. Such bodies were established in England, France and Germany. Not only did these bodies introduce peer review of experimental results and theories, but they also disseminated results and elicited public interest (and royal patronage) for the pursuit of science.

1.1.2 The 18th Century: The Age of Infrared and Ultraviolet Enlightenment

Globally, the 18th century was an epoch more of war and revolution than scientific discovery. In the midst of the American War of Independence and the French Revolution, democracy as we know it was being born, while social change would begin to sweep Western society and lead to institutions of higher learning as we know then

today. The military became a patron for science, appreciating that scientific discoveries and technological advances were intimately linked. Scientists of the time were as much politicians and soldiers, as they were philosophers, and poets.

Two such men were John Dollond (1706-1761) and Benjamin Franklin (1706-1790). Dollond, while working to improve the quality of telescopes for the navy, invented the achromatic lens. By using two glasses, crown and flint, which had different indices of refraction, he was able to correct for chromatic aberration. Franklin, the American ambassador to France and one of the Founding Fathers, established that electricity was both positive and negative. This early discovery stimulated further scientific inquiry, which led to the experiments of Faraday (1791-1867), Wheatstone (1802-1875), and Edison (1847-1931), and that finally culminated in the formulation of electromagnetic theory by Maxwell (1831-1879). Without electricity, most spectroscopic instrumentation in use today would not function.

Little development occurred by way of spectroscopic analysis, except for the first description of an emission spectrum observed for a sodium flame by Thomas Melville in 1752. The important understanding that the optical spectrum is not limited to the visible region was gained only at the end of the 18th century. Sir William Herschel (1738-1822) studied the distribution of heat from the sun with an array of thermometers, each placed at a different color of the dispersed visible spectrum. Herschel thus discovered that most of the heat lay outside the visible spectrum, beyond the red: he had found the infrared. Almost simultaneously, Johann Wilhelm Ritter (1776-1810) was studying the effectiveness of the visible spectrum in blackening silver chloride. Ritter observed that that the action was strongest beyond the visible violet: he had found the ultraviolet.

1.1.3 The 19th Century: Frauenhofer, Kirchhoff, and the Birth of Spectroscopy

Spectroscopy in the 19th century began almost furtively, with only qualitative observations of emissions from flames, sparks, arcs, and the sun. At this time, astronomy

was the primary application of spectroscopy; several decades later, spectroscopic analysis would lead to the discovery of an element hitherto unknown on earth, helium, and to the formulation of the periodic table.

Thomas Young (1773-1829) observed a distinctive yellow line in the spectrum of candles, yet attributed this characteristic emission to interference effects. William Hyde Wollaston (1766-1828) observed dark lines that interrupt otherwise continuous solar spectra, but could not explain their origin. Countless others observed flame emission, but because their instruments were of poor quality, or the purity of their samples was inadequate, the fact that each atom and molecule has its own characteristic spectrum was not formulated until the arrival of Frauenhofer and Kirchhoff.

Joseph Frauenhofer (1787-1826), initially an apprentice to a mirror-maker, soon became the master optician of his time. While trying to define the color of light used in measuring the refractive index of glass in glass-making, he constructed a theodolite telescope which he placed behind a prism to view the images of a slit. In this manner, he observed "an almost countless number of strong and weak (dark) vertical lines" [3]. Because he could quantitate the angles in his experiment, he determined the relative line positions and developed a map of the solar spectrum. This map then served as a standard for the comparison of dispersion by different types and qualities of glasses. With all his measurements converted to 'wavelengths', Frauenhofer established one of the first spectroscopic standards. Only with a wavelength standard could scientists directly compare results obtained using different optical devices and make spectroscopic advances.

Frauenhofer also developed the first objective prism with which he observed the first stellar (Sirius) and planetary spectra. Furthermore, he discovered the transmission grating and thus observed the D-lines of sodium emission. Once he was able to manufacture transmission gratings of 3000 lines/cm with a diamond point and ruling machine, he measured the unresolved D-lines of sodium, and found that the yellow lines in sodium flames corresponded exactly in wavelength to the two dark lines in the solar spectrum.

This realization of a relation between emission and absorption spectra of light led to the formulation of a general law by Gustav Robert Kirchhoff (1824-1887), the

founder of spectral analysis: "The relation between the powers of emission and the powers of absorption for rays of the same wavelength is constant for all bodies at the same temperature" [43]. Kirchhoff was the first to articulate the significance of characteristic spectra emitted by different elements. He explained that the continuous nature of the solar spectrum was produced by emission from hot elements at the interior of the sun, while the dark lines were a result of absorption from this continuous emission spectrum by elements in the sun's cooler atmosphere. Not only did Kirchhoff completely map the solar spectrum but, with the aid of Robert Wilhelm Bunsen (1811-1899), he investigated many flame and spark spectra of very pure elements, and discovered both cesium and rubidium.

By the late 19th century, experimental spectroscopy exploded with new discoveries and theoretical formulations appearing almost every year. Although a complete listing1 of all these historical developments lies beyond the scope of this brief overview, we summarize a few important steps taken by scientists. The 1830's and the 1840's saw the creation of photographic film by William Henry Fox Talbot (1800-1877) and Jacques Daguerre (1789-1851), who developed a process to fix prints on paper soaked in silver nitrate. By 1870, Sir George Gabriel Stokes (1819-1903) had discovered that quartz is transparent in the ultraviolet, and photographic plates made of dry gelatine were being used by spectroscopists such as Élenthère Mascart (1837-1908) and Henry Augustus Rowland (1848-1901) to measure ultraviolet spectra to 2150 Å. By 1893, Victor Schumann had developed gelatin-free plates, fluorite optics, and evacuated chambers, so that ultraviolet spectroscopy extended beyond the absorption of oxygen to 1200 Å. A decade later, Theodore Lyman (1874-1954) extended the ultraviolet to 500 Åusing a concave grating of fluorite optics. In the 20th century, after numerous continual improvements to light sources, gratings and mountings by Robert Andrews Millikan (1868-1953) and Kai Manne Siegbahn (1918-), the ultraviolet limit was reduced to below 30 Å. Simultaneously, efforts were underway to extend spectroscopy to the infrared region. By the 1880's, Sir William Abney (1843-1920) had developed photosensitive plates that could record spectra to 200 μm, while Samuel Pierpont Langley (1834-1906) invented the bolometer, a sensitive electrical resistance thermometer that could measure radiation to 180 μm. Experimental spectroscopy, as

this historical moment, seemed to have no boundaries.

But the general problem of the lack of suitable standards for spectra was not fully resolved until the 20th century. Of the many standards devised, most of which were based on tabulations of Fraunhofer lines, each carried its own flaws. Anders Jonas Ångström (1814-1874) charted thousands of Frauenhofer line wavelengths, but his measurements were based on the Uppsala meter, which was later shown to be inaccurate. Henry Augustus Rowland (1848-1901) tabulated more accurate wavelength values by using a concave grating. Albert Abraham Michelson (1852-1931) used interferometers to measured highly accurate line wavelengths. But it was not until 1907 that the first spectroscopic standard was established by Charles Fabry (1867-1945) and Alfred Pérot (1863-1925): their interferometric measurement of the red cadmium line at 6438.4696 Åwas accepted by the International Union for Co-operation in Solar Research. Secondary standards based on rare-gas spectra were only adopted after World War I.

1.1.4 Early 20th Century Spectroscopy

In the early 20th century, spectroscopists and astronomers were busily occupied with their newly created spectroscopes and higher powered telescopes. Johann Jakob Balmer (1825-1898), Theodore Lyman (1874-1954), and Friedrich Paschen (1865-1947) had discovered that specific series of hydrogen lines could be represented by a simple mathematical formula, first found empirically by Rydberg (1854-1919). Pieter Zeeman (1865-1943) discovered magnetic splitting of spectral lines. Meanwhile, physical societies were struggling over a strange new theory called quantum mechanics. In 1900, Max Plank (1858-1947) had introduced the concept of quantized energy states leading to quantized transition energies. Five years later, Albert Einstein (1879-1955) introduced the idea that under certain circumstances light can behave like particles, called photons. Quantization then began to take root: Niels Henrik David Bohr (1885-1962) used it to develop early atomic theory and predict the energy levels of hydrogen. Max Born (1882-1970) applied it to the study of crystals, crystalline vibrations, and optical polarization.

Despite the vast tragedies of the first and second World Wars, an entire generation of young physicists including Erwin Schrödinger (1887-1961), Werner Karl Heisenberg (1901-1976), Louis-Victor-Pierre-Raymond deBroglie (1892-1987), Wolfgang Pauli (1900-1958), Samuel Abraham Goudsmit (1902-1978), Enrico Fermi (1901-1954), Edward Uehler Condon (1902-1974), Paul Adrien Maurice Dirac (1902-1984), Edward Teller (1908-), and Vladimir Alexandrovich Fock (1898-) (to name just a few!) not only fully adopted the ideas of quantum mechanics, but furthered them. They devised a wave theory, formulated the particle-wave duality of electrons and photons, formalized the Schrödinger equation, and developed the mathematics to 'solve' this equation for the energy levels of various physical systems. Yet, these theoretical advances were not made without experimental measurements. In 1887, Sir Joseph John Thomson (1856-1940) discovered the electron; in 1912, Ernest Rutherford (1871-1937) scattered alpha particles from atoms to demonstrate that atoms mainly consist of empty space; in the 1920's, Arthur Holly Compton (1892-1962) showed that photons can behave like particles and carry momentum, when he scattered x-rays from carbon films, and discovered that some of the x-rays had suffered 4% energy loss. Thus, by the end of the World War II, both the theoretical and the experimental stages were set for major advances in spectroscopy.

Some of the most important contributions to modern spectroscopy, based for the sake of brevity on a list of recipients of Nobel Prizes in chemistry and physics over the last six decades, follows. A more elaborate discussion of modern absorption spectroscopy techniques is presented in the next section.

- Sir Chandrasekhara Venkata Raman is most noted for his discovery of the Raman effect, the basis for present-day linear and nonlinear Raman spectroscopy, a powerful tool for the investigation of molecular vibrations and rotations. The advent of lasers has not only greatly enhanced the sensitivity of spontaneous Raman spectroscopy, but has led to new spectroscopic techniques based on the stimulated Raman effect, such as Coherent Anti- Stokes Raman Scattering (CARS).

- Willis Lamb Jr. is the father of saturation spectroscopy, which is based on the

velocity-selective saturation of Doppler-broadened molecular transitions. The spectral resolution then becomes only limited by the much narrower width of the Lamb dip. He was thereby able to determine the fine structure of hydrogen.

- Nikolay G. Bosov, Aleksandr M. Prokharov, and Charles H. Townes invented the maser that is ubiquitous in modern microwave spectroscopy experiments.

- Nicholas Bloembergen and Arthur L. Schawlow are noteworthy for devising laser spectroscopy, on which many modern spectroscopic studies are based.

- Gerhard Herzberg stands out among the chemistry Nobel laureates for his work in determining the electronic structure and geometry of molecules, and his contribution to spectroscopy of the three-volume *Molecular Spectra and Molecular Structure*[32]. His spectroscopic studies not only provided experimental results of prim importance to physical chemistry, but helped stimulated a resurgence of interest in chemical reactions of gases.

Spectroscopy now covers a sizable fraction of the electromagnetic spectrum. A more elaborate discussion of modern quantitative linear absorption spectroscopy is presented in later chapter. A plethora of other spectroscopies exist, but they are beyond the scope of this introduction. The reader is referred to the excellent treatments of Condon and Shortley [15] for atomic spectroscopy, of Herzberg [32] for molecular spectroscopy, of Schawlow and Townes for microwave spectroscopy [102], and of Levenson [51] for nonlinear spectroscopy. A compendium of spectroscopic techniques can be found in Demtröder [17].

1.2 20th Century Technological Breakthroughs

The evolution of optical science took a giant leap in the second half of the 20th century with the advent of the laser, the silicon-based semiconductor transistor and integrated circuit, the compound semiconductor optoelectronic photodiode and diode laser, the optical fiber, and a new generation of thin film optical coatings. Without these technological advances, cavity ring-down spectroscopy would not be possible

today. Ironically, the advances in optical coating technology, and a lack of suitable measurement techniques for highly reflecting mirrors, brought about the birth of cavity ring-down spectroscopy.

1.2.1 The Laser

"God said 'Let There Be Light!'
And Einstein planted a seed
Maiman created the laser one night
And sated man's optical need!" [111]

In the 1960s, a single crystal of ruby (sapphire grown with a small doping of Cr^{3+} atoms replacing Al atoms in the lattice) was shown to oscillate by Ted Maiman. This was the first demonstration of a three-level laser. An atom in the lowest energy state absorbed energy, became excited to the highest energy state, and decayed almost immediately into an intermediate state having a long lifetime. When a population inversion was built such that more atoms existed in the intermediate state than in the lower energy state, and a photon of the right wavelength passed through the crystal, stimulated emission of identical photons occurred, resulting in a spatially and temporally coherent beam of light exiting the crystal. Simply put, all photons exiting the laser were identical in energy, direction, polarization and phase to the photon used to provide the stimulation. By pumping the crystal at the correct rate to establish population equilibrium between the states, this 'lasing action' was sustained. Hence the name LASER: Light Amplification by Stimulated Emission of Radiation.

Since these early days, the laser has rapidly evolved and diversified into a multitude of light sources whose properties can be tailored to their application: pulsed or continuous wave output, different wavelengths and tuning ranges, and/or diverse output powers. There are lasers based on gas, solid-state crystal, liquid dye, even semiconductor material gain media. Laser emission wavelengths now vary from the vacuum-ultraviolet to the millimeter regions of the spectrum. These unique and useful sources of radiation and their application to spectroscopy will be discussed in greater detail throughout the remainder of this chapter.

1.2.2 Semiconductor Integrated Circuits

The germanium-gold transistor was invented in 1947 by John Bardeen, Walter H. Brattain, and Willian B. Schockley at Bell Laboratories in New Jersey, USA. Transistors, and their subsequent incarnations, are all made of crystalline semiconductor materials, whose electrical properties can be widely varied by the addition of impurities, called dopants. Electric current in semiconductors is carried both by electrons, and their analog, holes, which have effectively positive charge. This duality has been exploited in may electronic devices (e.g. MOSFET, JFET, bipolar transistors, etc.).

Success in purifying silicon led to silicon-based electronic devices in the 1960s. Owing to the low cost of silicon production and its material qualities, such as the simple growth of stable, adhesive oxides that can serve as masks for patterning many different devices onto a single silicon wafer, the integrated circuits (ICs) and electronics industries exploded in the 1970s and 1980s. Early ICs consisted of about 10 individual components and measured several millimeters; today, ultra-large-scale ICs measure several centimeters and comprise tens of millions of transistors.

The microprocessor and memory chips developed using ICs allowed computer engineers to design compact, low-cost microcomputers with sufficient computing power to perform even the most daunting business, medical or scientific tasks. The high-volume production and large consumer demand have promoted the use of microprocessors and microcontrollers in a vast array of applications, from household appliances to automobiles, and, of course, in most scientific instruments.

Spectroscopic measurements no longer require painstaking data acquisition by hand or manual computation. Most spectroscopic instruments already include computers, which allow real-time data acquisition and manipulation. Furthermore, electronics enable more accurate signal amplification and processing, as well as better photodetectors. Finally, computers also facilitate faster data interpretation and analysis, as well as faster dissemination of results. Spectroscopy and electronics will never be less intimately linked.

Optoelectronic Devices

In parallel to the growth and development of silicon technology have arisen optoelectronic devices based on compound semiconductor materials. Optoelectronic devices respond to, or generate, light: photodetectors and solar cells convert light (photons) into current (electrons); light-emitting diodes (LEDs) and diode lasers convert an applied voltage and current into light; optical fibers and waveguides help propagate light losslessly from one location to another; and optical amplifiers (fiber amplifiers) convert an optical pump to photons emulating an input optical signal.

Fabrication of optoelectronic devices relies on semiconductor materials formed by elements from column III of the periodic table (Ga, Al, In), and elements from column V (As, P, and Sb). Not only can these compounds be mixed together and produce crystalline materials having direct bandgaps (and thus capable of converting electrical energy into light and vice versa), but their properties can be subtly changed either through the material composition (stoichiometry) or through doping (group IV elements as C, Si). In fact, due to the similarities in crystal structure of different compositions, materials can be graded, even changed within a single crystal growth (e.g. by molecular beam epitaxy), and compositional changes controlled accurately on an atomic layer scale. Thus, laser diodes that emit at specific wavelengths can be designed and fabricated.

Developments in optoelectronics in the near-infrared have been spurred on by telecommunications applications, which have produced a plethora of inexpensive and readily available laser diodes between 650 nm and 1550 nm. Recently, memory and storage applications have resulted in laser diodes emitting in the ultraviolet to blue-green (370-500 nm) based on GaN. Fortunately for spectroscopists, the motivation of biological detection and environmental pollution monitoring have spurred research in compound semiconductors to produce diode lasers between 2 and 4 μm, and with the recent announcement of quantum cascade lasers, semiconductor optoelectronic lasers can now emit light from 5 μm to 15 μm as well. It is expected that these recent developments will soon be commercialized, thereby providing spectroscopists with inexpensive and readily available alternatives to gas, dye and solid-state lasers.

1.2.3 Optical Coating Technology

As high reflectivity mirrors became more important for many applications and optical instruments (e.g. high power lasers, gyroscopes, optical frequency standards), considerable efforts were made by the commercial manufacturers. Over the last decade, considerable progress was achieved in the development of superpolished, high purity substrates (surface roughness of angstroms), as well as in the growth of extremely low-loss thin-film dielectric coatings. Mirrors with losses on the order of ppm are readily available in the visible and near-infrared. Mirrors with several tens of ppm are available in the mid-infrared, and are expected to become available in the near future for the ultraviolet. Record reflectivities for these 'supermirrors' are 0.9999984, corresponding to losses of 1.6×10^{-6}, or 1.6 ppm.

Most high reflectivity coatings comprise at least 20 quarter-wave layer pairs of two layers having different indices of refraction. In the visible and near-infrared, layer composition is typically Ta_2O_5/SiO_2 [73]. In the ultraviolet, TiO_2/SiO_2 coatings, as well as oxides based on Os, Pt, and Rh, are under investigation [19]. In the infrared, materials having higher refractive indices are under investigation (and awaiting declassification) to reduce the necessary quarter-wave layer thickness used in the dielectric stacks. Different center wavelengths for a specific materials system are achieved by using different layer thicknesses and/or layer thickness gradation.

Typically, these oxide-based thin film dielectric layers are sputtered from high-purity oxide targets in a cryogenically pumped deposition chamber. Stoichiometric films are achieved with a carefully controlled, partially ionized oxygen backpressure in the chamber. Substrates typically undergo special chemical cleaning (e.g. ethanol and 1,1,1- trichloroethane) to minimize nonvolatile residue presence before deposition, and completed mirrors are stored in an inert atmosphere. It should be noted that these high reflectors require careful handling to prevent contamination by human contact (i.e. oils and water), and should be installed under clean conditions (i.e. a work bench with flowing, filtered air) to prevent the deposition of dust on the surfaces.

Chapter 2

Spectroscopic Analysis and Measurement

Spectroscopy is defined by the *Encyclopaedia Britannica* as "the study of the absorption and emission of light and other radiation by matter, as related to the dependence of these processes on the wavelength of the radiation."

Linear absorption spectroscopy has several requirement commont to other spectroscopies:

1. a sample that is confined to a predetermined volume with a specific pathlength,
2. a source of excitation (incoherent or coherent electromagnetic radiation) used to generate a characteristic response from the sample,
3. a means to resolve the sample response in wavelength, and
4. a detector used to sense the transmission through or emission from the sample.

Spectra represent either the emission from, or the absorption by a sample as a function of wavelength.

2.1 Absorption Spectroscopy

Absorption spectroscopy measures the loss of electromagnetic energy after it passes through a cell containing the sample under study. Atoms, ions, or molecules absorb radiation at specific wavelengths, λ_{ik}, that excite them from an allowed lower energy state, E_i, to an allowed higher energy state, E_k:

$$\lambda_{ik} = \frac{hc}{E_k - E_i} \tag{2.1}$$

Consequently, radiation at these characteristic wavelengths is attenuated at the exit of the sample cell. If the energy levels involved are both bound, the spectrum produced consists of discrete lines. If the upper energy state is above the dissociation limit or the ionization threshold of the sample, the absorption spectrum becomes continuous. Similarly, absorption within a continuous band is also possible wherever a high density of broadened lines exists in a given spectral region, such as commonly observed in liquids and solids.

Because each atom, and many molecules have unique and identifiable energy levels, a measurement of the attenuated wavelengths allows identification of the species present. According to the Beer-Lambert law, the transmitted intensity, $I_{trans}(\lambda)$ at the wavelength λ is related to the incident intensity $I_o(\lambda)$ by

$$I_{trans}(\lambda) = I_o(\lambda) exp(-\alpha(\lambda) l_{eff}), \tag{2.2}$$

where $\alpha(\lambda)$ is the absorption coefficient, and l_{eff} is the effective pathlength of the sample. For weak absorption, the first-order Taylor expansion of $exp(-\alpha(\lambda)l_{eff})$ yields $1 - \alpha(\lambda)l_{eff}$, so that the absorption coefficient can be computed from

$$\alpha(\lambda) = \frac{I_o(\lambda) - I_{trans}(\lambda)}{I_o(\lambda) l_{eff}} = \frac{\Delta I(\lambda)}{I_o(\lambda) l_{eff}}. \tag{2.3}$$

Clearly, the minimum-detectable concentration of absorbers for a specific absorption transition is inversely proportional to the effective sample pathlength and directly proportional to the minimum intensity fluctuation of the system.

Depending on the region of the electromagnetic spectrum used for excitation, different questions about a molecular or atomic structure can be answered. The present discussion will be limited to the optical spectrum, because a full treatment including x-ray and microwave radiation is not only beyond the scope of this introduction, but is presently not directly relevant to cavity ring-down spectroscopy. Spectroscopic sources will be assumed to be limited from the vacuum ultraviolet to the mid-infrared, i.e. from about 100 nm to about 30 μm.

The vacuum ultraviolet (< 200 nm) and near-ultraviolet (200-400 nm) regions involve photons whose energies are high enough to induce electronic excitation or to initiate photochemical reactions. Ultraviolet radiation is useful in studying σ- and π-bonded molecular systems. Species studied in this spectral region are diverse, and can range from organic molecules having multiple bonds (alkenes, dienes, polyenes, etc.), to atoms, ions, and radicals in both ground and excited states. The infrared (800 nm-20 μm) region is primarily associated with the internal vibrational and/or rotational motion of molecules. The 'fingerprint' region of the infrared (3 to 10 μm), where each molecule has a unique and identifiable spectral signature, is particularly useful in identifying species present in mixtures, or trace contaminants in the ambient atmosphere.

2.1.1 Fourier-Transform Spectroscopy

The classical spectroscope (cf. figure 2.1a) is an instrument that disperses different wavelengths from a broadband incoherent source into a spectrum for visual observation (eyepiece), while a spectrograph is an instrument that records the spectrum on an imaging device (photographic film, CCD array). In both instruments, the spectrum is sequentially scanned, and there is no frequency separation of the input light. Broadband light focused through a sample enters an aperture and passes through a set of imaging optics before being dispersed (by a prism or grating) and directed, one wavelength at a time, onto the imaging system. The resolution of the spectra thus obtained depends on the power of the instrument to spread different wavelengths into different angles (angular dispersion), resulting in a displacement (linear dispersion)

at the imaging point.

Spectrometers and spectrographs are still in use today for emission spectroscopy, but are often replaced with Fourier-transform (FT) spectrometers for direct absorption spectroscopy. In fact, FT spectroscopy is one of the most widely used analytical techniques in modern industry and research, with the possible exception of chromatography and mass spectrometry, because it allows absorption spectra to be obtained with wide spectral coverage in a matter of minutes. Spectra of a broadband light source are obtained by first generating and recording an interferogram with a scanning Michelson interferometer (c.f. figure 2.1b), and then inverting the interferogram by means of a cosine Fourier transform.

In the scanning Michelson interferometer, half of the incoming light is transmitted by a beamsplitter to a stationary mirror, while the other half reaches a moving mirror. The two beams are then recombined on the beamplitters, are focused onto a sample, and are simultaneously collected by a detector. Because the two beams have equal amplitude and common coherent origin, but their wave fronts propagate along different optical path lengths, they interfere when they are recombined. This interference can be controlled by scanning the moving mirror, and the resulting intensity variation in the recombined output beam, as a function of relative time delay between the beams, yields the interferogram. It can mathematically shown [19, 17] that the spectrum can be computed from the cosine FT of the interferogram.

The principal advantage of FT spectrometers over classical ones is that all the frequencies in the source are modulated simultaneously into a single interferogram signal, reducing scan times and sensitivity to mechanical vibration in the instrument during a scan. Furthermore, by exploiting the computational power of modern computers and using discrete FT techniques, the wavelength resolution of FT spectrometers can be dramatically improved.

Sources for FTS in the infrared include a tungsten-filament lamp heated to 2800 K that provides a strong continuum from the visible to about 1.5 μm, and a Globar, a silicon carbide element heated to 1400 K that provides mid-infrared radiation from 1.5 to at least 50 μm. Sources for FTS in the ultraviolet can either use synchrotron radiation, laser-produced plasmas (few torr of a rare earth such as Yb and

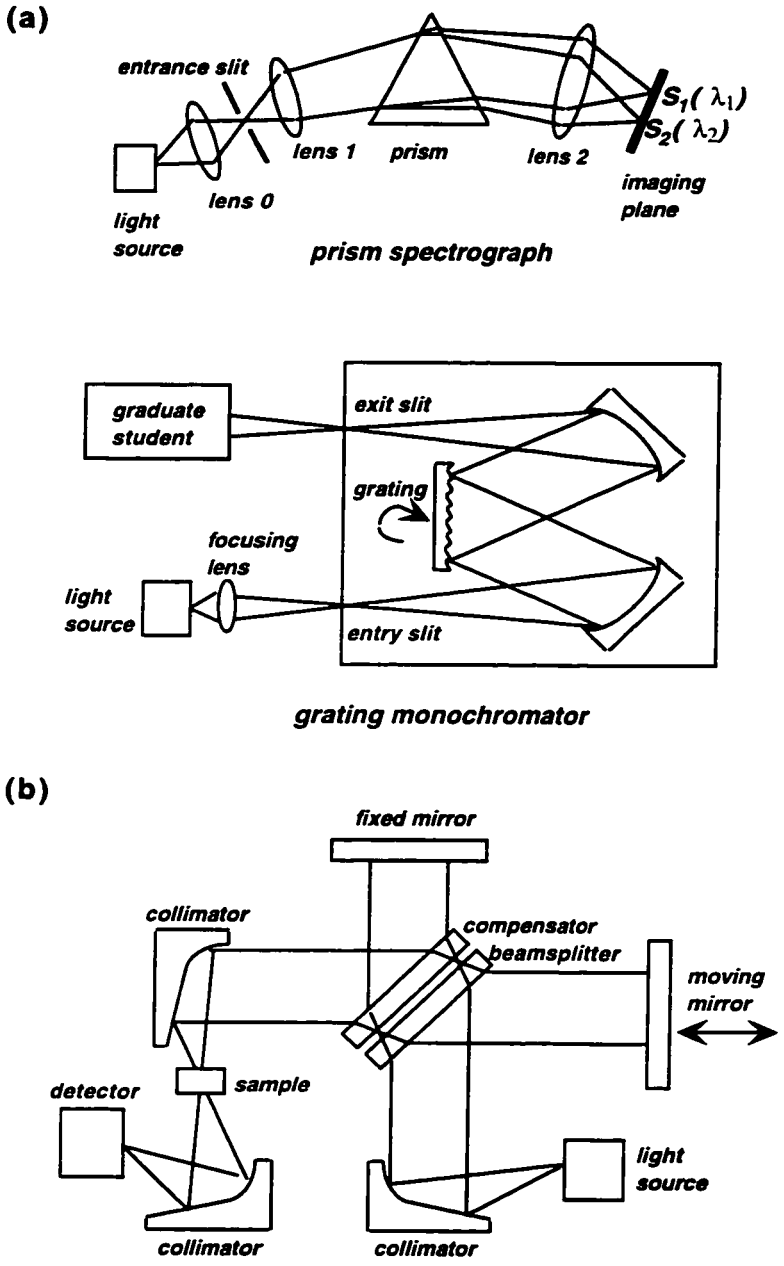

Figure 2.1: (a) Generic spectroscopes, and (b) a typical Fourier-Transform spectrometer.

Sm, or W, Pb and Hf), hydrogen and deuterium discharges (165-350 nm), or supercontinuum generation (focusing femtosecond laser pulses in both liquids and noble gases). Materials typically used to build the interferometers are listed in the section on measurement techniques. The physical principles of FTS instrumentation remain independent of the spectral region of interest.

FT spectrometers, however, do have their disadvantages and limitations and are by no means the panacea for all spectroscopic applications. Precise dynamic alignment of the interferometer using a reference laser and mirror servo-control can be difficult; and moving the scanning mirror with a uniform velocity in the presence of vibrations is far from trivial. Furthermore, typical wavelength resolution is limited to about 0.001 cm^{-1} for a slit separation on the order of tens of μm.

2.1.2 Laser Spectroscopy

A comparison between conventional absorption spectroscopy, based on incoherent radiation sources, and laser absorption spectroscopy is presented here. This discussion will be confined to methods where spectral resolution is limited by the Doppler broadening of molecular absorption lines. It should be noted, however, that there exist numerous nonlinear laser spectroscopic techniques (e.g. Doppler-free two-photon spectroscopy, Doppler-free laser-induced dichroism spectroscopy) that allow sub-Doppler spectroscopy. For a comprehensive discussion of laser spectroscopy techniques, the reader is referred to books by Demtröder [17] and Levenson [51].

In a conventional absorption spectrometer using a broadband, incoherent radiation source, the wavelength resolution is determined by the resolving power of the spectrometer. Laser spectroscopy uses coherent light sources, whose linewidths can be made extremely narrow and whose spectral densities can be made many orders of magnitude larger than those of incoherent sources. The advantages of laser spectroscopy are as follows:

1. For laser linewidths narrower than the absorption feature, the absorption spectrum can be directly obtained by scanning the laser through the desired feature; a monochromator is no longer necessary.

2. Spectral resolution is higher than in conventional spectroscopy owing to the narrow linewidths, and spectral profiles can be determined with greater accuracy.

3. Detector noise becomes negligible for sufficiently large spectral power densities.

4. Methods can be devised to suppress laser intensity fluctuations; such suppression increases the signal-to-noise ratio and improves sensitivity.

5. That laser light, being coherent, can be collimated, which allows the use of long pathlength absorption cells and results in increased sensitivity.

6. The laser frequency can be locked to the center of an absorption line in order to measure the line's center wavelength with unprecedented accuracy (1 part in 10^{14}).

Laser spectroscopy is therefore ideally suited for the spectroscopy of weak transitions and for measurements of ultralow concentrations. Because laser sources are becoming more reliable, less expensive, and more compact, the potential of laser spectroscopy for practical applications in industry and medicine continues to increase. However, the sensitivity of traditional direct absorption techniques is restricted by fluctuations in the intensity of the light source employed which limits the sensitivity of these techniques to 1 part in 10^4.

2.1.3 Measurement Techniques

A brief overview of the basic components needed for spectroscopic experiments is presented for each spectral region. A more complete review of the development of high reflectivity mirror coatings, specific to cavity ring-down spectroscopy, was given in the previous technology section.

The Ultraviolets: Vacuum Ultraviolet (VUV) and Near-Ultraviolet (NUV)

VUV and NUV radiation is typically generated as pulses. Coherent light sources include: pulsed lasers (listed in table 2.1), excimer lasers (see table 2.1), and nonlinear

Table 2.1: Light sources in the Ultraviolet. f=fixed frequency, t=tunable, CC=color center, PE=pulsed excimer, P=pulsed, CW=continuous wave, Semi=semiconductor

Laser Type	λ (nm)	Tune	Notes
Ar_2	126	f	PE, gas discharge
Kr_2	146	f	PE, gas discharge
ArCl	170	f	P: gas discharge
Xe_2	173	f	PE, gas discharge
ArF	193	f	P: gas discharge
KrCl	222	f	P: gas discharge
KrF	248	f	P: gas discharge
XeBr	282	f	P: gas discharge
XeCl	308	f	P: gas discharge
N_2	337.1	f	P: gas discharge
XeF	351, 353	f	P: gas discharge
Ar^{+2}	351.1, 363.8	f	CW: gas discharge
Kr^{+2}	350.7, 356.4, 406.7	f	CW: gas discharge
BBO	250-400	t	P: Nd:YAG pump
CC (F^+)/CaO	360-400	t	CW: argon ion pump
GaN	370-440	t	CW:Semi pn junction

optical techniques (second harmonic generation and sum- frequency mixing in BBO crystals, or stimulated anti-Stokes Raman scattering in molecular gases as hydrogen, nitrogen or methane). Recently, commercial edge-emitting laser diodes based on GaN, and emitting between 370 and 440 nm have been announced, and GaN vertical cavity surface-emitting laser diodes (VCSELs) are on the commercial horizon for 1999.

There is a wide assortment of photon detectors with useful response and sensitivity in the VUV and NUV. Both VUV and NUV detectors are based on the same principle, and are similar to their visible and near-infrared counterparts: a response is initiated by surface photoemission, electron-hole pair generation in semiconducting materials, or chemical reactions in photographic emulsions. VUV detectors with single photon counting capabilities are widely available [37, 95]. Typical detectors include: photographic plates, photomultiplier tubes, vacuum photodiodes, multichannel plate detectors, silicon photodiodes, charge-coupled devices, and ionization chambers.

A comparison of detector performance, and a general summary of photon detector technology are given in reference [59].

Optical materials for the VUV and NUV are dictated primarily by their transmission properties. Transmission through bulk materials typically limits wavelengths to remain above 105 nm, the short wavelength transmission limit of LiF. Metal surface reflectance decreases dramatically at short wavelengths, so that polarizers and narrow-band interference filters become difficult to manufacture because few materials have suitable optical constants. The most common substrate materials (windows, mirrors, lenses) are quartz or Suprasil ($\lambda > 160$ nm), sapphire ($\lambda > 145$ nm), calcium fluoride ($\lambda > 125$ nm), magnesium fluoride ($\lambda > 112$ nm), and lithium fluoride ($\lambda > 105$ nm). Transmission polarizers are usually based on the birefringence of magnesium fluoride. Gratings used are based on the Eagle, Wadsworth, or Seya-Namioka designs [106].

The Visible (VIS)

In the visible (400-800 nm), a plethora of pulsed and continuous-wave (CW) laser sources exists. Approximate tuning ranges for fixed frequency and tunable lasers are given in table 2.2, and have been adapted from reference [19]. An excellent source for useful lasers dyes in the visible can be found on p. 11 of reference [51]. Pulsed lasers (e.g. dye and alexandrite), with the exception of optical parametric oscillators (OPOs), tend to exhibit multimode emission in general, unless mode-selective elements such as etalons are introduced into the laser cavity. Pulsed laser linewidths typically vary from about 100 MHz (for OPOs at the Fourier-transform limit given nanosecond pulses) to several GHz (dye lasers); pulse repetition rates vary from about 10 Hz to a few kHz; and, pulse energies can exceed several mJ for nanosecond long pulses.

CW-laser performance is directly related to its tunability. Fixed frequency gas or solid state lasers can have large output powers (several W for argon ion to several kW for Nd:YAG), and can be used to pump tunable solid-state lasers such as Ti:Sapphire, Alexandrite, or dye lasers. Optically pumped tunable lasers typically exhibit large output powers (> 100 mW), but tend to be expensive and bulky. On the other side

Table 2.2: Light sources in the Visible. f=fixed frequency, t=tunable, CW=continuous wave, P=pulsed, Semi=semiconductor

Laser Type	λ (nm)	Tune	Notes
Ar^+	488.0, 514.5	f	CW, gas discharge
Kr+	568.2, 647.1	f	CW, gas discharge
HeNe	623.8	f	CW, gas discharge
Cr^{+3}-Ruby	694.3	f	P: flashlamp
Dye Solution	323-800	t	CW: ion laser pump
Alexandrite	700-820	t	CW: ion,Nd:YAG pump
Ti^{+3} : *Sapphire*	680-800	t	P:Nd:YAG; CW: ion,Nd:YAG pump
KTP-OPO	710-910	t	P:Nd:YAG
PPLN-OPO	400-700	t	P/CW: Nd:YAG, diode, fiber pump
GaN	400-550	t	CW:Semi pn junction
GaAsP	550-880	t	CW:Semi pn junction
AlGaAs,AlGaAs/GaAs	720-880	t	CW:Semi pn junction
InGaAlP/GaAs	630-700	t	CW:Semi pn junction

of the CW laser gamut are diode lasers and their optically stabilized external cavity diode laser counterparts, fabricated using III-V compound semiconductor materials. These diodes tend to be small, inexpensive, and readily available. They are tuned electronically, either by current or temperature control. Finally, CW lasers are similar in their modal purity to their pulsed counterparts: a frequency-selective element is required to obtain single-mode emission. However, unlike their pulsed counterparts, CW lasers offer an advantage in the time bandwidth product for long measurement times, so that linewidths of a few MHz, or even as low as a few 100 Hz, are achievable for free-running systems.

A multitude of different detectors exists for visible radiation. The specific choice of detector will depend on the exact experimental conditions at hand. An excellent survey of detectors is given in reference [110]. Typical detectors include: photographic film, photoelectric detectors fabricated from semiconductor materials such as photodiodes, avalanche photodiodes, vacuum phototubes, photomultipliers, and photoconductors, thermal detectors such as thermocouples, thermopiles, bolometers and

thermistors, and pyroelectric detectors. Electronic requirements for these photodetectors vary from several volts for photodiode detectors, to several hundred volts for avalanche photodiodes, phototubes and photoconductors, to several thousand volts for photomultipliers and bolometers. Typical detector bandwidths range from MHz to GHz. For weak signals, electronic amplification is usually necessary.

Optical materials for the visible (e.g. windows, lenses, beamsplitters, polarizers) must be transparent, fully dense, and pure to ensure low absorption and low scattering losses (< 0.1 cm^{-1} for low power applications; < 0.001 cm^{-1} for high power applications). Materials must also have sufficient uniformity in index of refraction to reduce beam distortion. Index uniformity is typically achieved best by single crystals (e.g. calcium fluoride, sapphire, calcite), followed by glasses (e.g. BK-7, Infrasil, Suprasil, Synsil, Homosil, etc.). For mirror applications, another important criterion of choice is the thermal expansion coefficient of the substrate, to ensure that the mirror maintains its optical figure precisely during use (e.g. BK-7 for typical applications, silica with 7.5% titanium dioxide for high precision applications). Thin film coatings for reflectors, filters, attenuators, beamsplitters, or simply protection are widely available, and are now highly developed for the visible region to provide satisfactory performance. Quartz serves as an excellent material for polarizing optics. Nonlinear optical materials used in acousto-optic or electro-optic modulators, include lithium niobate and quartz. For a complete list of available materials, the reader is referred to reference [110].

The Infrareds: Near-Infrared (NIR) and Mid-Infrared (MIR)

In the near-infrared (800-2,000 nm) and mid-infrared (2-20 μm), a plethora of pulsed and continuous-wave (CW) laser sources exists. Approximate tuning ranges for fixed frequency and tunable lasers are listed in table 2.3, and have been adapted from reference [19]. An excellent source for useful lasers dyes in the NIR, and color center lasers in the NIR and MIR can be found on p. 11 of reference [51]. Pulsed lasers exhibit similar behavior to those found in the visible, except that pulse energies decrease to below several mJ for nanosecond pulses with increasing wavelength.

CW-laser performance is also similar to that in the visible: optically pumped

tunable color center lasers, and electronically controlled lead salt lasers typically exhibit larger output powers, but tend to be expensive, bulky, and difficult to operate in single-mode. Most lasers emitting beyond 2 μm require cryogenic cooling, ranging from triple Peltier stacks to liquid nitrogen dewars. CW diode lasers, despite their limited tuning range and output powers remain fairly simple to operate, and are tuned with current and temperature control. A newcomer to this list is the quantum cascade laser, which is presently only in the developmental stage: it can emit several tens of mW of MIR light, with linewidths of several MHz. CW laser linewidths achievable for free-running systems, however, range from several MHz to several tens of MHz.

For infrared light detection, photoelectric detectors as photoconductors and photodiodes, or thermal detectors such as thermopiles, bolometers and thermistors can be used. Although silicon (germanium) detectors operate both in the visible and the NIR, for most MIR detectors, the material, responsivity and operational requirements change dramatically. In the MIR, size, operating temperature, physical configuration, vibration, and background electromagnetic radiation can all affect detector response and noise. Thermal (Johnson) noise limits the infrared wavelength response, so that detectors operating in the MIR require cooling, either electrically by Peltier coolers, or with liquid nitrogen, to ensure that $kT << E_g$, i.e. the thermal noise is much smaller than the material bandgap. Eventually with any material, however, photons at a sufficiently large wavelength will have an insufficient energy to excite free carriers, and thus elicit a detector response. Table 2.4, obtained from reference [110], shows typical detector material responses. For the MIR, detector response is usually much slower, usually no faster than 50 MHz, while responsivity depends on temperature.

Optical materials used in the NIR are identical to the visible. Once again, however, as the operational wavelengths increase beyond 2 μm, different materials must be used to achieve the desired optical properties. Typical substrates used in the infrared include silicon, zinc selenide, sapphire, cesium iodide, calcium fluoride, and chalcogenites, owing to their low absorption losses. Several specialty glasses (e.g. ULTRAN30, IRG2, IRG11, and Ig2n2919) have also been extended for use in the infrared up to about 8 μm. For applications beyond 10 μm, cadmium telluride and the cesium halogens can be used. It should be noted, however, that these materials,

Table 2.3: Light sources in the infrared. f=fixed frequency, t=tunable, ion=argon or krypton ion laser, CC=color center, CW=continuous wave, P=pulsed, Semi=semiconductor.

Laser Type	λ (nm)	Tune	Notes
Dye Solution	800-1200	t	P:flashlamp pump;CW:ion pump
Ti^{3+} : *Sapphire*	800-1100	t	P:Nd:YAG; CW:ion,Nd:YAG pump
CC (F_2^+)/LiF	820-1050	t	CW:ion pump
CC (F_2^+)*/NaF	990-1220	t	CW:ion pump
CC (F_2^+)/KF	1220-1500	t	CW:ion,Nd:YAG pump
CC (F_2^+)/NaCl	1400-1750	t	CW:ion,Nd:YAG pump
CC ($Tl^0(1)$)/KCl:Tl	1400-1600	t	CW:ion,Nd:YAG pump
CC (F_2^+)/NaF	990-1220	t	CW:ion,Nd:YAG pump
Nd^{3+}:YAG	1065, 1300	f	CW:lamp,laser diode
Er^{3+}-glass	1536,1543,1550	f	CW:lamp,laser diode
InGaAlAs/GaAs	800-1100	t	CW:Semi pn junction
GaAs	840-900	t	CW:Semi pn junction
InGaAsP/InP	1200-1650	t	CW:Semi pn junction
InP	900	t	CW:Semi pn junction
CC (F_B(II))/KCl:Na	2220-2740	t	CW: dye pump
CC (F_A(II))/KCl:Li	2300-3100	t	CW: krypton ion, Nd:YAG pump
CC (F_A(II))/RbCl:Li	2500-3650	t	CW: krypton ion, Nd:YAG pump
CC $(F_2^+)_A$/KI:Li	2380-3990	t	P: 1730 nm pump
InPAs	900-4000	t	CW: Semi pn junction
GaInAs	906-3100	t	CW:Semi pn junction
InAs	3100	t	CW:Semi pn junction
Xe	3507	f	CW: gas discharge
PbS	4300	t	CW:Semi pn junction
InSb	5200	t	CW:Semi pn junction
PbTe	6500	t	CW:Semi pn junction
PbSe	8500	t	CW:Semi pn junction
PbSnSeTe	4000-15000	t	CW:Semi pn junction
BBO OPO	3000-8000	t	P: Nd:YAG pumped
CO_2	10600	f	CW:gas discharge,dynamic
Quantum Cascade	5400 - 15400	t	P/CW:Semi interband

Table 2.4: Typical Intrinsic Detector Material [110]. DC=depends on composition,

Material	Bandgap (eV)	Temperature (K)	Usable λ range (μm)
Ge	0.67	193	0.9-21.9
Si	1.12	300	0.2-1.1
GaAs	1.5	300	0.4-0.9
InGaAs	DC	300	0.9-1.7
InGaAsP	DC	300	1.0-1.6
PbS	0.42	300	1.1-3.5
PbSe	0.23	300	1.0-5.0
InSb	0.18	77	2.0-5.5
HgCdTe	DC	77	8.0-14.0
PbSnTe	DC	77	8.0-11.5

as well as mid-infrared thin film coatings, are presently nonstandard for most optics manufacturers. Quartz remains a good material for nonlinear optical applications such as acousto-optic modulators. A more detailed description of specific crystalline and glass materials can be found in reference [110].

2.2 Ultrasensitive Absorption Spectroscopies

Over the past decade, alternative approaches to Fourier-transform spectroscopy have become extremely sensitive. Trace gases, such as pollutants, can be measured in minute quantities. Single atoms or different isotopes of the same atom can be detected among 10^{20} atoms of different species. Frequency shifts as small as one part in 10^{14} [116] of the frequency being measured can also be detected with ultrahigh resolution laser techniques.

Ultrasensitive detection methods all strive to increase the effective pathlength while minimizing the smallest detectable absorbance. These methods include multipass cell absorption spectroscopy, frequency modulation spectroscopy, intracavity laser absorption spectroscopy, and photoacoustic spectroscopy.

In table 2.5 , a comparison of various absorption spectroscopies is presented and compared with pulsed cavity ring-down spectroscopy (P-CRDS) and continuous-wave

Table 2.5: Comparison of several ultrasensitive detection techniques.

Spectroscopy	MDAL (cm^{-1})	Cost	Complexity
Single-Pass	10^{-6}	cheap	simple
Multipass	10^{-8}	moderate	straightforward
ICLAS	10^{-6}-10^{-11}	expensive	difficult
FM	10^{-6}-10^{-8}	moderate	moderate-difficult
P-CRDS	10^{-6}-10^{-10}	moderate	simple
CW-CRDS	10^{-10}-10^{-12}	cheap-moderate	simple-difficult

cavity ring-down spectroscopy (CW-CRDS). Which type of absorption spectroscopy is most suitable for a given application depends on factors such as cost, complexity, and sensitivity needed.

2.2.1 Multipass Cell Absorption Spectroscopy

Multipass cell absorption spectroscopy improves the detection sensitivity by increasing the *effective* pathlength through the sample. For a fixed volume, the light path can be folded around the input and output surfaces of the cell many times, thereby yielding an effective path through the sample cell that is many times the sample cell length. Multipass absorption spectroscopy typically can achieve single-shot minimimum detectable absorbances on the order of 10^{-5} to 10^{-7} cm^{-1} with direct detection [13].

Multipass cells (cf. figure 2.2a) that increase pathlength by a factor of 10 to 1000 are readily available. It is even possible to obtain meter-long multipass cells that have effective pathlengths up to a kilometer, but these special cells are expensive and require very stable operating temperatures to ensure that mirror shape and separation do not change. Two commonly used cells are White cells [113], where the beam is refocused to the same spot size on each roundtrip and light enters in one end and leaves at the other, and Herriot cells [31], where the beam circulates in a near-concentric optical cavity and light enters and leaves through the same hole in one of the mirrors.

The temperature stability requirement arises from the fact that most multipass

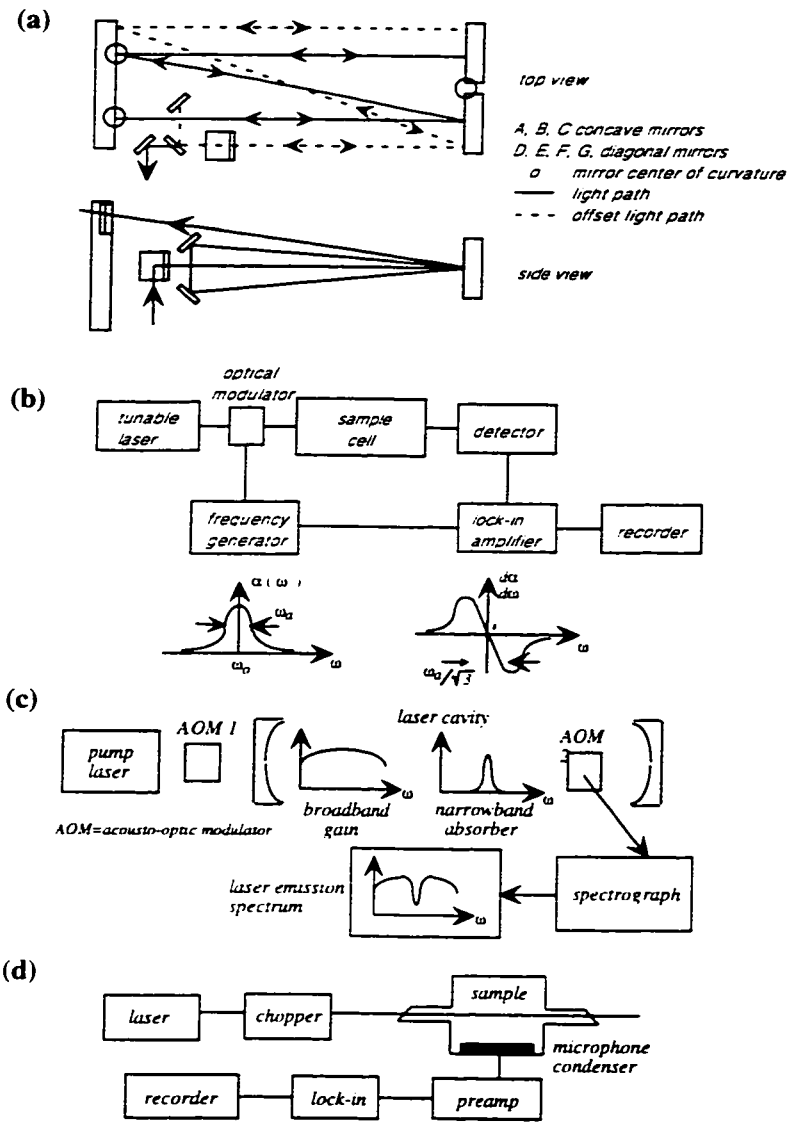

Figure 2.2: Experimental setups for (a) multipass cell spectroscopy, (b) FM modulation spectroscopy, (c) intracavity laser absorption spectrosopy, and (d) photoacoustic spectroscopy.

cells have large mirror surfaces to maximize cell throughput (i.e. have a small ratio of focal length to aperture) and are placed so that the optical cavity formed is at the stability boundary. Hence any change in cavity length will perturb the ability of the cell to refocus the beam at each pass, leading to a diverging beam and a loss in cell throughput. Furthermore, maintaining the geometry of each mirror is important, as the number of beam spots on the mirror determines the effective pathlength, and any fluctuations in effective pathlength translate into measurement noise in the effective absorbance, and reduce the system sensitivity. In all multipass cells, mirror reflectivity affects the maximum possible achievable pathlength because light is lost at each reflection, and mirror size affects the overall path length achievable because each beam spot must be spatially resolved from all others along the beam path to prevent interference effects. Even with this gain in pathlength, multipass absorption spectroscopy is ultimately limited by intensity fluctuations in the light source.

2.2.2 Frequency Modulation Spectroscopies

Even in direct absorption spectroscopy, it is well-known that sensitivity can be improved by amplitude modulation of the CW light source and lock-in detection at the modulation frequency. Lock-in detection effectively filters the signal at the modulation frequency with a narrow bandpass, and therefore eliminates excess noise in the system. This idea was furthered with the advent of frequency modulation (FM) spectroscopy, which is a rapid and sensitive technique for detecting both absorption and dispersion features of species.

In FM spectroscopy [8], a single-mode laser oscillating at optical frequency ω_c is sinusoidally modulated with frequency ω_m and amplitude Ω (cf. figure 2.2b). This modulation is either produced externally with a phase modulator to achieve large frequency shifts (MHz to GHz) or internally with a transducer (e.g. piezoelectric transducer for a solid-state laser, or input current modulation for a laser diode) for lower frequency shifts (kHz to MHz). This setup produces a pure (FM) optical output consisting of a strong carrier at ω_c, and two weak sidebands at $\omega_c \pm \omega_m$. The modulated light then passes through a sample cell. It can be shown [17] that for laser light with

frequency $\omega_L = \omega_c + \Omega \sin(\omega_m t)$, the Taylor expansion of the light intensity transmitted through a sample cell containing an absorber with absorption coefficient $\alpha(\omega)$, yields a lock-in signal of

$$S(\Omega) = -\Omega L \frac{d\alpha}{d\omega} \sin(\Omega t) \tag{2.4}$$

for lock-in detection at frequency Ω, where it was assumed that the single pass loss and modulation amplitude are both very small, i.e. $\alpha L << 1$ and $\Omega/\omega_c << 1$. Similar expressions can be obtained for higher derivatives of the absorption coefficient. In general, the transmitted intensity can be detected on a square law detector and demodulated using standard RF heterodyne techniques. Both the phase and the dispersion associated with the spectral feature can be measured by simultaneously monitoring the amplitude and the phase of the heterodyne signal as the laser frequency is swept through the absorption feature.

FM spectroscopy achieves sensitivity improvements through noise reduction in several ways. Heterodyne and lock-in detection filter the frequency response to a narrow interval around the modulation frequency which reduces the total signal noise. Any low frequency background noise, such as from cell window absorption, laser intensity fluctuations, or sample concentration variations, is also reduced. Increasing the modulation frequency can minimize technical noise in the signal, such as 1/f noise. Furthermore, choosing a modulation frequency that is large compared to laser linewidth reduces noise inherent to the laser light, and choosing the modulation frequency to be larger than the spectral feature of interest maintains the spectral resolution of the original laser source. Thus the total noise may be limited to the quantum-noise limit of the statistical fluctuations in the number of detected photons, i.e., the shot-noise limit.

Typical MDAL_{shot} values that can be detected using FM spectroscopy lie in the range from 10^{-6} to 10^{-7} cm^{-1}. FM spectroscopy has been performed with many types of lasers, including laser diodes [96, 74] and lead-salt diode lasers [16]. Combinations of multipass cells and frequency modulation spectroscopy can achieved MDAL_{shot} of 10^{-10} cm^{-1}; most of the effort is concentrated on the detection electronics.

Intracavity Laser Absorption Spectroscopy

As its name implies, intracavity laser absorption spectroscopy is performed by placing a narrow-line absorber into the cavity of a laser. If the laser is single-mode, the laser gain is narrow-band, and lasing action can be strongly affected by the sample absorption. Therefore, in order to obtain a reasonable sensitivity enhancement over a passive sample cell, the laser medium pump must be kept close to threshold with a constant pump power. Minor changes in intracavity losses may result in large changes in the laser output. It can be shown that the effective pathlength, l_{eff}, is given by [17]

$$l_{eff} = \frac{g_o}{\gamma(g_o - \gamma)} \tag{2.5}$$

where γ is the total passive intracavity loss per roundtrip, and g_o is the unsaturated laser gain. Tthis approach is limited by the increasing instability of laser output as threshold is approached, and by a spontaneous emission background from the laser above threshold.

By using the homogeneously broadened gain of a multimode laser that is much broader than the absorption features of interest, the laser gain will only be affected by broadband losses such as cavity mirror loss. Then, the gain will be determined by the smallest loss among oscillating modes. The absorption spectrum is obtained by switching on an intracavity output acousto-optic modulator to direct the laser emission onto a spectrograph (cf. figure 2.2c). The emission and hence absorption spectra are resolved on a detector array.

In this case, the sensitivity gain occurs because light inside the laser cavity travels through the absorber many times, so that the laser cavity functions as a very effective multipass cell. Pathlength enhancements from 0.5 to 30 km have thus been achieved [9, 107]. The ultimate sensitivity of the emission spectrum of a multimode laser to intracavity absorbers is limited by laser pulse duration, nonlinear mode coupling. The photon number distribution M_o produced during the cavity buildup process develops

in time as $M(t_g)$[39]. The sensitivity enhancement factor is given by

$$M(t_g) = M_o \frac{\sqrt{t_g}}{M_{norm}} exp\left[-\left(\frac{q-q_o}{Q}\right)^2 \gamma t_r\right] exp(-\alpha c t_g) \tag{2.6}$$

where M_{norm} is a normalizing factor, t_g is the emission spectrum generation time, the rate of stimulated emission into a mode q has half-width half-maximum Q, γ is the cavity broadband loss rate, and c is the speed of light. The effective pathlength is then given by [39]

$$l_{eff} = ct_g. \tag{2.7}$$

By optimizing the ICLAS system, quantum noise limited detection is achieved [41].

Many different multimode lasers have been applied to intracavity spectroscopy: dye lasers [97, 40], Ti:sapphire lasers [27, 39, 40], fiber lasers [9], color center lasers[7], and diode lasers [6]. $MDAL_{shot}$ values vary widely, from 10^{-6} cm^{-1} for diode lasers, to 10^{-11} cm^{-1} for dye and Ti:sapphire lasers [107, 39, 40]. The primary advantage of ICLAS is its "multiples factor", which allows about 15 cm^{-1} of spectrum (with 0.01 cm^{-1} resolution) to be obtained in a single measurement, a few seconds in duration. Recently, $3x10^{-9}$ cm^{-1} MDAL in 400 μs long single-shot measurements has been demonstrated [42]. ICLAS also allows the use of sample cells haveing "dirty" windows (up to several percent losses) to be placed inside the laser cavity without affecting the sensitivity. Because the laser beam in ICLAS is spatially confined inside the laser cavity, it is possible to perform spatially resolved spectroscopies of complex environments such as supersonic slit jets and flame fronts. Furthermore, ICLAS can yield absolute absorption coefficients [100, 39] with quantum noise limited detection, even for poor quality detectors, owing to its effective unity quantum efficiency.

However, ICLAS is not without its disadvantages. It requires specialized, often expensive equipment, in particular a broadband laser, and a spectrograph. Difficulties can arise in determining the baseline losses with good accuracy. ICLAS measurements also demonstrate a relatively low dynamic range, compared to multipass or cavity ring-down spectroscopies. Finally, the spectral range (i.e. 300 to 1600 nm) of ICLAS remains limited by the availability of good quality broadband laser gain

media. Perhaps this spectral range limitation has been the greatest drawback in the applicability of ICLAS to detect trace pollutants.

2.2.3 Photoacoustic Spectroscopy

Photoacoustic spectroscopy is best suited for the detection of minute concentrations of a specific species present in a high pressure mixture. When a laser beam modulated at frequencies below 20 kHz and tuned to a molecular transition of the species of interest is introduced into the sample cavity, molecules of the desired species will be excited. These excited molecules can then transfer their energy through collisions, heating up the total sample present in the test cell (cf. figure 2.2d). Because the chopped laser beam appears only periodically, it will elicit pressure variations that can be detected with a microphone. The sensitivity in this case depends on the geometry of the photoacoustic cell and on the characteristics of the microphone. Modern microphones can be made very sensitive, so that detection levels of 10^{-10} cm^{-1} have been achieved.

The sensitivity limit of photoacoustic spectroscopy is typically not limited by electronic noise, as is the case for most laser absorption techniques. Rather, any laser light reflected from the cell windows, or scattered by background gases (e.g. aerosols) in the cell can contribute to the temperature rise and subsequent pressure variations. Furthermore, the use of high power lasers can produce photochemical reactions of the sample if the excitation wavelength is not correctly chosen. Photoacoustic spectroscopy also requires an acoustically quiet background, and remains an indirect detection technique. Quantitative measurements necessitate calibration using samples with well-known concentrations. However, uncertainties in the absolute measurement remain on the order of several percent.

Chapter 3

Basics of CRDS

A firm grasp of cavity ring-down spectroscopy and of its fundamental limitations can only be achieved if the response of an optical resonator, i.e. the ring-down cavity, is well-understood. Because optical resonators have existed for almost a century, and have been employed and modeled both as interferometers and laser cavities, their behavior has been extensively investigated. Excellent, detailed treatment of resonator theory can be found in books by Siegman [94], Demtröder [17], and Yariv [115]. For introductory and nomenclature purposes, the partitioning of light into 'modes' inside optical cavities will be briefly reviewed, followed by a basic description of cavity ring-down spectroscopy theory. The reader is refered to the work of Hodges, Looney and van Zee [33], Lehmann and Romanini [48], and Zalicki and Zare [121], for a more rigorous treatment of cavity ring-down spectroscopy theory. The origins of CRDS in mirror reflectrometry, and an overview of practical CRDS experiments using pulsed and CW laser sources, are presented in subsequent sections.

3.1 Overview of Linear Resonator Theory

Consider (cf. figure 3.1a) an optical resonator formed by two mirrors, each having reflectivity $R^{(i)}$, radius of curvature $r_c^{(i)}$, physical radius $r_m^{(i)}$, and separation d. A light wave inside the resonator propagates back and forth between the two mirrors, and suffers losses during each roundtrip caused by the finite mirror reflectivity ($R < 1$) and

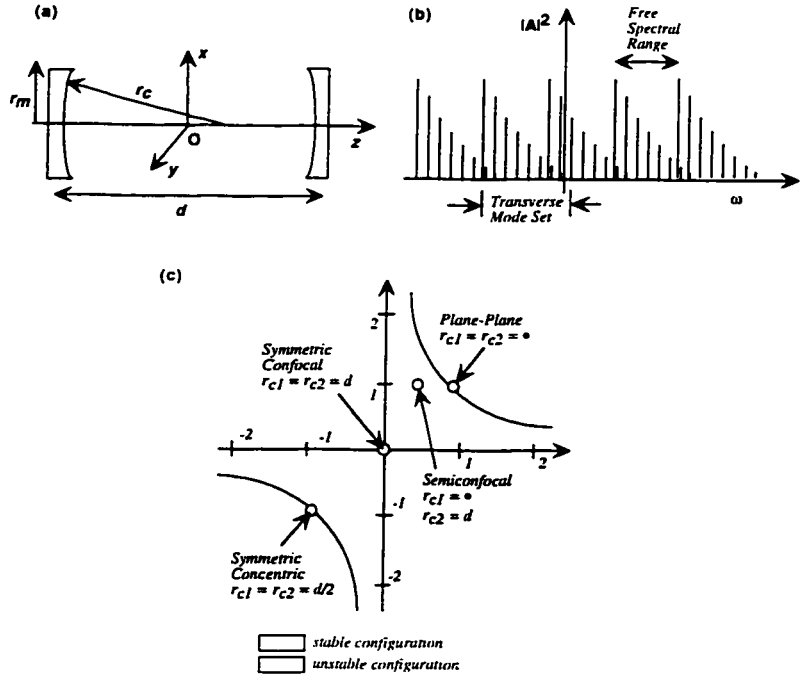

Figure 3.1: (a) Linear optical resonator formed by two identical circular mirrors, having spherical curvature. These mirrors are characterized by their radius r_m, radius of curvature, r_c, and separation d. (b) Mode structure of linear optical resonator. (c) Stability diagram for optical resonator.

the finite mirror area (diffraction). In other words, the resonator imposes boundary conditions on the electromagnetic radiation, both in and perpendicular to its direction of propagation. These boundary conditions force light existing the resonator to have particular characteristics, not unlike a particle in a box exhibiting quantized energy levels, or a finite length string vibrating only at certain acoustic frequencies.

3.1.1 Optical Resonator Stability and Modes

In out treatment of CRDS theory, a tacit assumption will be made about the optical resonator: it is a stable, spherically symmetric resonator. The resonator stability criteria must be defined to achieve an understanding of ring-down cavity design, since different research groups favor different cavity geometries. A full derivation of cavity stability can be found in most textbooks dealing with optics [94, 17, 115].

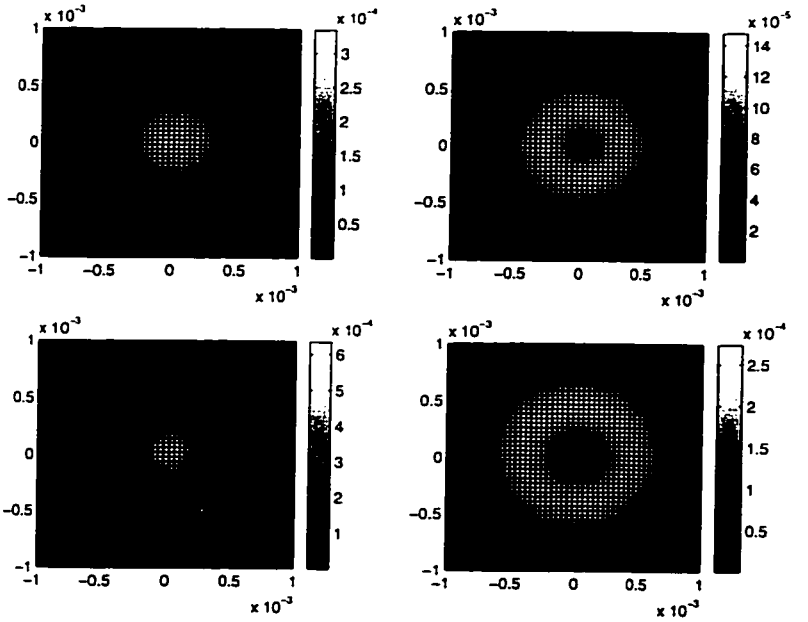

Figure 3.2: Laguerre-Gaussian modes for a spherical resonator.

In a stable resonator the field amplitude $E(x, y, z)$ reproduces itself after each round-trip up to a constant scaling factor that accounts for diffraction and/or reflection losses. For the cavity geometry presented in figure 3.1a, the stability criterion for the TEM_{00} mode is

$$0 < g_1 g_2 < 1 \quad \text{or} \quad g_1 = g_2 = 0 \tag{3.1}$$

where $g_i = 1 - d/r_c^{(i)}, (i = 1, 2)$ are the stability parameters. The stability diagram for linear optical resonators is shown in figure 3.1c, with specific resonator configurations indicated. Typically, stable, spherical resonators with identical mirrors ($r_c^{(1)} = r_c^{(2)} = r_c$, $r_m^{(1)} = r_m^{(2)} = r_m$, and $R^{(1)} = R^{(2)} = R$) have been used for CRDS, and will be assumed in all subsequent derivations. Symmetric confocal and plane-plane resonators are more sensitive to mechanical vibrations and acoustic noise, because they lie on the stability boundary. They are also much more difficult to align. Semiconfocal (hemispherical) resonators have a larger mode volume than spherical resonators for the same mirror separation, and have not been fully exploited. Ring resonators, consisting of more than two mirrors, have only recently been used [64], and can add

several degrees of freedom to ring-down cavity design, despite the additional losses incurred by the additional mirrors.

The specific forms of light that can exist unchanged (up to a scaling factor due to finite losses) within a resonator are called 'modes'. There are two types of modes corresponding to the two distinct types of boundary conditions: longitudinal modes are derived from the finite cavity length conditions; transverse modes are derived from the finite mirror area condition. Generally, any light existing within the optical resonator can be described as a superposition (i.e. weighted sum) of resonator transverse and longitudinal 'modes'.

3.1.2 Transverse Modes

The transverse (i.e. perpendicular to the direction of propagation) intensity distribution of light circulating inside an optical resonator with finite area mirrors will change after each roundtrip. Thus, a cavity transverse 'mode', or 'eigenfunction', can be defined as a specific transverse light intensity distribution, whose physical (or mathematical) form remains unchanged (up to a scaling factor) after each resonator roundtrip.

Transverse modes can be mathematically described by an orthonormal set of three-dimensional functions that are solutions of Maxwell's equations, and that satisfy the optical resonator boundary conditions. These mathematical 'modes' are usually only approximate solutions to the natural cavity 'modes' that physically exist within the resonator [94]. A rigorous derivation of actual cavity modes is found in reference [105]. A derivation of the commonly used approximate modes, namely Hermite-Gaussian and Laguerre-Gaussian modes, using Fresnel's integral, is found in references [94] and [11].

The simplest approach used in deriving optical resonator transverse modes is to assume that light in the resonator, $E(x,y,z,t) = \psi(x,y,z)e^{i(\omega t - kz)}$, satifies the paraxial wave equation, i.e. that the second partial derivative of $E(x,y,z,t)$ with

respect to z (the direction of propagation) can be neglected,

$$0 = \frac{\partial^2\psi}{\partial x^2} + \frac{\partial^2\psi}{\partial y^2} - 2ik\frac{\partial\psi}{\partial z}, \tag{3.2}$$

and to find a complete set of orthogonal solutions, given the boundary conditions of two mirrors separated by distance, d. It can be shown that for mirrors having cylindrical symmetry, the Laguerre-Gaussian (LG) functions constitute a complete set of orthogonal solutions. Using cylindrical space coordinates (r, θ, z), the general expression for LG functions is,

$$\psi_{p,l}(r,\theta,z) = \sqrt{\frac{2p!}{\pi(p+l+1)!}}\left(\frac{\sqrt{2}r}{w^2}\right)L_p^l\left(\frac{2r^2}{w^2}\right)e^{-\frac{r^2}{w^2}}e^{-i(\frac{kr^2}{2R}+l\theta-(2p+l+1)\tan^{-1}(\frac{z}{z_R}))} \tag{3.3}$$

where (p, l) are the 'mode numbers', $\lambda = 2\pi/k$ is the wavelength of the light, $w_0 = \frac{\lambda}{2\pi}\sqrt{d(2r_c - d)}$ is the beam waist, $z_R = \frac{\pi w_0^2}{\lambda}$ is the Raleigh range, $w = w_0\sqrt{1 + (\frac{z}{z_R})^2}$ is the actual beam spot size at distance z from the cavity center, $R = z + z_R^2/z$, and L_p^l is the (p, l)th LG polynomial. LG polynomials satisfy the recursion relation:

$$pL_p^l(x) = (-x + l + 2p - 1)L_{p-1}^l(x) - (l + p - 1)L_{p-2}^l(x) \tag{3.4}$$

where $L_0^l(x) = 1$, $L_1^l(x) = (l + 1) - x$, and $L_2^l(x) = \frac{1}{2}(l + 1)(l + 2) - (l + 2)x + \frac{1}{2}x^2$. LG polynomials can also be generated from

$$L_p^l(x) = \frac{e^x x^{-l}}{p!}\frac{\mathrm{d}^p}{\mathrm{d}x^p}\left(e^{-x}x^{l+p}\right) \tag{3.5}$$

Any given light input to the resonator, $E_i(x, y, z, t) = A(x, y, z)E_a(t)$, can be decomposed into LG resonator modes:

$$A(x,y,z) = \sum_{p,l} C_{pl}\psi_{p,l}(x,y,z) \tag{3.6}$$

where the complex coefficients C_{pl} are a measure of the spatial overlap between E_i and the (p, l)th mode (cf. figure 3.1). This decomposition is yet another illustration

of the superposition principle. As will be seen later, each resonator mode has its own characteristic ring-down parameters, so that each mode excited affects the ring-down measurement differently.

3.1.3 Longitudinal Modes

A light wave propagating back and forth inside the resonator along the direction of propagation will acrue both phase and attenuation. In mathematical terms, the longitudinal mode must be an eigenfunction of the operator that transforms the light field in the cavity, at position z and time t, to the light field at the same position, one roundtrip later. Thus, if the light field is to reproduce itself (up to the attenuation factor) indefinitely, then it must accrue a total phase shift of $2n\pi$ (n is an integer) over a round-trip

$$phase\left[\psi_{p,l}(x,y,-\frac{d}{2})e^{i(\omega t-k\frac{d}{2})}\right]-phase\left[\psi_{p,l}(x,y,\frac{d}{2})e^{i(\omega t+k\frac{d}{2})}\right]=2n\pi, n\in\mathbf{Z} \quad (3.7)$$

Equation 3.7 results in the phase condition that determines the longitudinal mode frequencies of the optical resonator for each transverse mode, i.e. for the (p,l)th transverse mode, the longitudinal modes can only occur at frequencies, $\nu_{p,l}^{(n)}$ that satisfy

$$\nu_{p,l}^{(n)}=\frac{c}{2\pi d}\left[\pi n+2(2p+l+1)\tan^{-1}(1-\frac{d}{r_c})\right], n\in\mathbf{Z} \quad (3.8)$$

where c is the speed of light and n is the index of the nth longitudinal mode.

Equation 3.8 demonstrates that there is an infinite number of longitudinal modes (index n) associated with each transverse mode (p,l), and that light can exist inside the resonator only if it posseses one of the modal frequencies. It is also clear from equation 3.8 that the frequency response of an optical resonator will resemble a comb in frequency space: the comb consists of a repeated series of transverse mode frequency patterns, where each subsequent pattern is separated from its predecessor by the longitudinal mode frequency spacing ($\frac{c}{2d}$), as seen in figure 3.1b.

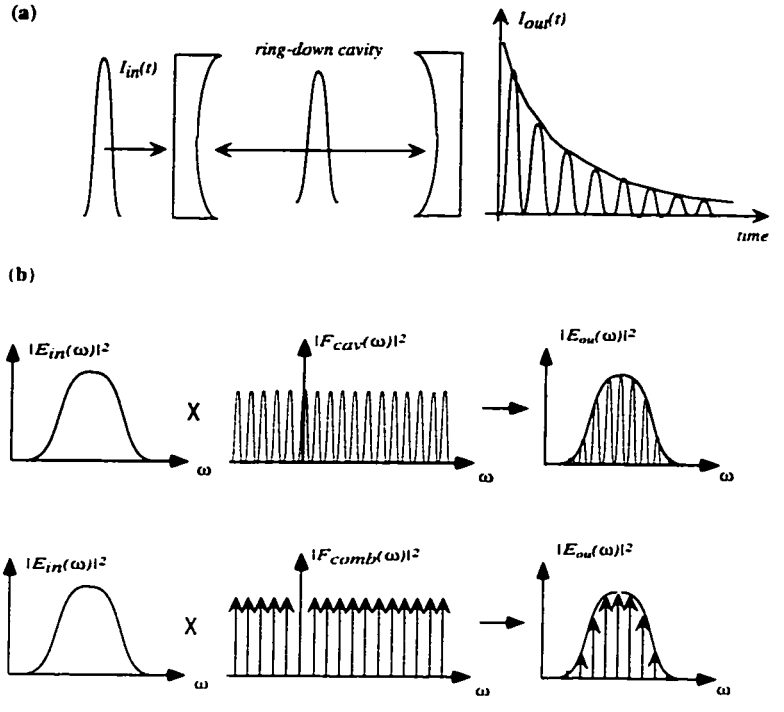

Figure 3.3: (a) Bullet model of pulsed CRDS. (b) Frequency domain model of pulsed CRDS for Dirac delta function comb and Airy function comb .

3.2 Introduction to CRDS Theory

The basic theory of pulsed CRDS will be presented in this chapter. The description of CRDS that follows does not pretend to be accurate or rigorous; its aim is to establish the general principles of CRDS so that the advantages and limitations of this technique can be discussed. The theory of CW-CRDS will be briefly reviewed in the experimental CW-CRDS section. For a more complete treatment of CRDS theory the reader is refered to references [33], [48], and [121].

3.2.1 A Simplistic View: The Bullet Model

Pulsed CRDS (P-CRDS) is based on the injection of a light pulse into an optical resonator, called the ring-down cavity (RDC) that is either empty or encloses the sample of interest (cf. figure 3.2a). From a 'bullet model' viewpoint, the envelope of the intensity of the pulses exiting the cavity decays exponentially in time at a rate

dependent on the total cavity losses. These losses comprise the finite reflectivity of the mirrors, diffraction, and any absorption within the cavity. If I_{out} is the intensity of light pulses monitored at the output of the cavity, I_{in} is the initial pulse intensity, $t_{rt} = (2L)/c$ is the round-trip time of the cavity, and the pulse duration is assumed to be much shorter than t_{rt}, then the output intensity after n round-trips is

$$I_{out}(nt_{rt}) = T^2(1-\alpha_{abs})^{2n+1}(1-\alpha_{cav})^{2n+1}I_{in} \tag{3.9}$$

where T is the mirror transmitivity, and total cavity losses are $\alpha = \alpha_{abs} + \alpha_{cav}$ in the presence of an absorber. If the losses are small ($\alpha \ll 1$), then the output pulse intensity can be rewritten such that it decays exponentially

$$I_{out}(nt_{rt}) = T^2 e^{-(2n+1)(\alpha_{abs}+\alpha_{cav})}I_{in} \tag{3.10}$$

and the envelope of this signal, as observed using a detector too slow to resolve individual pulses, is

$$I_{env}(t) \propto e^{-\frac{2(\alpha_{abs}+\alpha_{cav})}{t_{rt}}t}. \tag{3.11}$$

Thus, the decay rate of the cavity depends on empty cavity losses and on absorption losses of a sample present inside the resonator. This exponential decay due to absorption is exactly a restatement of Beer's law when $\alpha_{abs} = \epsilon C d$, where ϵ is the extinction coefficient and C is concentration. If ϵ is known for a specific wavelength and species, then the concentration of the species present can be determined by measuring the absorption losses.

3.2.2 A More Sophisticated View: RDC Transfer Functions

However straightforward and appealing the previous reasoning may seem, it is not really correct. Although it simply explains why an exponentially decaying envelope is usually observed in ring-down experiments, it fails to account for the amplitude and phase of the field within the optical resonator. It also fails to account for the fact that only light having frequencies near a cavity mode that can exist inside the resonator. If only a set of allowed frequencies can propagate inside and through the resonator, one

may wonder why pulses in the output pulse train appear to be identical in temporal shape to the input pulse. This fact, and a few others needed later to illustrate the utility of CW-CRDS, can be explained by considering the physics of CRDS in the frequency domain, and deriving the RDC transfer function. Details of the derivation followed here can be found in reference [48].

Assume for the moment that the input intensity pulse $I_{in}(t)$, with corresponding input field $E_{in}(x, y, -\frac{d}{2}, t)$ has a linear polarization, and excites only a single cavity transverse mode (the TEM_{00} mode),

$$E_{in}(x, y, -\frac{d}{2}, t) = C_{00}\psi_{00}(x, y, -\frac{d}{2})e^{i(\omega t - kz)}m(t)$$

where $m(t)$ is the field time dependence (e.g. gaussian pulse, square wave pulse, etc) and $C_{00} = (C_{00}^x C_{00}^y)$ is the coupling coefficient. Then the field at the output of the RDC can be written as [48]

$$E_{out}(t) = \sum_{n=0}^{\infty} Tr^{2n+1}e\left(t - (n + \frac{1}{2})t_{rt}\right) \tag{3.12}$$

where $e(t) = e^{i\omega t}m(t)$, r is the field reflectivity of the mirrors, and $t_{rt} = \frac{2d}{c}$ is the cavity round-trip time. The cavity transfer function states the mathematical relationship existing between the input and output field time components and is given by the Fourier-transform (FT) of the cavity response to a Dirac delta function time input (which is uniformly distributed over all frequencies in frequency space). Using the standard FT formulation:

$$\tilde{E}(\omega) = \frac{1}{\sqrt{2\pi}}\int_{-\infty}^{\infty} E_{out}(t)e^{-i\omega t}dt$$

yields the RDC transfer function:

$$\tilde{F}_{cav}(\omega) = \frac{Te^{-i\omega\frac{d}{c}}}{1 - Re^{-i\omega\frac{d}{c}}} \tag{3.13}$$

$R = r^2$ is the intensity reflection coefficient for the RDC mirrors, respectively. It

should be noted that this is the transfer function of the cavity for the input light *field*, and that this transfer function cannot be simply squared to obtain transfer function for light *intensity* if more than one mode is excited in the cavity. However if only a single mode is excited, the FT of the ring-down waveform can be directly obtained by squaring $\tilde{F}_{cav}$, and multiplying it by the FT of the input light intensity, and the detector intensity response.

From equation 3.13, it can be seen that for a single transverse mode, the RDC intensity transfer function is a series of identical, sharp resonance peaks (cf. figure 3.2b), each having an Airy lineshape, and relative separation of $\frac{2\pi c}{d}$, called the free spectral range (FSR) of the RDC. This transfer function is independent of the type of input signal applied to the RDC and relates the FT of the input signal to that of the output signal. It should be noted that this transfer function for the cavity is independent of phase noise in the input signal, of the duration of the input signal, of the carrier frequency of the input signal, or of the effective bandwidth of the input signal. Thus, the cavity properties remain the same, regardless of the coherence length of the input pulse. However, the coupling coefficient C_{00} may be drastically reduced if mode matching to the cavity spatial and longitudinal mode is poorly realized.

The halfwidth of the RDC transfer function resonances in frequency space, $\Delta\nu_{1/2}$, can be shown to be given by

$$\Delta\nu_{1/2} = \frac{c}{2d}\frac{1-R}{\pi\sqrt{R}},$$

and can also be expressed in terms of the RDC FSR by $\Delta\nu_{1/2} = \frac{FSR}{F^*}$, where F^* is the cavity finesse. As the reflectivity of the mirrors increases ($R \rightarrow 1$), the RDC halfwidth decreases, while the FSR remains unchanged, being dependent on RDC geometry. The RDC finesse increases with increasing mirror reflectivity. Thus, less of the total input light can enter, and consequently exit the cavity. This tradeoff between cavity throughput and finesse will be discussed further in the context of CW-CRDS. Presently, it will only be noted that increasing the finesse increases the RDC decay time, which increases CRDS sensitivity, while decreasing the throughput increases noise levels in the detected waveform (it is harder to detect less light), which

decreases CRDS sensitivity.

At this point, a brief explanation of why the output signal of a CRDS measurement often 'looks' like an exponentially decaying series of input pulses is at hand, and can be understood as a direct consequence of the relationship that exists between the FT and the Fourier series of a function having finite duration (i.e. a pulse). For simplicity, it has been assumed that only the TEM_{00} mode of the cavity has been excited. However, this argument can be extended to multi-mode excitation as shown by Hodges *et al.* [33]. Figure 3.2b illustrates two cases in frequency space for the same input pulse: the FT of the output for a RDC, which is a series of Airy functions separated by the FSR, $\tilde{F}_{cav}(\omega) = \sum_{n=-\infty}^{\infty} \tilde{L}(\omega - \omega_c - 2n\pi FSR)$, and the FT of the output for a comb of Dirac delta functions separated by the FSR, $\tilde{F}_{comb}(\omega) = \sum_{n=-\infty}^{\infty} \delta(\omega - 2n\pi FSR)$. For the delta function comb response, the output signal in FT space is equal, up to a multiplicative constant, to the Fourier series of the input pulse, which corresponds to a series of identical pulses occurring at a period equal to the inverse of the delta function frequency separation in the time domain.

For the RDC, the transfer function of the cavity is a comb of identical Airy functions, which can be expressed as the convolution of a single Airy function and a comb function: $\tilde{F}_{cav}(\omega) = \tilde{F}_{comb}(\omega) * \tilde{L}(\omega - \omega_c)$. Because the inverse FT of a convolution of two functions is the product of the inverse FT of each function, the time-domain response of the cavity to an input pulse is simply the product of the delta function comb response, a series of identical pulses, and the time-domain response of an Airy function, which can be approximated by an exponential decay. Therefore, the time-domain response of the RDC for *any* input pulse is simply a series of pulses identical in temporal shape to the input pulse, but having (approximately) an exponentially decaying envelope.

3.2.3 Some Notes on Mode-Matching

If multiple-modes are excited inside the RDC, the output field of the RDC will consist of the weighted sum of exponentially decaying fields, each having a different time constant. If the frequency difference between two such modes is comparable to the

rate of decay, and the output light of the cavity is not completely collected, then sinusoidal beating will be observed [55], and may preclude the accurate determination of the ring-down rate. Note that the excitation of multiple longitudinal modes will result in a similar mode beating, but because the beating frequency equals the cavity FSR (typically > 100 MHz), this effect will occur too quickly to be observed with most detectors, although it may still appear as excess noise on the decay waveform.

To calculate the total field for multi-mode excitation, the response of the cavity for each mode must be first computed, and the field responses summed, before taking the square of the magnitude. The cross-terms in this squared sum will produce mode-beating effects if all the light is not collected. Such calculations can rapidly become complex. Once again, if all the light is collected at the detector (which is rarely the case in actual experiments), mode interference is completely eliminated and each mode can effectively be treated independently. Nonetheless, the superposition of many exponential decays, each having a slightly different decay constant, is difficult to analyze and fit. For accurate ring-down rate measurements, multiple transverse mode excitation is clearly undesirable. Thus, the quality of P-CRDS experimental results usually depends on the effort made to mode-match the laser source to a single transverse mode of the cavity.

3.2.4 CRDS Experiments and Advantages

In actual CRDS experiments (cf. figure 3.2a), a pulsed laser source is injected into a cavity having high reflectivity mirrors ($\alpha_{cav} < 10^{-3}$ cm^{-1}), and the exponentially decaying output pulse train is measured on a photodetector. Signal processing is then performed on the electrical decay waveform to extract its rate of decay. This can either be done by digitizing the waveform on an oscilloscope and then fitting the set of data points numerically or by integrating the two portions of the waveform and taking their ratio, as is done with a boxcar integrator. The rate of decay is obtained at different wavelengths for both an empty cavity and a cavity containing the desired sample. By subtracting the empty cavity rate (i.e. the baseline) from that of the sample-containing cavity (i.e. the spectrum), a quantitative spectrum of the sample

is obtained, which can be directly converted into an absolute concentration.

There are several advantages to this approach:

- The measurement of an absorption spectrum depends only on the *rate* of decay of light inside the cavity, rather than the intensity of the transmitted light, so that it is independent of laser pulse to pulse intensity fluctuations.
- CRDS uses a low-loss optical resonator to enhance its pathlength up to several tens of kilometers (at a loss to good coupling efficiency).
- The baseline losses of the cavity can be measured by simply evacuating it and taking a spectral scan. When these losses are subtracted from a spectral scan involving a sample, absolute absorbance values for the sample are directly and simply obtained.
- Pulsed CRDS is a very simple technique to implement experimentally.

In contrast to direct absorption measurements, CRDS is insensitive to intensity fluctuations of the laser source. In contrast to multipass cells, CRDS optical resonators are stable, and may be less sensitive to length changes or temperature fluctuations. For any given absorptive transition, CRDS can be used to quantitate either extinction coefficients when concentration is known, or vice versa. Unlike FM spectroscopy or intracavity laser absorption spectroscopy, CRDS is a self-calibrated, absolute measurement technique. For simple setups involving a laser source, some mode-matching optics, a detector, and signal processing equipment, nominal sensitivities of 10^{-7} to 10^{-8} cm^{-1} can easily be achieved. For these detection levels, the setup will be relatively insensitive to mechanical, acoustic, or thermal noise, unlike photoacoustic spectroscopy. For more complex ring-down setups that attempt to achieve sensitivities of 10^{-12} cm^{-1}, the latter noise sources may become much more important.

3.2.5 CRDS Sensitivity

We need a common way of expressing the sensitivity that can be achieved in absorption spectroscopy. For this purpose, we introduce the following definitions. We

call the absorption signal S. We denote by $\langle ... \rangle_{av}$ the average over the duration of an absorption measurement, which we call a shot, and denote this duration by Δt_{shot}. Thus, the mean absorption signal $\overline{S}$ is $\langle S \rangle_{av}$, and the standard deviation of the signal is found from $\sigma_S^2 = \langle (S - \overline{S})^2 \rangle_{av}$. The minimum detectable fractional signal per shot is $MDFS_{shot} = \sigma_S / \overline{S}$. It follows that the minimum detectable absorption loss per shot is $MDAL_{shot} = MDFS_{shot}/l_{eff}$, where the physical sample length l_{sample} is less than or equal to l_{eff}, which is the total distance the radiation traverses in the sample. $MDAL_{shot}$ has units of cm^{-1}. By repeated absorption measurements at a specific wavelength the minimum detectable absorption loss decreases as the square root of the number of measurements, assuming that the measurement error is only statistical. If N replicate measurements (shots) are acquired, then the minimum detectable absorption loss becomes

$$MDAL(N) = \frac{MDAL_{shot}}{\sqrt{N}}. \tag{3.14}$$

For a measurement repetition rate of f shots per second, which may differ from but not exceed $1/\Delta t_{shot}$, the sensitivity is defined as

$$S_y = MDAL(f), \tag{3.15}$$

which has units of $cm^{-1}\ s^{-1/2}$.

CRDS sensitivity can be defined as:

$$S_y = \sqrt{2}\frac{MDAL_{shot}}{\sqrt{N_{phot}}} \tag{3.16}$$

where the signal for $MDAL_{shot}$ is the ring-down time, $\tau(t)$, and N_{phot} is the number of photons impinging on the photodetector. The sensitivity can be improved by decreasing $MDAL_{shot}$, and by increasing the cavity throughput. It is clear that under ideal conditions, with no noise introduced by detection electronics, shot-noise-limited experiments only restricted by cavity throughput could be performed. Presently, the state-of-the-art electronics, especially the detectors and digitizers used to render decay waveforms for mathematical fitting on a personal computer, introduce noise that exceeds the shot noise of the light. Cavity throughput will always remain a

limitation of P-CRDS, but can be minimized by the use of narrowband, externally modulated continuous-wave (CW) laser sources. The best pulsed source $MDAL_{shot}$ is about 0.2% [34], whereas the best CW source is $MDAL_{shot}$ 0.05%[99]. The best CRDS sensitivity achieved to date is on the order of 10^{-10} cm^{-1} [77], but is expected to decrease as detection systems improve. In fact, by using slightly more complex detection schemes such as heterodyning the ring-down signal with a local oscillator, shot-noise-limited measurements have now been enabled[99].

3.3 Precursors of CRDS: Mirror Reflectometers

The evolution of optical science took a giant leap in the second half of the 20th centure with the advent of the laser, the silicon-based semiconductor transistor and integrated circuit, the compound semiconductor optoelectronic photodiode and diode laser, the optical fiber, and a new generation of thin film optical coatings. Without these technolgical advances, cavity ring-down spectroscopy would not be possible today. Ironically, the advances in optical coating technology, and a lack of suitable measurement techniques for highly reflecting mirrors, brought about the birth of cavity ring-down spectroscopy.

As high reflectivity mirrors became more important for many applications and optical instruments (such as high power lasers, gyroscopes, optical frequency standards), considerable efforts were made by the commercial manufacturers. Over the last decade, significant progress was achieved in the development of superpolished, high purity substrates (surface roughness less than $\lambda/10{,}000$), as well as in the growth of extremely low-loss thin-film dielectric coatings. Mirros with losses on the order of parts per million (ppm) are readily available in the visible and near-infrared. Mirrors with several tens of ppm are available in the mid-infrared, and are expected to become available in the near future for the ultraviolet. Record reflectivities for these "supermirrors" are 0.999994, corresponding to losses of $6x10^{-6}$, or 6.0 ppm [18].

Although the transmission, T, through these high reflectors could be measured by very precise and expensive power meters having a large dynamic range, little information could be obtained about the mirror reflectivity, R, and mirror scattering

and absorption losses, S (where $T + R + S = 1$). Two competing techniques were developed to measure reflectivity based on the decay constant of a linear cavity Fabry-Perot resonator formed by two plano-concave mirrors: measurement of light intensity decay constant when the excitation source is abruptly terminated [5, 73], and measurement of the phase shift accrued by amplitude modulated light as it traverses the resonator [30, 29, 20].

In 1980, Herbelin *et al.* [30] were the first to propose measuring the photon lifetime in an optical resonator to determine mirror reflectivity. In 1985, Elleaume *et al.* used the phase-shift method to measure the reflectivity of mirrors used in a free-electron laser and to determine the mechanisms of UV-induced degradation on the dielectric stacks. In both approaches, a CW laser beam was amplitude modulated with an external electro-optic modulator (frequency f), which produced a linearly polarized, sinusoidally varying photon beam. Once this modulated beam passed through the linear optical resonator of interest, it became shifted in phase by angle α, which is directly related to the cavity intensity decay time τ by [29] $\tan(\alpha) = 4\pi f\tau$. Phase shift α was determined by standard lock-in detection, as shown in figure 3.3a: the phase of the light was measured before and after the resonator, and these two phases were subtracted to yield α; or, $\tan(\alpha)$ was directly measured using two lock-in amplifiers with a relative phase shift of 90°. Herbelin also remarked that "Many other applications are envisioned, including very sensitive gas-phase absorption studies and the study of optically transparent materials under high electric or magnetic fields or both" [30]. Meijer *et al.* [24] realized this prediction sixteen years later.

In 1985, Anderson *et al.* [5] were the first to use cavity decay time measurements to measure mirror reflectivity. The output of CW He-Ne laser was directed to the input of a linear optical resonator through Pockels cell and mode-matching lenses. When sufficient light was built up inside and transmitted by the optical resonator onto a photodetector, the laser light was terminated by the Pockels cell. The decay of light inside the resonator was then monitored using the photodetector, and decay time, τ, was measured using a counting circuit. Frequency overlap between the cavity and laser were incidental. The mirror reflectivity R, was then computed from the decay lifetime τ: $R \approx t_{rt}/\tau$, where t_{rt} is the cavity round-trip time.

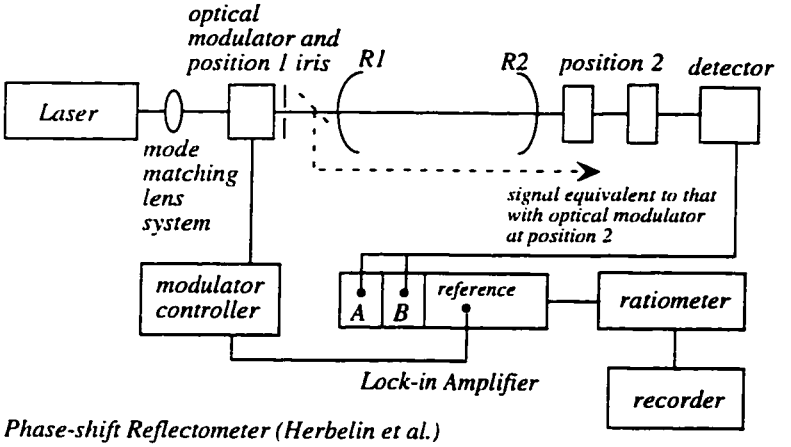

Phase-shift Reflectometer (Herbelin et al.)

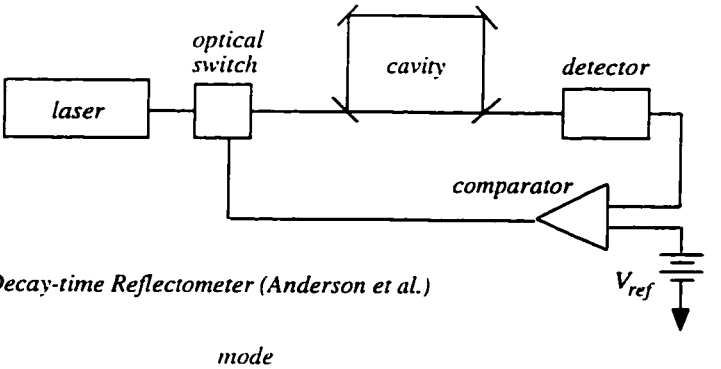

Decay-time Reflectometer (Anderson et al.)

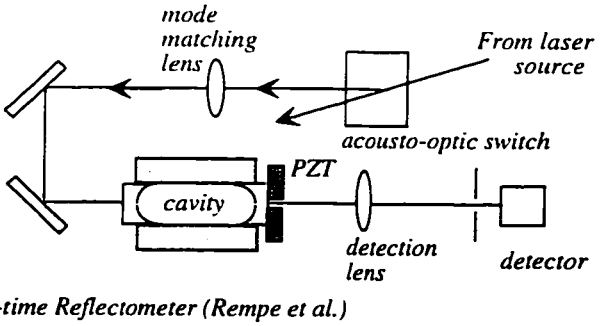

Decay-time Reflectometer (Rempe et al.)

Figure 3.4: Reflectrometry setups by (a) Herbelin *et al.* [29] for phase shift detection, (b) Anderson *et al.* [5] for decay-time detection, and (c) Rempe *et al.* [73] for decay-time detection.

Rempe *et al.* [73] used a similar approach in 1992 to measure the reflectivity of 1.6 ppm loss supermirrors. In contrast to Anderson, Rempe mounted one of the cavity supermirrors onto a piezoelectric actuator, so that the cavity length could be scanned across the test laser linewidth to build up light inside the resonator. When a sufficient light level was obtained, the CW laser light was deflected from the cavity with an acousto-optic modulator. The light intensity decay waveform was digitized and then numerically fit. This approach was adopted four years later by Romanini *et al.* [78, 77] to perform the first CW laser cavity ring-down spectroscopy experiments.

Anderson's time domain approach, rather than the phase shift technique, was later adopted by most supermirror manufacturers [73], and was even commercialized. It is interesting to note a remark by Anderson [5]: "The cavity optical path was evacuated: we have made tests in open air cavities, but found our results depended on the ambient Pasadena air quality." Anderson *et al.* had measured molecular absorption losses, but they did not pursue the spectroscopic avenue. Three years passed before the first pulsed laser cavity ring-down spectroscopic application was fully documented by Deacon and O'Keefe [62].

3.4 Pulsed Cavity Ring-Down Spectroscopy (PCRDS)

The first incarnation of PCRDS appeared in the literature in 1988 in a paper by O'Keefe and Deacon [62], where a nitrogen laser-pumped pulsed (15 ns) dye laser, emitting at 690 nm and mode-matched to the TEM_{00} mode of the RDC, was used to investigate the $b\Sigma_g \rightarrow X^3\Sigma_g$ overtone transitions of molecular oxygen. Ring-down waveforms were digitized using an oscilloscope and the decay constant was extracted from a linear fit of the logarithm of the waveform (after baseline subtraction). For mirrors having R > 99.99%, and a cavity length of 25 cm, the first sensitivities reported were 2×10^{-8} cm^{-1}. Subsequently to this seminal paper in PCRDS [62], O'Keefe began a collaboration with the Saykally group at the University of California at Berkeley, which has endured to this day.

The first application of CRDS appeared in 1990 [63]: the UC Berkeley group used PCRDS with a nitrogen laser-pumped dye laser (450 nm, 15 ns, 10-100 Hz

repetition rate) to investigate the spectroscopic constants of jet-cooled metal clusters in a molecular beam. They used a 55 cm long linear cavity with R $\propto$ 99.99% reflectors and obtained a spectral resolution of about 1 cm^{-1}. This approach proved very fruitful and a great deal of work was performed on metal clusters over the next six years [87]. Extensive spectroscopic investigations of silver silicides [85], aluminum silicides [88], and copper silicides [86] have been published. These later PCRDS experiments applied an excimer-pumped dye laser emitting in the ultraviolet (365 nm for silver, 405-413 nm for aluminum, and 400 nm for copper), with 0.3 to 0.04 cm^{-1} spectral resolution. The RDCs used were about 25 cm in length (primarily limited by the size of the molecular beam reactor), and had 99.99% reflectivity mirrors. Waveforms detected using a photomultipler (PMT) were acquired by a 12-bit, 20 MHz digitizer. A linear fit of the waveform logarithm (after baseline subtraction) was the preferred means for extracting the decay constant. MDAL on the order of 10^{-8} cm^{-1} were achieved, and allowed extensive vibrational analysis both of vibronic isotope shifts and rotational bands of the cluster spectra. Recently, PCRDS has been extended into the mid-infrared (using a Raman shifter cell) to study spectra of stable organic molecules and water clusters [67].

From 1993 to 1996, applications of CRDS were extended to detailed spectroscopic studies of line intensities, transition wavelengths, and coupling effects in vibrational and rotational spectra of gas phase species by Lehmann and Romanini at Princeton University [80]. When spectroscopic information from rotational structure of HCN and its isotopomers, $H^{13}CN$, and $H^{15}CN$ [83], was compared to *ab initio* calculations, Coriolis coupling in one band, and the Herman-Wallis effect (R and P branch asymmetry) in several bands were observed [83]. Furthermore, the standard computational techniques used to model vibrational overtone transitions for HCN were shown to produce inaccurate results when compared to experimental measurements, and CRDS enabled Lehmann and Romanini to improve on existing models [82, 81]. In the CRDS experiments, a Xe-Cl excimer-pumped dye laser (30 Hz repetition rate) operating between 480 and 580 nm with 0.04 to 0.08 cm^{-1} resolution was employed. Mode-matching optics were not fully deployed, resulting in intensity fluctuations of the output decay waveforms up to 50% [80, 82, 81, 83]. However, owing to the good

quality reflectors used (R > 99.99%), the 1.3 m cavity length, and detection using a PMT providing almost shot-noise-limited ring-down measurements, MDAL as low as $7 \times 10^{-10}\text{cm}^{-1}\text{s}^{-1/2}$ were achieved. It is interesting to note, that Romanini and Lehmann [80] did not digitize the ring-down waveforms, but used a two-channel box-car integrator to directly yield the sample absorbance, α, from the channel signals (A, B) and interchannel delay, Δt [80]:

$$\log(A/B) = \frac{\Delta t}{\tau} - \alpha c \Delta t \tag{3.17}$$

In fact, it was shown [80] that this detection scheme is inherently as accurate as waveform digitization followed by a linear fit (for $\Delta t_{opt} = 2\tau$) and reduced shot to shot fluctuations to the order of 0.5%. Lehmann and Romanini have also been instrumental in the development of CW-CRDS as will be recounted in the next section.

The Meijer group at the University of Nijmegen has been another source of innovations in PCRDS. In 1994, Meijer *et al.* [57] used short cavities having a dense transverse mode structure (and collecting all the modes to avoid mode-beating) to improve the potential resolution of PCRDS. By using a 10 cm, off-confocal RDC, they were able to obtain a 10 MHz transverse mode spacing, and hence perform spectroscopy on the OH radical in a flame at 298 nm (doubled Nd:YAG pumped dye laser). In all their PCRDS studies, the Nijmegen group digitize the ring-down waveform on an oscilloscope and use a linear fit to obtain the ring-down constant, in the spirit of the original O'Keefe paper. In addition to performing detailed spectroscopic studies of oxygen [35, 98] for comparison with detailed theoretical *ab initio* calculations, and applying PCRDS to the study of laser desorbed, jet-cooled organics (diphenylamine) [10], the Nijmegen group was the first to demonstrate the utility of PCRDS in the UV for trace gas detection. Using a pulsed Nd:YAG pumped dye laser followed by a KDP and/or BBO doubler to obtain radiation at 300 nm, the Nijmegen group showed PCRDS sensitivities of 10 parts per billion to ammonia, and 1 part per trillion to elemental mercury in air [38]. The Nijmegen group was also the first to point out laser bandwidths effects in PCRDS, which result in multi-exponential decays if the laser line is broader than the absorption feature. The Nijmegen group

was also the first to demonstrate PCRDS in the far-infrared using a free-electron laser tuned between 10 and 11 μm to measure vibrational transitions of ethylene [25]. In the past two years, three other important PCRDS innovations have appeared thanks to the Nijmegen group: phase-shift CW-CRDS discussed in the following section [24], Fourier-transform PCRDS [23], and polarization-dependent PCRDS [22]. Briefly, Fourier-transform PCRDS combines the multiplex and resolution advantage of a Fourier-transform spectrometer with the sensitivity of PCRDS: time-resolved FT scans are taken at the output of the RDC excited with a broadband source, so that the inversion of the interferogram yields the time-dependent ring-down waveform at all excitation frequencies, i.e. yields the entire decay constant spectrum. In polarization-dependent PCRDS, the sample is exposed to the presence of a magnetic field, the polarization of the excitation source is set to be a mixture of orthogonally polarized light components, and the spectral splittings are observed by simultaneously collecting and then subtracting ring-down spectra at the two orthogonal polarizations.

From 1995 to the present, Zare and co-workers [119, 118, 109, 108] at Stanford University have been applying PCRDS in the ultraviolet (216 nm) for the detection of methyl radicals in a hot-filament reactor used for chemical vapor deposition of diamond films. PCRDS was demonstrated to be a much more sensitive absorption detection technique than multipass direct absorption spectroscopy [118], and to have sufficient spatial resolution (along the axis perpendicular to the RDC) to facilitate spatially resolved concentration profile measurements in the reactor [119, 109]. Thus the methyl radical concentration could be measured as a function of distance from the hot filament, and the implications of this concentration profile on the chemistry of diamond film growth rates deduced [109, 108]. There has been much confusion in the literature as to what conditions are necessary for the ring-down waveform to exhibit exponential decay in PCRDS. The Stanford group was the first to show, using an Nd:YAG-pumped, Fourier-transform-limited optical parametric oscillator (OPO) laser source, that multimode cavity excitation results in mode effects that can severaly distort the ring-down waveform. Thus, they were able to eliminate mode beating in further experiments involving this laser source [55]. The Stanford group [114] also recently applied CRDS in the visible to obtain spectra of ground state

species in hostile environments. The spectra of overtone rovibrational transitions of water vapor generated by combustion in an atmospheric pressure, methane-air flat-flame were obtained as a function of distance from the burner surface. From these spectra, the temperature and concentration profiles of water vapor were computed. Baseline degradation caused by non-uniform optical densities and emission from the flame medium were shown to be acceptable. MDAL values on the order of 2×10^{-8} cm^{-1} were obtained for these hostile environments.

In 1996, Hodges, Looney and van Zee at the National Institute of Standards were the first group to dedicate experiments to the actual physics PCRDS. Their efforts have resulted in two very detailed studies of laser source effects on the noise and sensitivity of PCRDS. In particular, the NIST group [34] was able to demonstrate the limitations of using laser sources that are broadband when compared to the absorption features of interest, and showed that it is possible to overcome these limitations by using cavities where only a single mode is excited (so that the RDC determines PCRDS resolution, rather than the laser linewidth). Furthermore, the NIST group [33] performed very careful PCRDS experiments to determine the effects of mode beating and multi-mode excitation on noise in the ring-down waveforms, and the consequent reduction in detection sensitivity. By eliminating these effects, they have recently obtained shot to shot noise statistics on the order of 0.2%, a significant improvement over most PCRDS systems.

Scherer and Rakestraw at Sandia National Laboratories furthered PCRDS into the mid-infrared [91] in 1996: an OPO was used to obtain the first PCRDS spectra of acetylene at 1.6 μm, and of methane at 3.3 μm. In this case, the OPO output consisted of almost-Fourier-transform-limited pulses (2-4 ns) providing a resolution of 0.0025 cm^{-1}. MDAL on the order of 10^{-7} cm^{-1} were obtained in the mid-infrared. The Sandia group has also recently demonstrated the effectiveness of PCRDS for spectroscopy in harsh environments [90, 36]: the rovibrational spectra of methyl radicals were measured in a low-pressure laminar-flow methane/air flame around 3 μm, and data were compared to flame chemistry simulations under various flame stoichiometric conditions. Similarly, Scherer employed PCRDS for the detection of formyl

radicals in low pressure $CH_4N_2O_2$ flame [89] using ultraviolet radiation, demonstrating sensitivities comparable to intracavity laser absorption spectroscopy.

Over the last two years, PCRDS has become more and more popular among spectroscopists as its utility to chemists seems to increase day by day. Recent applications of PCRDS to hostile environments include detection of C_6H radicals in a hollow cathode discharge by Maier *et al.* [44] and spectroscopy of NaH in flames by Hering *et al.* [49]. Application of PCRDS to predissociation dynamics include studies of the ^1A state of HNO [68] and the $A^2\Sigma^+(\nu = 1)$ state of the SH radical [112] by Ashfold *et al.* in the visible and ultraviolet, respectively, and studies by Ding and Zdu of photolysis products of ethyl nitrate [123] and glyoxal [122] in the ultraviolet. Other spectroscopic applications of PCRDS include studies of acetylene spectra at 1064 nm using ultrahigh finesse cavities by Nakagawa *et al.* [60], measurements of the radiative lifetime of the $A^1\Delta_g$ state of molecular oxygen by Miller *et al.* [58], detection of ultra-slow mirror velocities by Feld *et al.* [4], and evanescent-wave cavity ring-down spectroscopy for liquids based on total internal reflections by Pipino *et al.* [71]. It can be stated without a doubt that over the next decade PCRDS will gain acceptance as a standard spectroscopic tool, with applications ranging from reaction dynamics to detailed spectroscopic studies of complex molecules, and using sources from the deep ultraviolet to the far-infrared.

3.5 Continuous-Wave Cavity Ring-down Spectroscopy (CW-CRDS)

The use of pulsed lasers imposes several limitations on PCRDS. Unless care is specifically taken to mode-match the laser to only a single mode of the RDC [33], and allow the cavity to synchronously follow the laser, PCRDS often suffers from excess noise caused by multi-mode excitation, and can be limited in resolution (for dense mode RDCs) by the laser linewidth. Analysis of the behavior for multi-mode systems can prove to be tedious [34, 48]. For pulsed lasers, even when Fourier-transform-limited,

the laser linewidth typically exceeds several hundred MHz ($\propto 0.002$ cm^{-1}). Data acquisition rates have been limited in the past by slow repetition rates of pulsed lasers, although OPOs having kHz repetition rates are presently becoming available. Most importantly, the intensity of the light coupled into and out of the cavity is small in PCRDS ($T^2 I_{in}$ comes out), as a consequence of the high cavity mirror reflectivity. To overcome these problems, Lehmann [47] proposed the use of continuous wave (CW) laser sources. Single-mode, CW lasers modulated externally not only have higher duty cycles allowing kHz repetition rates (limited only by the buildup time of light inside the RDC), but also have narrower linewidths (typically < 100 MHz). The resulting increased overlap between the laser and RDC linewidth results in actual energy buildup inside the RDC [94]. Higher light levels at the cavity output imply improved signal-to-noise ratios on the decay waveforms, improved waveform fitting accuracy, and better detection sensitivity. Furthermore, the ability to use CW laser sources enables the exploitation of relatively inexpensive laser sources: laser diodes.

In a similar approach as that first presented by Herbelin *et al.* [29], the Nijmegen group [24] was the first to measure phase-shifts accrued by a sinusoidally modulated CW laser beam after it passes through a cavity, and to deduce from this phase shift the losses accumulated from the RDC and from an absorber. Spectra of O_2 transitions were obtained around 635 nm using a single-mode, Argon ion pumped dye laser. The Nijmegen group demonstrated that acquisition rates of kHz were compatible with high-resolution CRDS, and that narrowband laser throughput could be made possible (though by no means optimized) by using resonators having a dense transverse mode structure. However, multi-mode excitation within the RDC produced excess noise in the decay constant measured, leading to reduced sensitivities on the order of 10^{-6} cm^{-1}.

Initially, efforts to use LDs in CRDS were directed at optically locking a LD to a high-finesse cavity [75]. This approach was precluded, however, by a lack of long-term stability (i.e., thermal drift) in locking the laser to the same cavity mode. Romanini *et al.* at the Centre National de Recherche Scientifique and Université Joseph Fourier (the CNRS-UJF group) [78, 77] avoided this optical locking problem altogether by sweeping one resonant mode of their ring-down cavity through the CW

laser linewidth. When sufficient buildup of light within the cavity was detected, the input laser beam was deflected with an acousto-optic modulator (AOM), and the cavity ring-down decay was recorded. Extensive mode-matching was carried out to guarantee that only TEM_{00} modes would be excited in the cavity, although excess baseline noise was reported when actual spectral scans were performed, with shot to shot variation in the decay time of several percent. Using this technique and a single-mode dye laser, the CNRS-UJF group achieved acquisition rates of several hundred Hz, greatly reduced baseline noise, and extreme sensitivities on the order of 10^{-10} cm^{-1}. The stability of this CW-CRDS system provided the reproducibility necessary to even obtain absolute measurements of continua [79].

Most of the laser sources previously described in CRDS experiments are not only large, and relatively complicated to operate, but are expensive. Although solid state lasers (e.g. OPOs, Ti:Sapphire lasers) are slowly replacing more traditional dye lasers with their increased reliability, ease of operation, mode quality, and tuning range, they are no less expensive. Laser diodes (LDs), on the other hand, have been decreasing in cost thanks to the continuous growth of the telecommunications and data storage industries. Today, laser diodes have sufficient power (> mW), wavelength coverage (UV to mid-infrared) and reliability to be used as experimental light sources. Owing to their compactness, high wallplug efficiency, and low cost, LDs seem to be an ideal source for implementing practical CW-CRDS systems.

The CNRS-UJF group was the first to employ external cavity diode lasers (ECDLs) in CW-CRDS [77] to measure high quality NO_2 spectra in a supersonic slit jet, with a residual Doppler width of about 250 MHz. Efforts are also underway by Lehmann to implement the swept cavity scheme using simpler distributed feedback (DFB) LDs for trace water vapor detection. The use of edge-emitting LDs (no stabilization grating as in DFBs) with linear cavities was first demonstrated by the Stanford group [66]. The problem of 'external cavity' formation between the LD back facet and externally placed optics (the output facet has a low reflectivity to maximize output power), affects both the phase and gain relations of LD and makes the LD output highly dependent on the uncontrollable external cavity length. This problem was eliminated by placing an acousto-optic modulator (AOM) inside the 'external cavity' formed by

the LD and the RDC input mirror. In this approach, only low optical isolation is required for the LD to achieve stable behavior and reproducible coupling into the RDC. A dense cavity transverse mode structure was used, that limited sensitivity (by multi-mode excitation) to 10^{-8} cm^{-1}.

In order to minimize multi-mode coupling into the cavity, and improve sensitivity, the Stanford group demonstrated that it is possible to frequency lock the RDC to the laser source [64]. A ring resonator consisting of two flat mirrors and a plano-concave mirror was exploited for its nondegeneracy between p- and s-polarizations. Thus, the RDC is effectively two resonators: a lower finesse RDC for p-polarized light, and a high finesse RDC for s-polarized. The laser beam was split into two arms: the p-polarized arm was used to lock the cavity to the laser, while the s-polarized light was used for CRDS. Thus, the locking arm could remain uninterrupted during the spectral scan, ensuring a continuous overlap between the laser line and TEM_{00} mode. It is noted that the s- and p-polarized TEM_{00} modes are shifted in frequency relative to one another. By using the Pound-Drever-Hall electronic locking technique, not only were intensity fluctuations between ring-down decays reduced to several percent, but the shot to shot fluctuations were reduced to 0.5%, comparable to P-CRDS. This cavity-locked approach ensured that only a single transverse mode was excited, and eliminated spurious oscillations in the spectral background. However, owing to the substantial linewidth of the ECDL (several MHz), throughput for the high-finesse cavity remained small, so that detector noise and poor quality mirrors (R=99.93%) limited the sensitivity to the order of 5×10^{-9} cm^{-1}.

The two-arm locking scheme with large p-arm cavity throughput, and limited s-arm throughput where the two beams are frequency-shifted relative to one another, has enabled heterodyne detection to be performed at the cavity output. This detection scheme, developed by Levenson *et al.* [52], improved the signal-to-noise ratio in the ECDL system by 31 dB, leading to digitization-limited shot-to-shot noise of 0.2%. Efforts are presently underway by the Stanford group to perform shot-noise limited CW-CRDS measurements using the locked cavity system with narrowband laser sources (nonplanar ring oscillator Nd:YAG) and low-noise detectors.

Shot-noise-limited detection of decay waveforms from supercavities (R > 99.995%)

is expected to improve single-shot CRDs sensitivity to $10^{-13}cm^{-1}s^{-1/2}$, assuming that about 50 mW of laser light exits the cavity, and heterodyne detection is performed with averaging of 100 waveforms at 100 Hz. This level of sensitivity would allow detection of about 100 molecules in the volume of the probe beam inside the optical cavity for strong infrared transitions and about 10 molecules for strong visible transitions. The results of this calculation are very encouraging about the ultimate sensitivity of CW-CRDS. The reader is warned, however, that other factors may come into play if such extreme limits are pursued. For example, in this calculation it has been assumed that the transition relaxation rate is faster than the cavity round-trip time, which is generally not the case in the mid-infrared.

It can been forseen that CRDS will play an increasing role in absorption measurements. Presently, absorption spectroscopy is a workhose for spectrochemical analysis. We believe that PCRDS offers the possibility of transforming this venerable Clydesdale draft horse into a quarter horse for robust, practical applications: moreover, CW-CRDS might spawn an Arabian thoroughbred racehorse for ultimate sensitivity applications, with outstanding limits of detection.

Chapter 4

Advanced Theory: Scattering Matrices

In this chapter, familiarity with linear systems theory and the superposition principle of resonator modes will be assumed. A scattering matrix approach which provides an identical model for CRDS as the differential equation approach of Martin, Paldus, and Zare [55] is provided here, along with simulation results.

4.1 Notation

The notation used throughout this section is based on the conventions given in reference [14]. However, because transverse cavity modes rather than plane waves [14] are used as the basis set, the scattering matrices differ significantly. Transmission matrices serve to relate the two sides of a linear system. This tranformation is a linear mapping between two vector spaces and thus can be mathematically described by a matrix once a basis is chosen for the input and output vector spaces. For an optical system, the transmission matrix transforms the input eletromagnetic (EM) wave from the domain space into an output EM wave in the range space (cf. figure 4.1).

Assuming that the input signal is a continuous wave at angular frequency ω, and that its tranverse mode distribution can be fully represented by a single transverse

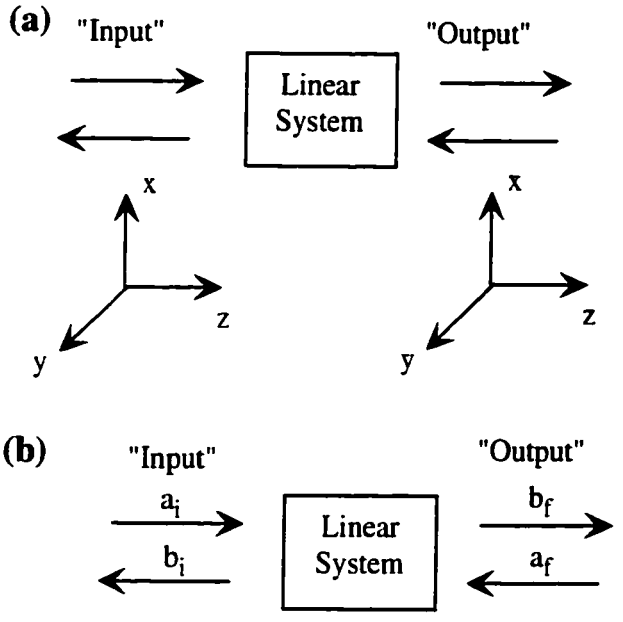

Figure 4.1: (a) Linear system with 'input' and 'output' waves, and (b) linear systems notation conventions.

mode,

$$E(x,y,z,t) = A\psi_{p,l}(x,y,z,t)e^{i(\omega t - kz)} + B\psi^*_{p,l}e^{-i(\omega t - kz)}, \tag{4.1}$$

then the domain space of the linear system can be represented by the basis set,

$$\begin{aligned} E^+_{z_i}(x,y,t) &= \psi_{p,l}(x,y,z_i)e^{i(\omega t - kz_i)} \\ E^-_{z_i}(x,y,t) &= \psi^*_{p,l}(x,y,z_i)e^{-i(\omega t - kz_i)}, \end{aligned} \tag{4.2}$$

where $E^+_{z_i}$ and $E^-_{z_i}$ are values of the EM field in a plane orthogonal to the direction of propagation, z, at coordinate z_i. A similar basis can be chosen for the range space, at coordinat z_f. The relation between the input and output EM field coordinates can then be described by a simple 2×2 matrix M,

$$\begin{pmatrix} A_f \\ B_f \end{pmatrix} = M \begin{pmatrix} A_i \\ B_i \end{pmatrix}, \tag{4.3}$$

which represents a specific linear transformation. In the following sections, the basis

coordinates will be written as.

$$\begin{array}{llll} basis & (E^+_{z_i}, E^-_{z_i}) & \rightarrow & coordinates \quad (b_i, a_i) \\ basis & (E^+_{z_f}, E^-_{z_f}) & \rightarrow & coordinates \quad (b_f, a_f) \end{array} . \tag{4.4}$$

For the case of multiple longitudinal mode excitation (e.g. short pulse), the simple two-dimensional vector space formalism must be replaced by a larger vector space that accounts for all the excited modes. If N longitudinal modes are excited, then the EM field components will be

$$E^{\pm}_{z,n}(x, y, t) = \upsilon^{(*)}(x, y, z)e^{\pm i(\omega_n t - k_n z)}. \tag{4.5}$$

where n denotes the nth longitudinal mode index. The basis set for the domain space is then

$$(E^+_{z_i,1}, E^-_{z_i,1}, E^+_{z_i,2}, E^-_{z_i,2}, \ldots, E^+_{z_i,N}, E^-_{z_i,N}),$$

while the basis set for the range space becomes

$$(E^+_{z_f,1}, E^-_{z_f,1}, E^+_{z_f,2}, E^-_{z_f,2}, \ldots, E^+_{z_f,N}, E^-_{z_f,N})$$

forming a $2N$-dimensional vector space. If more than the TEM_{00} is excited by the transverse EM field profile, then these additional transverse modes are included in the domain and range vector spaces, as above, with index n replaced by index pair (n, m) for the mth transverse mode corresponding to the nth longitudinal mode. The dimensions of the domain and range spaces is then $2NM$.

It is noted that in the previous sections, transverse modes possessed two indices $(p.l)$. By defininining an 'ordering' for these modes, is it possible to use a single index m and thereby simplify vector notation. One possible approach to this ordering is to use the following algorithm, where (p, l) and $(\tilde{p}, \tilde{l})$ are sets of mode indices:

1. if $2p + l > 2\tilde{p} + \tilde{l}$, then (p, l) is listed after $(\tilde{p}, \tilde{l})$,
2. if $2p + l = 2\tilde{p} + \tilde{l}$ and $l > \tilde{l}$, then (p, l) is listed after $(\tilde{p}, \tilde{l})$,
3. otherwise (p, l) is listed before $(\tilde{p}, \tilde{l})$.

This algorithm implies the following correspondence:

1	2	3	4	5	6	7	8	9	...
(0,0)	(0,1)	(1,0)	(0,2)	(1,1)	(0,3)	(0,4)	(1,2)	(2,0)	...

The basis set which includes both transverse and longitudinal modes can then be expressed as

$$E^{\pm}_{z,n,m}(x,y,t) = v^{(*)}_{p(m),l(m)}(x,y,z)e^{\pm i(\omega_{m,n}t - k_{m,n}z)}. \tag{4.6}$$

At this point, the coordinates of the input and output EM fields consist of a superposition of transverse and longitudinal modes at different angular frequencies. Any linear transformation will have a matrix representation in these two basis sets.

In the analysis presented here, coupling between different transverse or longitudinal modes is ignored, assuming that modes do not interact within the RDC, even in the presence of an absorber. Thus, all transmission matrices will appear as block-diagonal matrices, each block being two-dimensional. Were mode-coupling to occur (e.g. two-photon absorption under saturation conditions), then additional terms could be added to the transmission matrix in order to model this phenomenon (provided that coupling is independent of the magnitude of the fields). Thus, a RDC can be represented completely by a transmission matrix, once bases for the input and output planes have been defined. The output signal for any input signal can then be computed, and will automatically account for the wavelength dependence (e.g. mirror reflectivity response, absorption profile) of the cavity losses, since all wavelength-dependent effects are included in the discretized series of cavity mode frequencies.

4.2 Elementary Transmission Matrices

Analytical expression similar to those presented in reference [14] for the 2×2 matrix blocks are derived in this section for the different RDC components. The full block-diagonal cavity matrices are then generated from these 2×2 blocks, where each block corresponds to a specific transverse and longitudinal mode. The input EM fields used

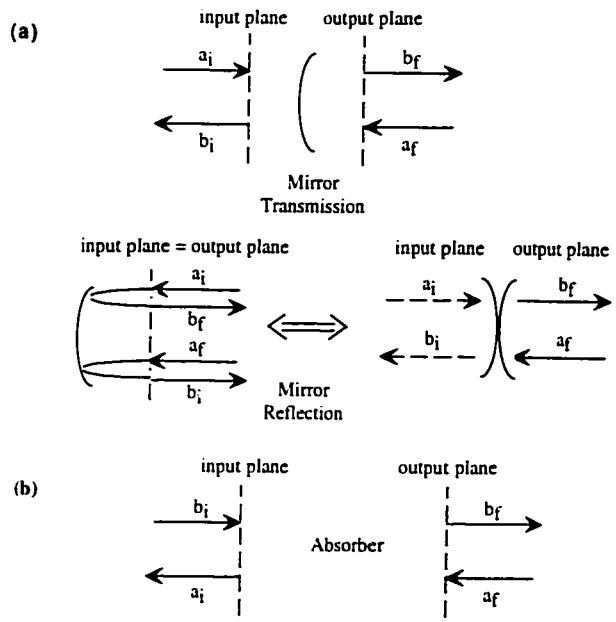

Figure 4.2: (a) Mirror transmission and reflection, and (b) absorption by a sample.

in this derivation are given by

$$E(x,y,t) = a_i E^+_{z_i,n,m}(x,y,t) + b_i E^-_{z_i,n,m}(x,y,t),$$

while the output EM fields are characterized by similar expressions.

4.2.1 Mirrors

Two different matrices are needed to model mirrors in an RDC: a matrix T, that describes transmission through a mirror, and a matrix, R, that describes reflection by a mirror. Both cases are shown in figure 4.2a. If r and t are the mirror reflection and transmission coefficients (for electric *field*), and the input and output planes are defined such that no additional phase shift is needed to account for the propagation of the field through the mirror, then the mirror transmission matrix T is given by

$$\begin{pmatrix} b_f \\ a_f \end{pmatrix} = \begin{bmatrix} -\frac{r}{t} & \frac{1}{t} \\ \frac{1}{t} & -\frac{r}{t} \end{bmatrix} \begin{pmatrix} b_i \\ a_i \end{pmatrix} = T \begin{pmatrix} b_i \\ a_i \end{pmatrix}. \tag{4.7}$$

The matrix that defines reflection from a mirror, effectively 'propagates' the field around the cavity. In this case, the input coordinates (a_i, b_i) give the field at position z_i and time t, while the output coordinates (a_f, b_f) represent the field at position z_i and time $t+\delta t$. Once again, assuming that reflection does not produce any additional phase shift in the output field (e.g. as would be the case for non-normal incidence, and can be included in the model as a simple $e^{i\psi_{cav}}$ factor), the reflection matrix R is given by

$$\begin{pmatrix} b_f \\ a_f \end{pmatrix} = \begin{bmatrix} 0 & -r \\ -\frac{1}{r} & 0 \end{bmatrix} \begin{pmatrix} b_i \\ a_i \end{pmatrix} = R \begin{pmatrix} b_i \\ a_i \end{pmatrix}. \tag{4.8}$$

4.2.2 Absorbers

For an absorber producing α intensity losses, as shown in figure 4.2b, the transmission matrix (which depends on wavelength) is given by:

$$\begin{pmatrix} b_f \\ a_f \end{pmatrix} = \begin{bmatrix} 0 & \sqrt{1-\alpha} \\ \frac{1}{\sqrt{1-\alpha}} & 0 \end{bmatrix} \begin{pmatrix} b_i \\ a_i \end{pmatrix} = A \begin{pmatrix} b_i \\ a_i \end{pmatrix}. \tag{4.9}$$

4.3 RDC Transmission Matrices

Two equivalent methods for deriving the RDC transmission matrix will be presented. The first method is a propagation method similar to reference [48], while the second is a 'steady state' method, similar to that used to derive the RDC transfer function in reference [94]. The resulting transmission matrices are identical. Calculations will be performed using only 2×2 matrices, since these blocks multiply independently in the full block-diagonal matrix system.

4.3.1 Propagation Method

In a high-finesse resonator, a given mode can either be considered as propagating back and forth between two mirrors, or propagating along an infinite sequence of resonators [94]. The ouput field is a sum of the fields at the output of the RDC after one, or several, roundtrips, as shown in figure 4.3a. The components of these

fields (in a given basis set) can be expressed as the product of a 2×2 matrix and the coordinates of the input field in the basis associated with the input plane. Because all the components of the output fields are expressed in different bases (even though in reality they correspond to the same output plane in real space), i.e. for straight propagation, $z_f = \frac{d}{2}$, and after g round-trips, $z_f = \frac{d}{2} + 2gd$, these fields must be transformed into the same basis set, in order to obtain the total output field.

By choosing the plane $z = \frac{d}{2}$ (output plane) for the common output basis, components are given by

$$\begin{aligned} E^{+}_{m,n}(x,y,z,t) &= E^{+}_{\frac{d}{2},m,n}(x,y,t)e^{-2i(2p+l+1)tan^{-1}(\frac{d}{2z_R})} \\ E^{+}_{m,n}(x,y,z,t) &= E^{-}_{\frac{d}{2},m,n}(x,y,t)e^{2i(2p+l+1)tan^{-1}(\frac{d}{2z_R})}, \end{aligned} \tag{4.10}$$

and the phase shift accrued over a single cavity trip cancels out. Consequently, if (A, B) are coordinates of the field in the $(E^{+}_{(2g+1)\frac{d}{2},m,n}, E^{-}_{(2g+1)\frac{d}{2},m,n})$ basis, then its coordinates $(\tilde{A}, \tilde{B})$ in the new $(E^{+}_{m,n}, E^{-}_{m,n})$ basis are

$$\begin{pmatrix} \tilde{A} \\ \tilde{B} \end{pmatrix} = \begin{bmatrix} e^{2i(2p+l+1)\tan^{-1}(\frac{d}{2z_R})} & 0 \\ 0 & e^{-2i(2p+l+1)\tan^{-1}(\frac{d}{2z_R})} \end{bmatrix} \begin{pmatrix} A \\ B \end{pmatrix} = P \begin{pmatrix} A \\ B \end{pmatrix}, \tag{4.11}$$

where matrix P is given by

$$P = \begin{pmatrix} e^{-i\phi} & 0 \\ 0 & e^{i\phi} \end{pmatrix}$$

while $\phi = (2p + l + 1)\tan^{-1}(\frac{1}{2}d/z_R)$.

The phase shift introduced in matrix P seems to corresponds to the phase shift added to a wave propagating along the z-axis only when $r = 0$ and $\theta = 0$. Because each transverse (longitudinal) mode is an eigenfunction of the cavity, and the basis set is comprised of transverse (longitudinal) modes and thus reproduces itself after a round- trip up to a scaling constant, the phase shift added to each point of the transverse mode will be the same as for the $r = 0$ and $\theta = 0$ point. It should also be noted that the transverse mode expressions must be changed when they are used to calculate fields beyond the plane $z = \frac{d}{2}$, to account for the fact that these modes

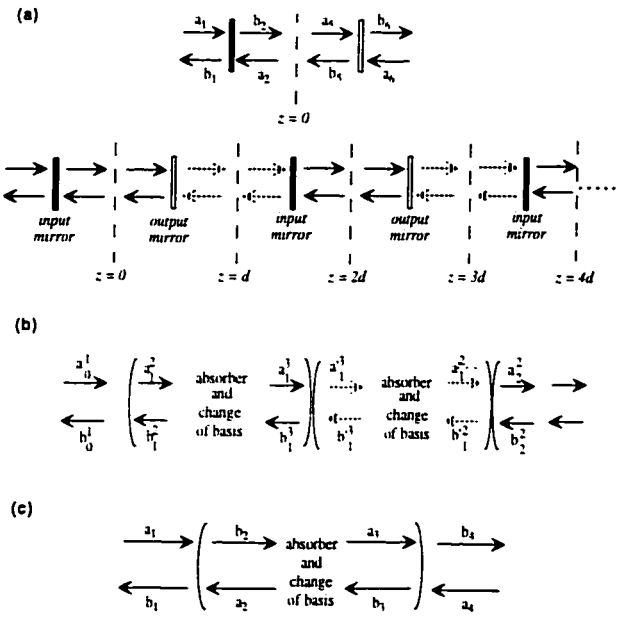

Figure 4.3: (a) Wave propagation mode, and (b) steady-state wave model.

are only defined within the resonator. This is accomplished by a simple coordinate change.

The transmission matrix of the RDC is obtained by propagating the input field, as shown in figure 4.3b. Here, a_1^0 is the forward propagating wave, b_1^0 is the reflected wave satisfying the condition $b_1^0 = ra_1^0$, and $a_2^1 = 0$, because no backwards traveling wave exists at this point. Thus,

$$x_2^1 \begin{pmatrix} b_2^1 \\ a_2^1 \end{pmatrix} = T \begin{pmatrix} b_1^0 \\ a_1^0 \end{pmatrix} = T \begin{pmatrix} ra_1^0 \\ a_1^0 \end{pmatrix} = Tx_0^1.$$

In order to properly account for the absorber matrix, which has reversed basis coordinates (i.e. $(E^+_{-\frac{d}{2},m,n}, E^-_{-\frac{d}{2},m,n})$ instead of the usual $(E^-_{-\frac{d}{2},m,n}, E^+_{-\frac{d}{2},m,n})$ which was used to ease physical understanding of how this matrix is generated), a completely unimodular row interchange matrix C,

$$C = \begin{bmatrix} 0 & 1 \\ 1 & 0 \end{bmatrix},$$

must be introduced before and after the absorber matrix. Note that a modified absorber matrix $\tilde{A} = AC$ could be used instead to simplify this analysis. Then at the RDC output mirror, after the first round-trip, the forward propagating wave, $x_3^1 = CPACx_2^1$, is reflected by the mirror, $\tilde{x}_3^1 = Rx_3^1$, where $\tilde{x}_3^1$ is a backward propagating wave. The output of the cavity at this point, x_4^1, is given by the transmitted sum of the forward and backward propagating waves, $x_4^1 = T^{-1}(x_3^1 + \tilde{x}_3^1)$. The latter relation will be successively used to calculate the transmission matrix of the cavity. An alternative (and simpler) approach to calculating x_4^1 is to argue that there is only a forward transmitted component (i.e. $a_4^1 = 0$), so that:

$$x_4^1 = \begin{bmatrix} 0 & t \\ 0 & 0 \end{bmatrix} x_3^1 = Qx_3^1.$$

The reflected wave now travels backwards inside the cavity. By exploiting arguments similar to those used above, we have that $\tilde{x}_2^1 = (CPAC)^{-1}\tilde{x}_3^1$. The wave $\tilde{x}_2^1$ is now reflected by the input mirror into $x_2^2 = R\tilde{x}_2^1$. Using the iterative equations

$$\begin{aligned} & x_2^1 = Tx_1^0 \\ \forall i \geq 2 \quad & x_2^i = R\tilde{x}_2^1 \\ \forall i \geq 3 \quad & \tilde{x}_3^i = CPACx_2^i \\ \forall i \geq 3 \quad & \tilde{x}_3^i = Rx_3^i \\ \forall i \geq 3 \quad & \tilde{x}_2^i = (CPAC)^{-1}\tilde{x}_3^i \\ \forall i \geq 3 \quad & x_4^i = Qx_3^i, \end{aligned} \tag{4.12}$$

it can be shown that for x_1^0, the total transmitted field $x_4 = \sum_i x_4^i$ is

$$x_4 = \begin{bmatrix} 0 & t \\ 0 & 0 \end{bmatrix} (CPAC)(I - M)^{-1}Tx_1^0 = T_{cav}x_1^0, \tag{4.13}$$

where $M = R(CPAC)^{-1}R(CPAC)$, and I is the identity matrix. It should be noted that x_1^0 is purely a mathematical entity used for convenience and is not physically exist. Were one to measure the field at the input mirror, the quantity $x_1 = \sum_i x_1^i$ would be obtained. Thus, x_0^1 is simply the freely propagating input field to which

a backwards propagating wave corresponding to the reflection of this field from the input mirror has been added. Therefore, the matrix T_{cav} is not the physical transfer matrix of the system that relates the input field to the output field. Nonetheless, matrix T_{cav} is very simply and efficiently computed, and yields the correct output field for x_0^1 corresponding to an arbitrary input field.

4.3.2 Steady-State Approach

The fields used in this derivation are assumed to be standing rather than traveling waves, and the analysis is simply a steady state analysis of the cavity: the matrix relations which exist between all intermediate steady-state fields inside the cavity at different planes are used to relate the input and output fields. Once again, all modes are assumed to be mutually independently.

Assuming that the basis set developed in the previous section is used, i.e. that the fields of the cavity are expressed using coordinates (a_k, b_k) for basis elements $(E^+_{m,n}, E^-_{m,n})$, as shown in figure 4.3c, the following set of equations holds,

$$\begin{aligned} x_2 &= Tx_1 \\ x_3 &= CPACx_2 \\ x_4 &= T^{-1}x_3. \end{aligned} \tag{4.14}$$

Therefore, the input and output steady-state fields can be related as

$$x_4 = T^1CPACTx_1.$$

In order to compute the output field $x_4 = (a_4 b_4)^T$ from the input field $x_1 = (a_1 b_1)^T$, the linear system must be rearranged to solve for b_1 and b_4 because only a_1 and a_4 are known. If

$$T^{-1}CPACT = \begin{bmatrix} \alpha & \beta \\ \gamma & \delta \end{bmatrix},$$

then equivalently

$$\begin{pmatrix} b_4 \\ b_1 \end{pmatrix} = \begin{bmatrix} \frac{\alpha}{\gamma} & -\frac{\alpha\delta-\beta\gamma}{\gamma} \\ \frac{1}{\gamma} & -\frac{\delta}{\gamma} \end{bmatrix} = \begin{pmatrix} a_4 \\ a_1 \end{pmatrix}. \tag{4.15}$$

Although a transfer function has been derived for the cavity, it should be recalled that the fields represented here are steady-state fields, and therefore unknown for a given input at time $t = 0$. Were any two components of x_1 and x_4 known, then this system could be very simply solved. However, this is generally never the case. If should also be noted that the fields employed here physically exist in the system, even though they cannot be measured without perturbing the system (e.g. x_1 could be measured if a detector could be placed just left of the input mirror).

Finally, it should be noted that the two approaches for deriving the RDC transmission matrix are identical, even though they do not relate the same fields (one is steady state, the other is a mathematical composition of the real field and its reflection). A little algebra yields the relations

$$b_4 = \frac{t^2\sqrt{1-\alpha}e^{i\phi}}{1-(r\sqrt{1-\alpha}e^{i\phi})^2}a_1 \tag{4.16}$$

and

$$-\frac{\alpha\delta-\beta\gamma}{\gamma} = \frac{t^2\sqrt{1-\alpha}e^{i\phi}}{1-(r\sqrt{1-\alpha}e^{i\phi})^2}. \tag{4.17}$$

The propagation method is simple to implement numerically, because it predominantly involves only 2×2 matrix multiplication. However, the propagation method is not completely intuitive, because physical fields are not manipulated (i.e. the x_k^i cannot be directly measured, and only their sums can be detected). The steady-state method, despite its intuitive appeal, is not easily implemented as numerical code. Moreover, were mode-coupling to occur in the system, then the equivalence between the two methods might no longer hold (i.e. the equivalence has assumed a block-diagonal form of all matrices), and would certainly have to be demonstrated in specific cases. However, if the two methods do remain equivalent (or if it is simply assumed that they do), then the propagation method still remains much easier to implement numerically.

4.4 Simulations

The general structure of the algorithm used to perform simulations is first presented:

1. An input signal is defined and decomposed over multiple transverse modes. The input field is expressed as:$E(r,\theta,z,t) = \sum_{p,l} \psi_{p,l}(r,\theta,z)e(t)$, where $e(t)$ is the time variation of the signal,

2. A time vector$x(i)$, discretizing $e(t)$, is defined for sampling size N: $x(i) = e(t)|_{t=\frac{i-1}{2N-1}\Delta t}$, $\forall i \in [1, 2N]$.

3. The discrete Fourier-transform (FT), $ft_x(j)$ is calculated from $x(i)$.

4. For each transverse mode (m) excited, the cavity transfer function $F_m(j)$ is computed at all frequencies of $ft_x(j)$.

5. The FT of each mode's output field is calculated: $ft_{y_m}(j) = F_m(j)ft_x(j)$.

6. The discrete inverse FT is computed for each mode's output field, yielding the time-dependent vector $y_m(t)$.

7. The total output intensity for an ideal detector is calculated by summing the square of the magnitude of all $y_m(t)$, because the modal basis set is orthonormal. Thus, $I_{out}(t) = \sum_m \|y_m(t)\|^2$.

8. The transverse mode output intensity distribution in the (r,θ) coordinates is defined and calculated as the time-averaged total transverse intensity pattern.

The FT is computed using the fast FT algorithm, whose input is an array of points in time and whose ouput is an array of the same number of points in frequency space. The output array contains the values of the coefficients of the Fourier series corresponding to the input $e(t)$. If the frequency of the Fourier series is small enough, then it is a good approximation to the actual FT of $e(t)$. For a time interval Δt, and $2N$ sampling points, the sampling time is $\delta t = \frac{\Delta t}{2N-1}$, the frequency interval is $\Delta\omega = \frac{2\pi}{\Delta t}(2N-1)$, and the sampling frequency of the FT is $\delta\omega = \frac{2\pi}{\Delta t}$.

The cavity and computational parameters defined in table 4.1 were used to generate the decay waveforms shown in figure 4.4. The decays shown are indeed exponential, and after fitting, a total absorption loss of $1-r+\alpha_{abs} = 1.08\times10^{-4}$ was obtained, in agreement with the parameter value of 1.10×10^{-4}. It should also be remarked that the output decay waveform consists of a series of consecutive 'pulses' separated by the RDC round-trip time, as expected for single mode excitation. One surprising feature is that the first output pulse is larger than expected (i.e. $\sqrt{1-r^2}(1-\alpha_{abs})\sqrt{1-r^2}$ = 0.001 compared to 0.0015), and the second output pulse is larger still. However, if the fact that the Gaussian pulse FWHM is equal to the RDC round-trip time is recalled, then the output field will actually be superposition of one pulse with the tails of several other delayed pulses, so that the simple bullet model perception fails.

The decay waveforms generated using parameters defined in table 4.1, but with two longitudinal RDC modes corresponding to the same transverse mode (TEM_{00}) is illustrated in figure 4.5. In this case, the laser wavelength was shifted by half a free spectral range, $\lambda_{las} = 830 + 7\times10^{-4}$ nm, so that the FT of the Gaussian pulse overlaps two longitudinal modes. A very strong beating between the two modes can be observed with an expected period equal to the RDC round-trip time. For a detector with a small bandwidth, this mode beating will not be observed, and the effective decay waveform will appear to have been averaged. If the decay rate for both longitudinal modes is identical (i.e. a broad absorber), then the averaged waveform will be exponentially decaying with the correct rate. However, if the absorption losses differ between the modes, the averaged waveform will not be purely exponential, resulting in a loss of sensitivity, even if mode beating is not observed. This is yet another compelling argument for performing ultrahigh sensitive CRDS with narrowband, CW lasers.

Finally, the effects of mode beating between two transverse modes are illustrated in figure 4.6, where the parameters of table 4.1 were used, but in this case both TEM_{00} and TEM_{01} transverse modes were excited, at two longitudinal mode frequencies. As was noted earlier, because transverse modes are defined to be orthonormal in space, if all the light from the RDC is collected and the detector frequency response is uniform over the transverse mode frequency separation, then no mode beating

(a)

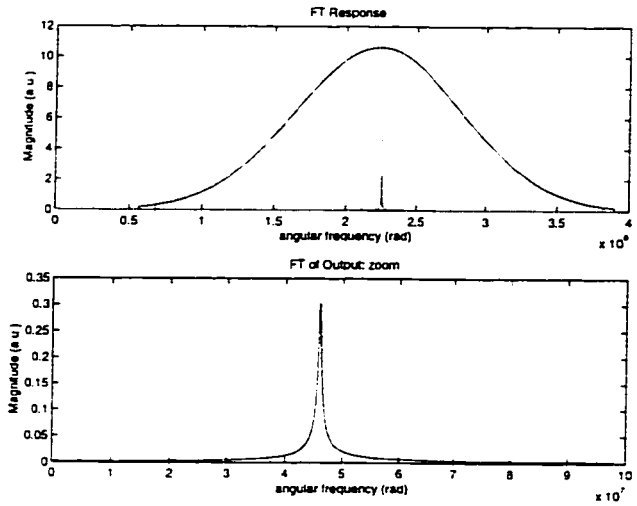

(b)

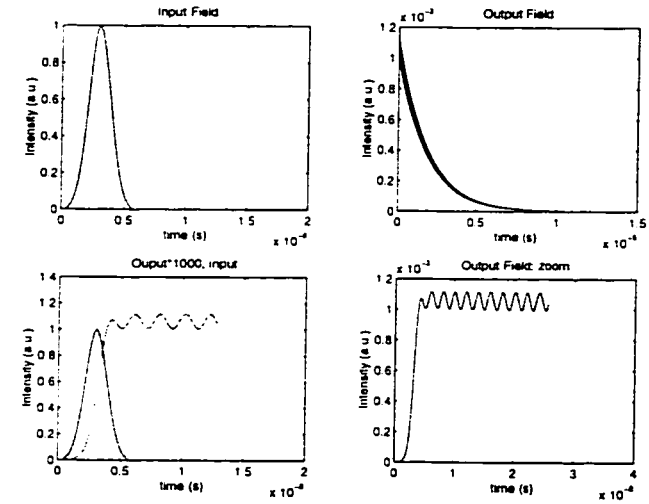

Figure 4.4: (a) FT space excitation picture, and (b) magnitude of the input field (left top corner), magnitude of the output field (right top corner), magnitude of the input and output field for very small times where the output field is magnified 1000 times (left bottom corner), detail of the magnitude of the output field (right bottom corner). Only a single longitudinal and transverse mode is excited.

(a)

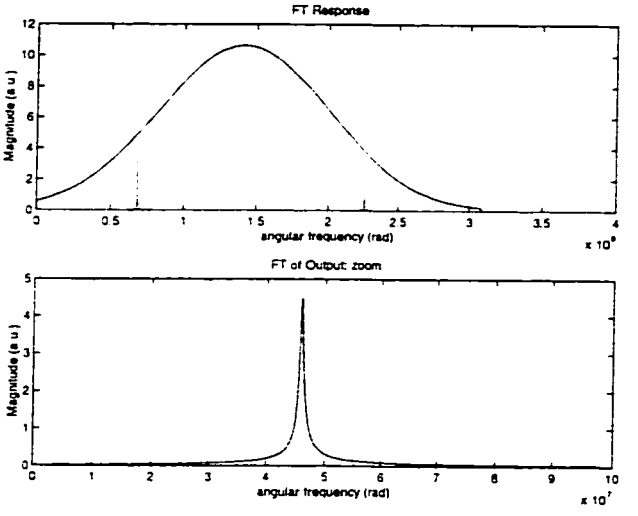

(b)

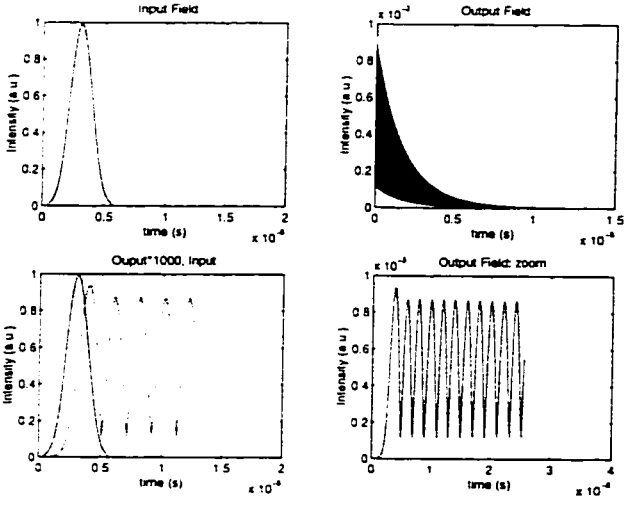

Figure 4.5: FT space excitation picture, and (a) magnitude of the input field (left top corner), magnitude of the output field (right top corner), magnitude of the input and output field for very small times shere the output field is magnified 1000 times (left bottom corner), detail of the magnitude of the output field (right bottom corner). Two longitudinal modes corresponding to a single transverse mode (TEM_{00}) are excited.

Table 4.1: Parameter set used in simulations of CRDS using a Gaussian input beam, for a typical physical system. HWHM=half width half maximum, t_{rt}=cavity round-trip time.

Parameter	Symbol	Value
RDC length	d	0.6 m
Mirror radius	r_m	1.27 cm
Mirror radius of curvature	r_c	1.0 m
Mirror Intensity Reflectivity	R	99.9%
Absorber center wavelength	λ_{abs}	830 nm
Absorber linewidth	σ_{abs}	∞
Absorption loss (max)	α	10^{-4}
Laser wavelength	λ_{las}	$830 + 4\times10^{-4}$ nm
Gaussian pulse HWHM	σ_t^2	$\frac{t_{rt}}{2}$
Modes excited	m, n	$m = 0, n = 1, \ldots, 3$
Time interval	Δt	420 μs
Discretization Number	2N	2^{21}=2,097,152

between transverse modes will be observed. This situation was assumed to exist for an 'ideal' detector, as illustrated in figure 4.6, where the topmost waveform shows only longitudinal mode beating. However, if the detector does not collect all the light, significant transverse mode beating, in addition to the longitudinal mode beating, will occur (cf. figure 4.6) and may not be easily separated from the exponential decay. Because the period of the transverse mode beating can be on the order of the decay constant, and the resulting output field magnitude is a decaying exponential with a superposed sine wave, obtaining an accurate fit of the decay rate is difficult, so that CRDS sensitivity is compromised.

Preliminary investigations of the effects of laser phase noise were also carried out using the scattering matrix formulation. These show that phase noise or equivalently, laser frequency noise, is translated into intensity noise by the RDC transfer function, and produces excess intensity noise on the output decay waveform. However, the simulations produced a noise level that was strongly dependent on the Nyquist sampling frequency of the FT if more than one longitudinal mode in the RDC was excited. Therefore, the accuracy of the simulations, and their physical validity, still

(a)

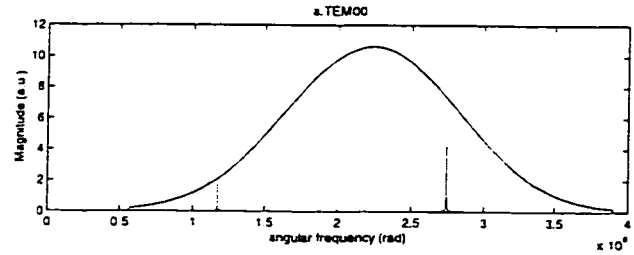

(b)

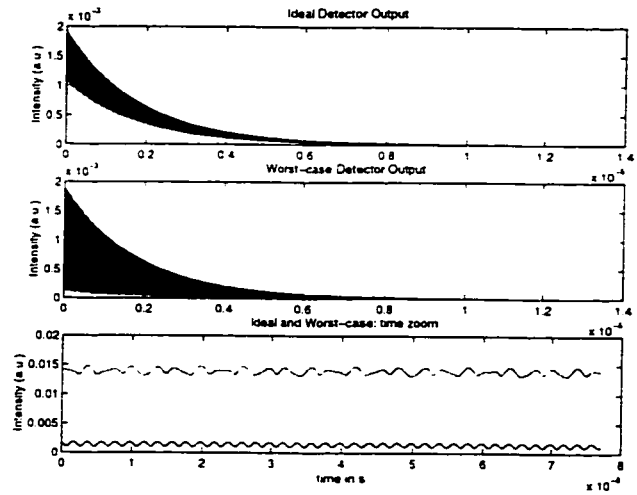

Figure 4.6: (a) FT space excitation picture, and (b) magnitude of the output field (top), of an ideal detector, magnitude of the output field (middle) for a bad detector, detail (bottom) in time of the magnitude of the output field for a good (bottom waveform) and bad (bottom waveform) detector. Two transverse modes (TEM_{00} and TEM_{01}) corresponding to two longitudinal mode frequencies are excited.

remain questionable, and will not be presented here.

4.5 Experimental Results

As was shown by Martin *et al.* [55], CRDS experiments generally involve pulses that are much broader in bandwidth than expected from the Fourier transform limit, indicating that the phase of the electric field forming the pulse undergoes random phase fluctuations. These fluctuations will reduce any coherent superposition effects of the pulse with itself in the cavity. However, the pulses generated by an OPO system are almost Fourier-transform-limited, so that for pulses with a 4 ns duration, the bandwidth is 160 MHZ, and the coherence length of the radiation is on the order of few meters, that is, a few cavity roundtrips.

An absence of phase fluctuations is expected to allow coherent effects such as mode beating to occur. In fact, several beating effects in the CRDS waveforms were experimentally observed for a single-mode pulsed light source. The examples presented here clearly demonstrate that for Fourier-transform-limited pulsed sources with long coherence lengths, carefully designed cavity geometries, and accurate control of mode matching the injected light to the cavity are crucial in obtaining purely exponential decay waveforms.

As discussed earlier, when a coherent pulse overlaps two or more cavity modes, the output signal will be amplitude modulated; this effect is called mode beating. The beat period is determined by the frequency separation of the cavity modes excited. Depending on cavity geometry, the existence and excitation of higher order transverse cavity modes can lead to beat frequencies ranging from zero to a few hundred MHz.

Figure 4.7a presents a schematic of the experimental setup used to obtain decay waveforms from a cavity configuration having 2.0 m radii of curvature mirrors and a length of 0.41 m. Assuming that both longitudinal and transverse $\mathrm{TEM}_{m}n$, $m, n \in -2, .., 2$, modes are excited, the inset of figure 4.7c shows the mode frequency positions in the cavity: a large longitudinal mode spacing of 76 MHz that produces oscillations with a 14 ns period, and a small transverse mode spacing of 14 MHz that modulates the decay with a period of 70 ns. Thus, the experimental ring-down decay waveform

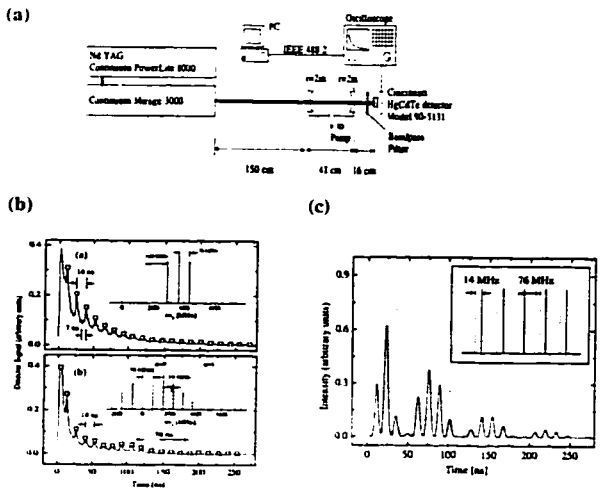

Figure 4.7: (a) Setup for mode-beating demonstration, (b) experimental decays, and (c) resonator theory predicted mode-beating.

in figure 4.7b is modulated by one or two different beat frequencies (depending on whether more than one transverse mode is excited).

Under these conditions, a problem in extracting the ring-down decay time constant will arise, as was discussed earlier. It is relatively straightforward to average out the high frequency beating modes with a low pass filter, but it is difficult to eliminate the slow amplitude modulation caused by transverse mode beating. Because precise numerical fitting of sinusoidally modulated exponentials requires an exact knowledge of the cavity mode spacings, significant error would be introduced into any ring-down times thus obtained. It is therefore very important to design and mode-match cavities to avoid such closely spaced transverse-mode patterns.

Numerical solutions [55] for two different modal spectra are given in figure 4.7c. If only a spectral comb of modes separated by 76 MHz is considered, a purely exponential decay modulated only by the corresponding fast beat period is observed (dotted line). If it is assumed that two such combs exist and are shifted by 14 MHz from one another, an additional modulation with a slow period of 70 ns appears in the decay (solid line). The high modulation index observed in the theoretical mode beating curves is a consequence of the assumption that an ideally monochromatic

electric field is injected into the cavity and of the simplification that filling factors are identical for all modes considered. Clearly, this simple spectral model verifies that the excitation of closely spaced modes substantially alters the fundamental exponential decay.

Chapter 5

CRDS in Hostile Environments

The chemistry taking place in highly luminous environments, such as arcs, plasmas, and flames, is often hidden by radiant background interference. Morever, direct probing of such hostile environments is generally difficult owing to the high temperatures and pressures that characterize them. Noninvasive optical methods are commonly used, but are often limited by various drawbacks. For example, emission spectroscopy can only provide information on electronically excited species and is therefore 'blind' to ground-state species [1].

One promising strategy is to use a coherent laser beam as the carrier of information about the ground-state population distribution. This technique has the advantage that the intensity of the incident luminous source falls off with the square of the distance from the source, so that its interference can be significantly supressed by spatial filtering in which the coherent signal is captured. The success of coherent anti-Stokes Raman spectroscopy (CARS) [72] and degenerate four-wave mixing (DFWM) [53, 93] in investigating hostile environments is an example of this advantage. However, the quantitative interpretation of both techniques is often limited by the need to understand in great detail the different contributions to these nonlinear spectroscopies. In addition, both CARS and DFWM depend on the square of the species' single quantum state number density, which precludes an easy extension of these techniques to very low sensitivity limits.

In the present work, we exploit the sensitivity and versatility of CRDS to study

the ground-state molecular species of water vapor in atmospheric-pressure flames. We investigate the overtone transitions of the O–H vibrations between 810 and 820 nm, with the aim of demonstrating that CRDS can detect weak transitions of reaction products (e.g. combustion products) in hostile environments. The overtone transitions are used because high reflectivity mirrors, as well as high sensitivity and low-noise detectors are not readily available. Furthermore, we have used an OPO laser source in the visible to avoid the problem of long fluorescence tails associated with Ti:sapphire lasers, which makes the latter more difficult to use in CRDS. We also show that this technique remains relatively insensitive to backgrounds radiating over the entire detector responsivity range, as well as to media presenting nonuniformly dense optical paths along the ring-down resonator principal axis.

5.1 Apparatus and Experimental Method

A Nd:YAG laser-pumped optical parametric oscillator (OPO) is used to generate nearly Fourier-transform-limited Gaussian light pulses. The pulses are 4 ns in duration and run at a 10 Hz repetition rate. The laser (Continuum Mirage 3000) has an upper linewidth limit of 500 MHz (0.017 cm^{-1}). Infrared radiation is generated by the OPO as follows (cf. figure 5.1a): the master oscillator (MO) KTP crystal is pumped with frequency-doubled, single-mode 532 nm light from a single-mode-seeded Nd:YAG pulsed laser; the MO resonator consists of two mirrors and a grating in a Littrow configuration, which produces single-mode operation; the first order grating deflection is resonantly enhanced in the resonator, while the zeroth order grating deflection provides the MO near-infrared output. This MO output serves as the seed radiation for the optical parametric amplifier stages that mix it with 532 nm and subsequently 1064 nm radiation in order to produce a signal (1.45 μm to 2.12 μm) and an idler (2.12 μm to 4.0 μm). In this experiment, the output from the parametric OPA 1, which is tunable from 710 nm to 850 nm and produces 15 mJ of energy, is used (cf. figure 5.1a).

The MO output is directed onto a ringdown cavity (RDC), along with a collinear HeNe alignment laser (c.f. figure 5.1b). The RDC is a linear Fabry-Perot resonator,

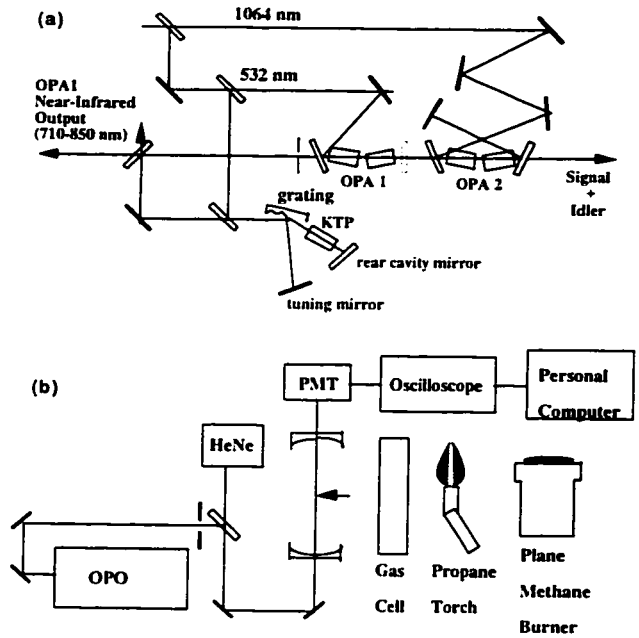

Figure 5.1: (a) Generation of near-infrared light in the master oscillator stage of an optical parametric oscillator; (b) experimental setup used to measure water vapor in a gas cell, in a propane torch flame and in a plane methane burner flame.

consisting of two concave mirrors (Newport:10CV00.SR.40F), each having a 99.98% reflectivity and a 1 m radius of curvature. The cavity length is chosen according to Meijer [57], such that a quasi-continuum mode-structure is obtained, allowing high resolution scans to be performed without loss of spectral information. Output radiation from the RDC is detected using a near-infrared photomultiplier tube (PMT) with a responsivity from 160 nm to 930 nm (Hamamatsu: R943-02), peaking between 300 nm and 850 nm. The signal is digitized and averaged on an oscilloscope (HP: 54510A. 1GSa/s with 20 single-shot averaging). The logarithm of the ringdown decay is analyzed on a personal computer using a linear least squares fit.

For measurements of water vapor in a closed environment, the two mirrors are mounted as windows (41.5 cm separation) on vacuum cell flanges, thereby sealing the ends. Flexible bellows fixed in gimbal mounts (MDC: FGC-275-M) allow adjustment of the mirrors with micrometer screws. The cell is evacuated with a rotary pump to a residual pressure of 5 mTorr before being filled to a specific pressure with water

vapor. For measurements of water vapor generated in a propane torch flame, the central segment of the vacuum cell is removed and replaced with a mount holding the torch, such that the center of the flame is positioned at the height of the RDC axis. Each half segment of the vacuum cell is tapered down from a 1.5" flange to a 5 mm aperture stainless steel tube, in order to reduce mirror degradation caused by exposure to the flame, and to limit the presence of atmospheric water vapor in the ringdown path. A dry nitrogen gas purge is flowed from the mirrors to the flame to minimize further mirror contamination by water vapor, room dust, soot, and heating by the torch. This purge also eliminates absorption losses caused by water vapor in the ambient atmosphere. The nitrogen flow velocity is adjusted to minimize the shear layer mixing and maintain homogeneity of the flat flame. For measurements of water vapor produced by a plane methane flame, the methane burner is placed at the center of the RDC. Its position relative to the RDC axis is controlled with a variable height mount.

In all combustion experiments, appropriate evacuation of the product gases is achieved using an overhanging duct. The propane flame is generated by igniting flowing propane from a soldering torch (BenzOmatic Propane Fuel Cylinder) and by adjusting the propane flow rate until a controllable burn is achieved. No air flow, other than that occurring in the ambient environment, is provided to the flame. The 5 cm tall, 1 cm diameter propane flame has a teardrop shape and shows the three typical flame temperature regions: a light blue, low-temperature region near the torch nozzle, a bright yellow, high-temperature region at the flame tip, and a moderate-temperature (ca. 2000 K), blue region elsewhere. Flame height is adjusted until a known region intersects the CRD axis (i.e., the HeNe alignment beam).

The plane flame is generated in a 7 cm diameter water-cooled Meker type [54] burner, shown in figure 5.2. Both methane and air are supplied at room temperature (293 K) and monitored with calibrated flow meters (Mathieson). Industrial grade (> 99.9% purity) methane and (> 99% purity) air are mixed to achieve the desired stoichiometry of ϕ=1.1, where

$$\phi = \frac{(fuel flow rate)/(air flow rate)}{(fuel flow rate)/(air flow rate)_{stoichiometric}} \tag{5.1}$$

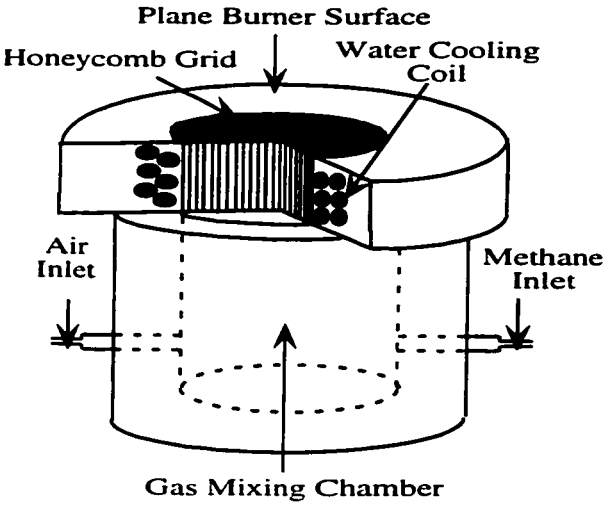

Figure 5.2: Schematic of Meker type burner used in flat flame experiment.

i. e., $\phi > 1$ is a fuel rich flame. In these studies, optimal flame stability was obtained with 1.289 slpm methane and 11.15 slpm air flow rates (inlet cold flow velocity of 5.4 cm/s), and resulted in a flat flame luminous zone with minimal curvature.

5.2 Results and Discussion

Using an optical parametric oscillator light source for conventional pulsed CRDS, shown in figure 5.1, we were able to obtain spectra of water vapor in ambient air, at the center of a propane torch flame, and at various heights of a flat flame methane-air burner, as shown in figure 5.4. All measurements were carried out at atmospheric pressure, so that all lines were pressure broadened to at least several GHz. After background subtraction, no baseline adjustments have been made.

Overall, our spectra compare favorably in absolute frequency, linestrength, and linewidth, to those generated using the HITRAN96 and HITEMP databases [84]. HITRAN is an acronym for HIgh Resolution Transmission molecular AbsorptioN database, while HITEMP is the HIgh TEMPerature equivalent of HITRAN for temperatures ranging from 1000°C to 1500°C (http://www.hitran.com). Using these

Table 5.1: Line assignments for water vapor hot band transitions from (J,K_a,K_c) to (J',K_a', K_c').

Line	Wavenumber(cm^{-1})	Vibrational Band	(J',K_a',K_c')←(J,K_a,K_c)
h1	12275.331	211	(909) ← (808)
h2	12285.707	310	(21 1 21) ← (20 1 20)
h3	12291.052	211	(624) ← (523)
h4	12294.906	211	(817) ← (716)
h5	12296.342	211	(15 1 15) ← (14 1 14)
h6	12304.194	211	(918) ← (817)
h7	12306.450	211	(743) ← (642)

databases in addition to the extensive tabulation of near-infrared water lines in Toth [101] and Flaud [26], we were able to assign all lines at 300 K and most (c.a. 98%) of the lines at high temperatures (> 1000 K) in the flames. Over our scanning range, we primarily observed rotational branches from the $2\nu_1 + \nu_2 + \nu_3$ vibrational band, in particular the P_{01}, Q_{01}, and R_{01} branches, but we also recorded rotational lines from the $\nu_1 + \nu_2 + 2\nu_3$ and $3\nu_1 + \nu_2$ vibrational bands. Spectral assignments corresponding to lines shown in figures 5.3 and 5.4 are listed in tables 5.1 and 5.2. The notation used to identify a specific rotation line is (J, K_a, K_c), where K_a is the value of the quantum number $|K|$ for the limiting prolate symmetric top with which the rotational level correlates, while K_c is the value of $|K|$ in the oblate rotor limit. For additional information on these transitions (e.g. line intensity, lower state energy, pressure-broadening coefficients, etc.), the reader is referred to the HITRAN96 and HITEMP databases, as well as tabulations by Toth [101] and Flaud [26].

The emergence of 'hot bands' between 813 and 815 nm in the flame spectra is illustrated in figure 5.3. A more detailed comparison of spectra taken at various heights above the flat flame methane-air burner is presented in figure 5.4. Changes in population among rotational states within the $2\nu_1+\nu_2+\nu_3$ vibrational band occur as detection moves farther away from the burner surface and the water vapor generated by combustion cools. At higher temperatures, rotational states with higher angular quantum number J become populated at the expense of lower J states, as expected

Table 5.2: Line assignments for water vapor transitions (J,K_a,K_c) to (J',K_a',K_c'). Doublets are listed under one reference number; primes indicate weaker lines.

Line	Wavenumber(cm^{-1})	Vibrational Band	$(J',K_a',K_c')\leftarrow(J,K_a,K_c)$
1	12212.070	211	(303) ← (202)
2	12218.829	211	(322) ← (221)
3	12223.804	211	(414) ← (313)
4	12223.848	211	(321) ← (220)
5	12224.682	211	(312) ← (211)
6	12226.101	211	(484) ← (303)
7	12236.560	211	(515) ← (414)
8	12237.466	211	(423) ← (322)
9	12238.312	211	(505) ← (404)
10	12244.719	211	(413) ← (312)
11	12248.020	211	(422) ← (321)
12	12248.579	211	(616) ← (575)
13	12249.390	211	(686) ← (505)
14	12254.518	211	(524) ← (423)
15	12259.602	211	(717) ← (616)
16	12260.995	211	(514) ← (413)
17	12262.813	211	(533) ← (432)
18	12267.038	211	(625) ← (524)
18'	12267.028	211	(542) ← (441)
19	12268.998	211	(808) ← (707)
20	12270.814	211	(523) ← (422)
21	12272.276	310	(625) ← (514)
22	12275.935	211	(919) ← (818)
23	12278.720	211	(615) ← (514)
24	12280.663	211	(726) ← (625)
25	12282.104	211	(10 0 10) ← (909)
26	12286.893	211	(541) ← (642)
27	12289.131	211	(633) ← (532)
28	12291.046	211	(624) ← (523)
29	12291.380	211	(12 0 12) ← (11 0 11)
30	12294.907	211	(817) ← (716)
31	12296.058	211	(735) ← (634)
32	12301.523	211	(928) ← (827)
33	12303.651	211	(744) ← (643)
34	12307.601	211	(10 1 9) ← (918)
35	12294.165	211	(13 1 13) ← (12 1 12)

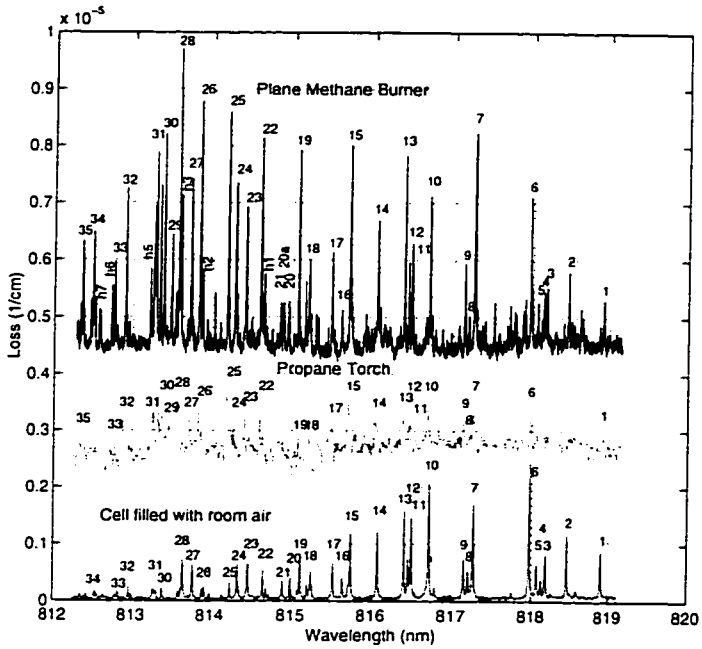

Figure 5.3: Spectra of water vapor in (a) a vacuum cell at 20 Torr and 300 K, (b) a propane torch flame at atmospheric pressure and 2000 K, and (c) a plane methane burner flame at atmospheric pressure and 5000 K.

from Boltzmann's distribution of rotational states $n(J, K_a, K_c)$ of water vapor [45]:

$$n(J, K_a, K_c, \nu_i) = n_{tot} \frac{g(J, K_a, K_c)}{Q(T)} \exp\left(-\frac{E(J, K_a, K_c, \nu_i)}{kT}\right) \tag{5.2}$$

where n_{tot} is the total number of states, ν_i characterizes the vibrational band state, (J, K_a, K_c) define the rotational state, $E(J, K_a, K_c, \nu_i)$ is the energy of the state, $Q(T)$ is the internal partition function [70], $g(J, K_a, K_c)$ is the degeneracy function, k is the Boltzmann constant, and T is the temperature. It is possible to relate the population of a rotational state to the integrated absorption measured via the line intensity I_s, [45] and the line strength $f(J, K_a, K_c)$,

$$I_s = \frac{\pi e^2}{m_e c^2} n(J, K_a, K_c, \nu_i) f(J, K_a, K_c), \tag{5.3}$$

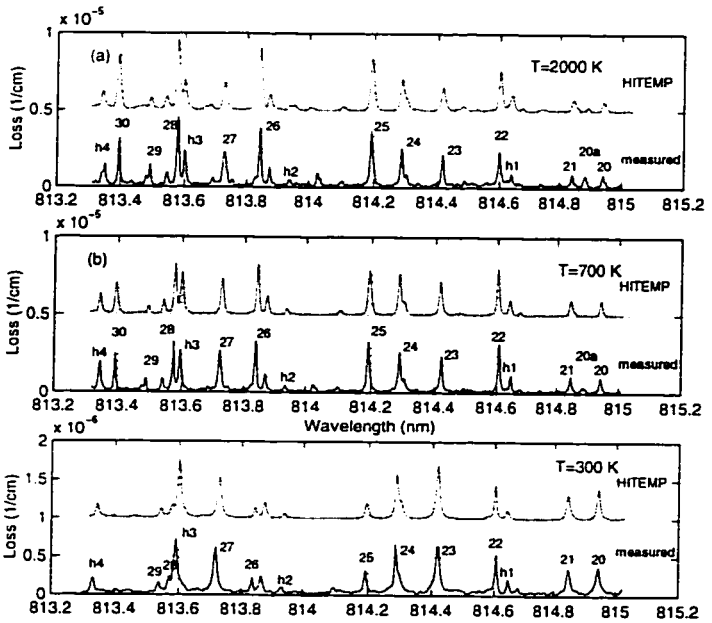

Figure 5.4: Spectra of water vapor generated by a plane methane burner at (a) 0.12 cm, (b) 3.1 cm ,and (c) 10.0 cm above the burner grid.

and to obtain a direct measure of the transition strength which is entirely independent of lineshape. Hence, by measuring the integrated absorption of various rotational branches within the $2\nu_1+\nu_2+\nu_3$ transition, namely the Q_{01} and R_{01} branches ($5 \leq J \leq 20$, $0 \leq K_a \leq 3$), and by fitting the slope of $\ln(I_s/g(J,K_a,K_c))$ versus $E(J,K_a,K_c)$, the rotational temperature was obtained. In this calculation, the degeneracy factors $g(J,K_a,K_c)$ were calculated from line intensities by using the lower state energy, the transition probability, and air-broadened linewidths, all provided by HITEMP, as well as an empirical temperature-dependent partitition function provided by Pierrot [70]. An iterative procedure that minimizes the least squares error of the fit and accounts for the temperature dependence of both line intensity and partition function, was used to determine the slope.

The final temperature at any given distance above the burner is an average over at least five temperatures obtained from different subbranches in which K_a is held constant and J and K_c are varied. Each subbranch contains at least 8 lines spanning at least 1.5 kT in lower state energy. The inset in figure 5.5 shows a typical straight

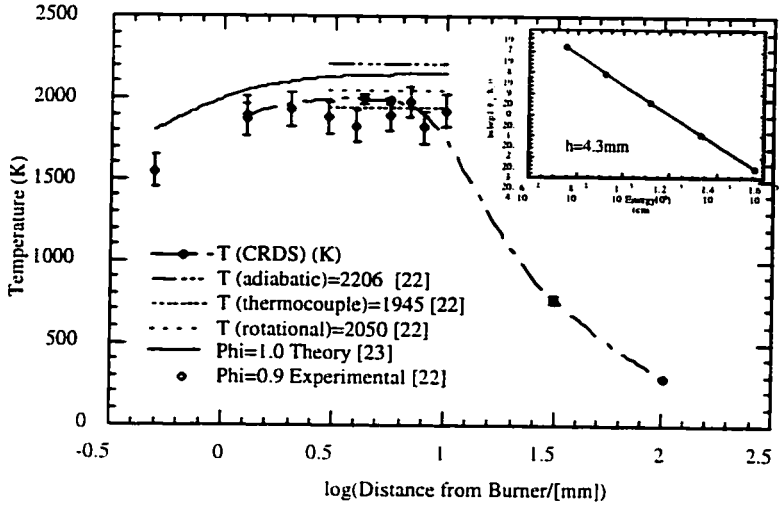

Figure 5.5: Water vapor temperature as a function of distance from a plane methane burner grid.

line fit for a rotational branch; the quality of the fit demonstrates that the assumption of local thermal equilibrium remains valid.

A plot of temperature versus distance for the flat flame methane-air burner is shown in figure 5.5, along with experimental results for ϕ=0.9 [12], theoretical results for ϕ=1.0 [103], and measured temperatures in the constant region for ϕ=1.1 [12]. From figure 5.5, it is clear that our measured temperature profile lies within the temperature interval for ϕ=1.1 given in Cattolica [12] for an identical methane-air burner, and is within 200 K of the adiabatic flame temperature. Furthermore, our temperature profile follows closely, although at slightly higher levels than expected for a fuel-rich stoichiometry, the temperature profile in Cattolica [12].

In order to extract the mole fraction of water vapor produced in the flame as a function of distance, recourse was made to the HITEMP database. Once knowledge of the temperature was obtained for a given point, it was possible to calculate the integrated line intensities from HITEMP for specific rotational lines[1]. The mole

[1]These integrated intensities can be converted from the standard HITEMP units of $cm^{-1}/(molecule/cm^2)$ to cm^{-2}/atm, by applying a factor of 2.48×10^{19} (at 273 K, and scaled according to the species temperature), so that partial pressures of water vapor can be directly calculated from the measured spectra.

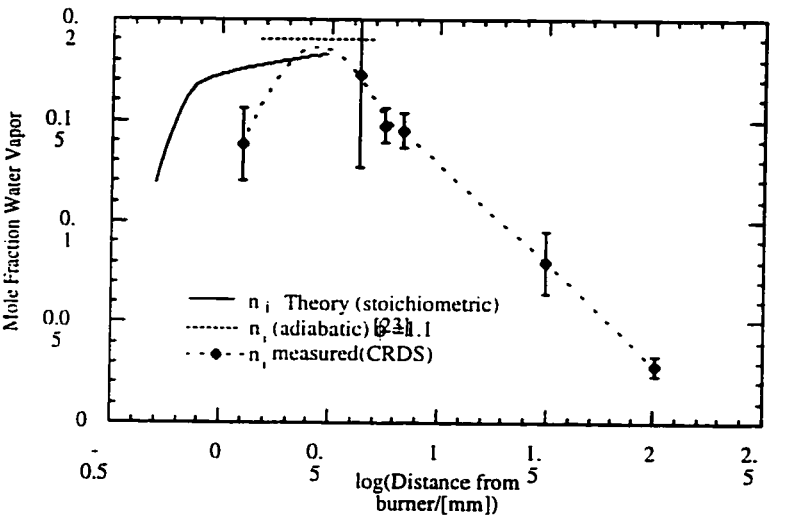

Figure 5.6: Water vapor mole fraction as a function of distance from a plane methane burner grid.

fraction, ψ, is then simply given by the ideal gas law for a fixed temperature and volume:

$$\psi_{H_2O} = \frac{n_{H_2O}}{n_{tot}} = \frac{p_{H_2O}}{p_{tot}} = p_{H_2O}(atm) \tag{5.4}$$

for a 1 atm flame, where n is the number of moles, and p is the pressure. A plot of mole fraction of water vapor versus distance from the burner surface is given in figure 5.6, along with the adiabatic peak mole fraction for ϕ=1.1, and a theoretically predicted distribution for ϕ=1.0 from Tsatsaronis [103]. The mole fractions plotted are an average over six rotational lines with $4 \leq J \leq 7$, $1 \leq K_a \leq 3$, and $2 \leq K_c \leq 6$ in the $2\nu_1 + \nu_2 + \nu_3$ vibrational band.

The measured data were interpolated, and this interpolation lies in between the theoretically predicted profile and the adiabatic limit, as would be expected for a fuel-rich ($\phi > 1.0$) stoichiometry. Because the majority of our data points lie outside the theoretical region of [103], their lower mole fraction can be attributed to the rapid diffusion of water vapor above the burner surface, which is amplified with distance, and directly corresponds to the lower temperatures observed. Moreover, the data points within the theoretically predicted region possess fairly substantial error bars, indicating that significant measurement uncertainty exists. Finally, the overall lower mole fractions measured could be caused by perturbation of the burner stoichiometry

and gas flow by the nitrogen purge (used to protect the high reflectors). Although the purge was not observed to cause flame instability, it nonetheless increases the total nitrogen present in the flame, and could therefore cool the flame.

A MDAL of 8×10^{-9} cm^{-1} for 99.99% mirrors was calculated from the RMS baseline noise in an evacuated cell, divided by the quantity $L/(1-R)$, where L is the cavity path length and R is the mirror reflectivity. In the spectra of figure 5.3, however, the baseline RMS noise is increased from that of the evacuated cell: by a factor of 1.6 for measurements of ambient air in the cell; by a factor of 4.5 for the flat flame methane-air burner; and, by a factor of 25.2 for the propane torch. In addition, the flame spectra show irregular undulations in the baselines, even after background substraction, which are greatest in the propane torch spectrum. The increase in baseline noise from an evacuated cell to one filled with ambient air is consistent with our previous results [66], and has been attributed to the presence of dust and other airborne particles or droplets in the environment. The change in baseline noise from the presence of flames is much larger, with the largest increase observed for an uncontrolled burn in the narrow propane jet. Because care was taken in the combustion experiments to prevent contamination of the mirrors by using a nitrogen purge, the increase in the flame baseline noise seems to originate in the flame medium itself. There are several possible causes for the significant increase in flame baseline noise which result in 'fast' fluctuations and 'slow' baseline drift.

Rapid baseline fluctuations may be caused by both the nonuniformity and the luminosity of the flame media. The laser beam can be scattered by combustion products such as soot, or be rerouted from its linear propagation by local variations in the refractive index of the flame. Because it is impossible to distinguish between these and simple absorptive losses in the ringdown cavity, and because these losses occur randomly over the light path (which is thousands of roundtrips of the cavity), they will contribute noise to the baseline. Furthermore, the luminous output of the flame will also contribute to the noise because stray photons will pass through the output CRD mirror (which is only highly reflecting for 30 nm in the infrared, but will pass visible and UV light) to the PMT, and produce noise on the ringdown decay waveform. This noise translates into an increased fitting error and consequently

baseline noise. A red filter was used in the experiment to reduce this stray output radiation.

Slow fluctuations of the baseline may be produced by long-term variations in flame properties along the light probe path. A single scan (10 nm) lasts 8 hours, during which it is likely that flame changes in temperature, size, or chemistry, all of which would affect the total absolute losses in the background. This reasoning is supported by the observation that these fluctuations were enhanced in the uncontrolled propane jet, while they remained significantly smaller for the Meker type burner flat flame. For the propane jet, there is little premixing of propane and air, the flame is tall but narrow, and consequently susceptible to air currents or local heating of the gases and the jet nozzle. On the other hand, the Meker type burner has a tightly regulated input gas flow, adequate gas mixing of a fixed ratio of nitrogen and air, and its flame front is short, so that it remains relatively unaffected by air currents. Overall, it remains clear that the increase in baseline noise for the Meker flat flame did not impede observing water vapor transitions with sufficient accuracy to make the derivation of rotational temperatures and water vapor mole fraction possible. In fact, CRDS has proven itself resilient to significant problems caused by harsh, luminous environments.

5.3 Summary

We have demonstrated that it is possible to use CRDS to study ground-state molecular species, in particular water vapor, in hostile environments such as atmospheric flames. From our spectra of overtone transitions of O–H vibrations between 810 nm and 820 nm, we were able to extract rotational temperature and water vapor mole fractions as function of distance from the burner surface, in a straightforward manner.

The study of controlled flames (e.g., a flat flame premixed methane-air burner) proved much easier than study of uncontrolled flames (e.g., propane jet), although spectra were achieved for both. Most importantly, CRDS remained relatively insensitive to the radiative output of the flames and nonuniformities in the flame media did not pose any significant problems to the propagation of ringdown optical signals.

Chapter 6

CRDS using a Frequency-Stabilized Laser Diode

CRDS is usually practiced by coupling a pulsed laser source into a high-finesse optical resonator (Fabry-Perot cavity) that encloses the sample of interest, and detecting the decay of light in the resonator. Under many conditions, the decay is exponential and a plot of the ring-down decay rate versus frequency gives the absorption spectrum. The ring-down decay rate is controlled by the resonator finesse, and changes wherever the sample absorbs. This approach is limited in spectral resolution by the laser linewidth ($>$ 100 MHz for pulsed sources) [34], in data acquisition rates by the pulse repetition rate of the laser (ca. 10-100 Hz), and in sensitivity by the inherent trade off between resonator finesse and light throughput.

Recently, efforts have been made to overcome these limitations of pulsed CRDS by the use of narrow linewidth ($<$ 10 MHz) CW lasers. Lehmann [47], Meijer [24] and Romanini [78] were the first to propose and implement the use of narrowband laser sources in CRDS. Lehmann [47] first proposed coupling a narrowband CW diode laser source to a ring-down cavity, in order to build up enough energy in the cavity to perform shot noise limited measurements. Meijer *et al.* [24] measured phase shifts (PS-CRDS) rather than intensity decay of an intensity-modulated CW light beam. They demonstrated for the first time that acquisition rates of kHz were compatible

with high-resolution CRDS, and that narrowband laser throughput could be improved by using stable resonators with a dense transverse mode structure. In an alternative approach, Romanini *et al.* [78] swept one resonant mode of the cavity through the CW laser linewidth (CW-CRDS), thereby allowing significant buildup of light inside the ring-down cavity, then switched off the light with an acousto-optic modulator and measured the intensity decay. Acquisition rates of several hundred Hz were thereby demonstrated, in addition to excellent light throughput, and reduced baseline noise leading to very high sensitivities. Romanini *et al.* [77] were also able to apply CW-CRDS to an external cavity diode laser (ECDL).

Recall that much of current ring-down spectroscopy [62, 57, 83, 120, 87, 117] still relies on fairly costly laser sources. As solid state lasers (e.g., Ti:Sapphire lasers, Nd: Yag-pumped OPOs, and ECDLs) have gained in reliability, tuning range, and output power, they have started to replace the more traditional tunable dye lasers, although they are no less expensive. Simultaneously, semiconductor laser diodes (LD) have also been improving in power, wavelength coverage, and reliability. The rapid growth of the communications industry in recent years has resulted in the availability of tunable near-infrared LDs at a rapidly diminishing cost (< \$500). In fact, owing to their compactness, low cost, durability, high wallplug efficiency, and compatibility with both fiber and silicon technologies, infrared laser diodes seem to be an ideal light source for realizing practical CRDS systems.

Early attempts demonstrated difficulties in applying LD sources to CRDS [47, 75]: whenever a LD beam is reflected directly back into the laser, as occurs in a linear cavity configuration, even under optical isolation, the optical feedback may result in phase fluctuations and mode hopping of the LD. In fact, at higher feedback levels, as would be typical for most practical setups, a wide variety of effects ranging from linewidth broadening to complete 'coherence collapse' (linewidth > 10 GHz) is often observed [56] and is illustrated in figure 6.1a. The inherent problem is the formation of 'external cavities' by reflective optics with the output facet (which has either a low reflectivity or is AR coated to increase output power) of the LD. The external cavity

affects both the gain and phase relations of the LD [69, 2, 14]. Thus, whenever back reflection is allowed, the lasing characteristics of the LD (frequency, number of excited modes, output power, etc.) become highly dependent on uncontrollable experimental parameters, most notably the external cavity length.

Several solutions exist to this coupling problem. A LD with an AR coated output facet can function as a gain medium in an external cavity (formed by a feedback element and a frequency selective element) that allows only one specific mode to exist, and that reduces (but does not completely eliminate) the sensitivity of the LD to feedback [77]; the feedback from a linear cavity configuration can be completely eliminated by using a ring resonator structure, as will be discussed elsewhere [64]; or, the external cavity effect can be controlled by placing an acousto-optic modulator (AOM) inside the external cavity, thereby stabilizing the time-averaged behavior of the LD. The last approach, first demonstrated by Martin *et al.* [56] as a useful scheme for stabilizing LDs in the presence of direct back reflections, and its application to CW-CRDS, is the primary focus of this chapter.

6.1 AOM Stabilization of Laser Diodes

In an AOM device, a pressure transducer creates a sound wave that modulates the index of refraction in an active nonlinear crystal, thereby producing a Bragg diffraction grating that disperses an incoming light beam into multiple orders [115]. By switching the RF power that drives the pressure transducer, light can be rapidly deflected by the AOM into and out of the first order, so that AOMs can be used as high-speed (< 10 ns rise/fall time) CW light modulators. The resulting diffracted beam is also frequency shifted by an amount equal to the acoustic wave frequency [115]. Hence, by placing an AOM into the external cavity formed by the LD back facet and the ring-down resonator input mirror, any light fed back from the first order becomes frequency shifted by twice the RF driver frequency. By considering the Lang and Kobayashi equations [46] that model the effects of optical feedback on LD behavior, it becomes clear that the frequency shift of the AOM forces the diode to cycle through

all values of phase with a period equal to the reciprocal of the frequency shift [56]. Therefore in order to achieve adequate stabilization, the AOM frequency must exceed the ring-down decay rate. Typically, a driver frequency greater than several MHz is sufficient for good quality ring-down reflectors (R > 99.99%), and will eliminate any changes in phase shift associated with changes in length of the external cavity. Under these conditions, the effective LD linewidth becomes insensitive to both thermal (seconds time scale) and mechanical (milliseconds time scale) perturbations of the external cavity length.

By placing an AOM between the laser diode and the input mirror of the ring-down cavity, the AOM can be used not only to switch the CW beam into and out off the first order diffraction, but simultaneously control LD linewidth. The AOM driving power determines the diffraction efficiency and hence the amount of feedback to the LD. The external cavity length fixes the maximum achievable linewidth for each feedback level (cf. figure 6.1b). The first order diffraction feedback drives the LD phase and stabilizes linewidth. Finally, the linewidth can be further enhanced by introducing nonfrequency-shifted feedback (of at least the same magnitude as first order feedback) that allows multiple external cavity modes to exist. The first order feedback then cyclically chirps the LD output through these modes at twice the AOM driver frequency (cf. figure 6.1c). In turn, the flexibility in achievable LD linewidth enables many different CRDS applications. Pressure broadened transitions, such as those of trace gases in the environment, can be studied using a broad LD linewidth (100 MHz to 1 GHz) with the advantage that the cavity throughput is increased with broader linewidth. Alternately, high resolution, Doppler-limited CRDS [78, 77], can be performed with a narrowed (1 MHz to 100 MHz) LD linewidth.

In this chapter, we focus on the demonstration of sensitive CRDS detection of water vapor using an AOM stabilized LD with both first and zeroth order feedback. The absorption spectra were extracted from a measurement of the intensity decay of light exiting the ring-down resonator. We note, however, that the sensitivities reported here should be regarded as prelimianary ones, as the primary sources of baseline noise are not presently completely understood. System performance will

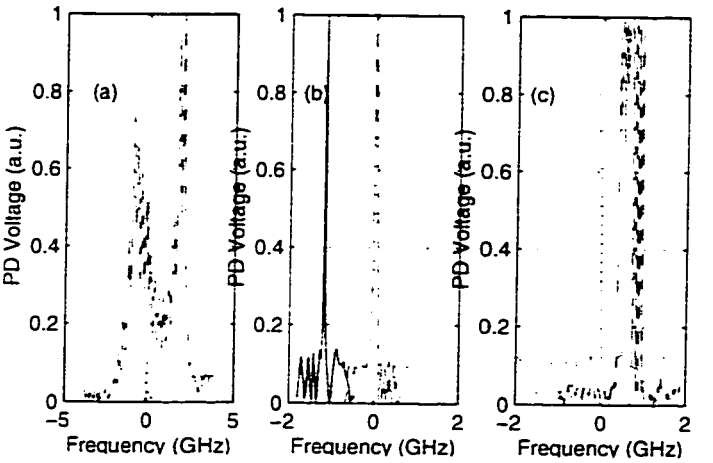

Figure 6.1: (a) Linewidth for a free-running LD (solid) and for a LD under feedback (36 dB feedback) from a ring-down cavity (dashed). (b) LD linewidth as a function of external cavity length for only first order feedback: L_{ext} = 215 cm (solid), L_{ext} = 100 cm (dashed), and L_{ext} = 55 cm (dash-dotted). The feedback level is 50 dB in all three cases. (c) LD linewidth for only first order (50 dB) feedback (solid) and both first (50 dB) and zeroth (50 dB) order feedback (dashed).

strongly depend on the application at hand. System optimization for several different applications, and a discussion of the trade offs involved in these different situations will appear elsewhere [65].

6.2 Apparatus and Experimental Method

The LD employed in these experiments was a Sharp LT017MD single-mode (V-channel current blocking) GaAlAs LD. The reflections of the facets are about 90% and 5%. Its threshold current is typically 60 mA when free-running. The LD was operated with both current and temperature stabilization (Peltier heater/cooler) provided by a laser diode controller (Melles Griot: 06DLD203 and 06DTC007). The free-running diode produces about 40 mW output power at 812 nm for 26°C and 100 mA operating current I_{op}. Wavelength scans were performed by current tuning the diode for small wavelength excursions (0.001 nm = 0.015 cm^{-1} at 810 nm with a 0.01 nm/mA rate) and temperature tuning for larger wavelength excursions (0.1 nm = 0.15 cm^{-1} at 810

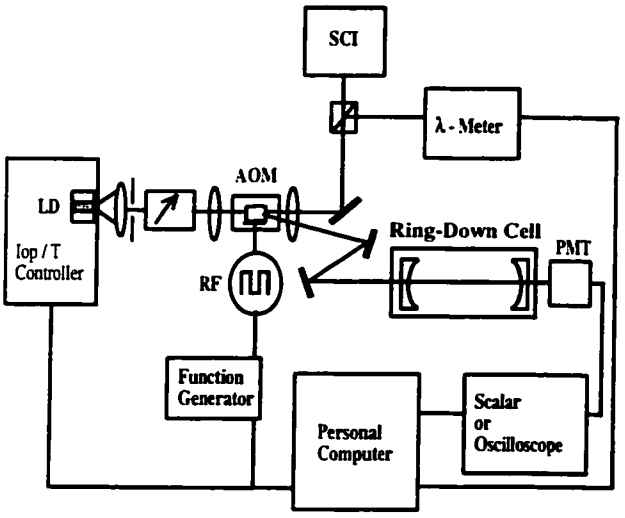

Figure 6.2: Laser diode cavity ring-down spectroscopy setup using acousto-optic modulator feedback stabilization.

nm with a 0.05 nm/°C rate). The LD output remained stable over 1.2 nm (812.6 - 813.8 nm), but only 0.6 nm (813.2 - 813.8 nm) were used for the spectroscopy of water vapor. The bandwidth of the free-running device was independently measured to be about 50 MHz.

The experimental setup is shown in figure 6.2. The components were mounted on a vibration-isolated movable optical table (Newport: VW Series Workstation), but otherwise no special precautions were taken against thermal motion of the optical elements, even of the ring-down resonator. The output of the laser is collimated with a NA=0.25 lens, and passes through a pinhole (used to selectively block back reflections into the laser and to protect it from back reflections from the isolator itself) and then through an optical isolator (OFR: IO-5-NIR-LP) before it reaches the AOM (Brimrose: GPM-400-100-960 with FFA-400-B2-F1 driver). The laser is focused to about 60 μm at the center of the AOM crystal and is recollimated after the AOM. The RF driver of AOM is modulated with a square wave output from a function generator (HP: 8116A). The zeroth order of the AOM passes into the diagnostics of the experiment, namely a fiber-coupled wavelength meter with 0.001 nm resolution (Advantest: TQ8325), and a scanning confocal interferometer (Burleigh: 8 GHz SA^{Plus} Analyzer

with RG-91 driver, DA-100 detector) whose back reflection can be used for zeroth order feedback (or blocked with a pinhole on slight detuning). The beamsplitter in the diagnostics achieves a 65/35 split with 65% of the light reaching the wavelength meter. The first order passes through optional beam shaping optics (beam expander and mode-matching lenses) before entering the ring-down resonator. The ring-down cavity is 45.7 cm in length, comprises two 1″ mirrors with 1 m radius and 99.97% reflectivity (Newport:10CV00.SR.40F), and is enclosed in a vacuum chamber with 2″ sapphire windows. Cavity adjustment is made via flexible bellows fixed in gimbal mounts (MDC: FGC-275-M). Such a stable rather than confocal optical cavity configuration, as first proposed by Meijer *et al.* [24], was chosen to provide a fairly dense mode structure that was found to increase output signal levels and reduce shot-to-shot fluctuations in cavity coupling and hence time constant.

Detection at the cavity output is performed with a photomultiplier tube (Hamamatsu: R2658P with SRS PS 325 high-voltage supply) and a photon-counting scalar (SRS: SR430). It should be noted, that the cavity output is attenuated with an ND = 2 filter in order to prevent overflow of the scalar's counting bins. Later, the attenuator was removed, and the output signal of the photomultiplier was directly digitized on an oscilloscope (HP: 54510A). The ring-down decay obtained from either the scalar or the scope is fitted on a personal computer using the Levenberg-Marquardt algorithm with the initial guess being provided by a linear least squares fit of the logarithm of the signal. This scheme, first proposed by Naus *et al.* [61], correctly fits exponential decays with a constant offset, as is typical for a photomultiplier output. This becomes especially important when a large dynamic range in ring-down constant is required, i.e., when both very weak and very strong lines are simultaneously present in a spectrum, or large fluctuations in concentration for a given species are being measured. Our effective data acquisition rate is presently limited to several hundred Hz by the oscilloscope and scalar response rates.

Cavity pressures are measured with both a baratron (MKS: PDR-D-1) and a convection gauge (Granville-Phillips: Model 275). Before any sample is introduced

for measurement, the cavity is purged below 1 mTorr using a mechanical pump with a liquid nitrogen trap. All background scans are also taken at this pressure. For low pressure measurements, a constant water vapor pressure is established in the cavity by adjusting both the cavity evacuation rate and the water vapor inflow rate. Stable flows ranging from 20 mTorr to 10 Torr in cavity pressure were thus established. When measuring water vapor in room air, the pump was removed, and the valve simply opened to let air into the cavity.

6.3 Results and Discussion

Using the AOM stabilization scheme for a laser diode source, shown in figure 6.2, we were able to perform CRDS on water vapor present in ambient air or in an evacuated optical cavity. LD linewidth control was performed with feedback from both first and zeroth orders, with levels of -48 dB and -47.6 dB, respectively (worst case), and -52 dB and -51.7 dB, respectively (best case), (the isolator has 36-40 dB isolation) for broad linewidth measurements. These feedback levels were estimated with the help of a beamsplitter placed immediately at the LD output. A total FWHM linewidth ranging from 500 MHz at lower tuning temperatures (30°C) to 240 MHz at higher tuning temperature (40°C) was observed, and is illustrated in figure 6.3. This laser linewidth assured that at least one longitudinal mode, and its associated transverse modes, were always excited in the ring-down resonator [24]. Similar observations can be made for low pressure scans made with narrower linewidths (180 to 240 MHz).

The decrease in linewidth, i.e., the number of excited external cavity modes, appears to indicate that the overall LD dynamics depend strongly on temperature (cf. figure 6.3). Changes in carrier density noise, index of refraction or carrier confinement, all of which affect the LD phase, appear to be fairly negligible for a 10°C temperature change and hence not directly responsible for this substantial linewidth change. Nonoptimal packaging and hence nonuniform LD heating could produce strain on the output facet, thereby changing its reflectivity, and hence the feedback coupling. More detailed investigations are necessary in order to determine the origin of this effect and

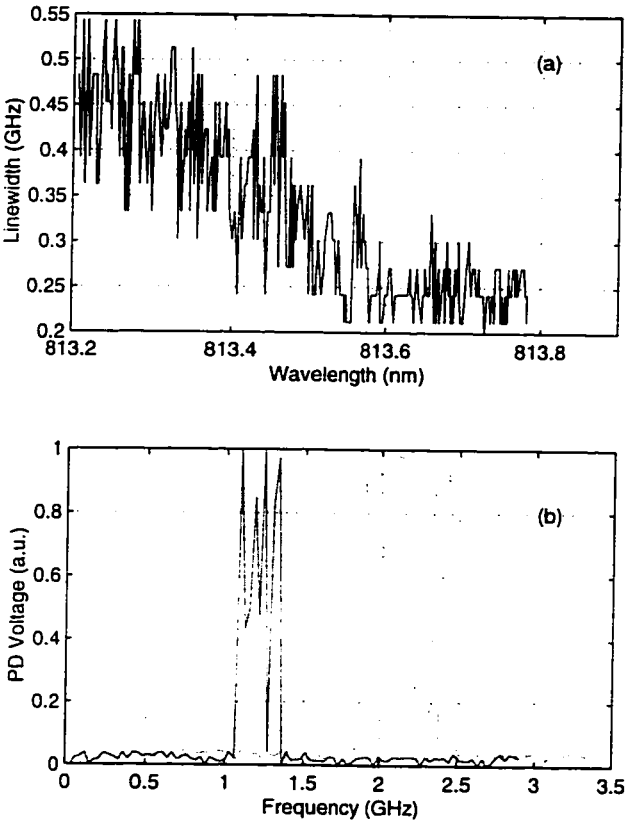

Figure 6.3: (a) LD linewidth as a function of wavelength (50 dB feedback), (b) LD spectral output at 813.2 nm (dashed) and 813.6 nm (solid).

to control it [65]. For small temperature excursions (ca. 2°C) and correspondingly small wavelength excursions (ca. 0.1 nm), however, the linewidth remained constant, as expected. Thus, for monitoring one or two lines of a given species, this stabilization scheme is more than adequate. Because minimization of baseline noise remains critical, a comparative study of the effects of using zeroth order feedback versus external cavity length to achieve broad linewidth LD output is necessary [65].

The cavity output decay train as seen on an oscilloscope is shown in figure 6.4a, while that recorded by the scalar for a single decay is shown in figure 6.4b. Figures 6.4a and 6.4b, show the actual averaged signals that were fitted to obtain the ring-down decay rates. Over a millisecond time interval, the stabilized LD is coupled into

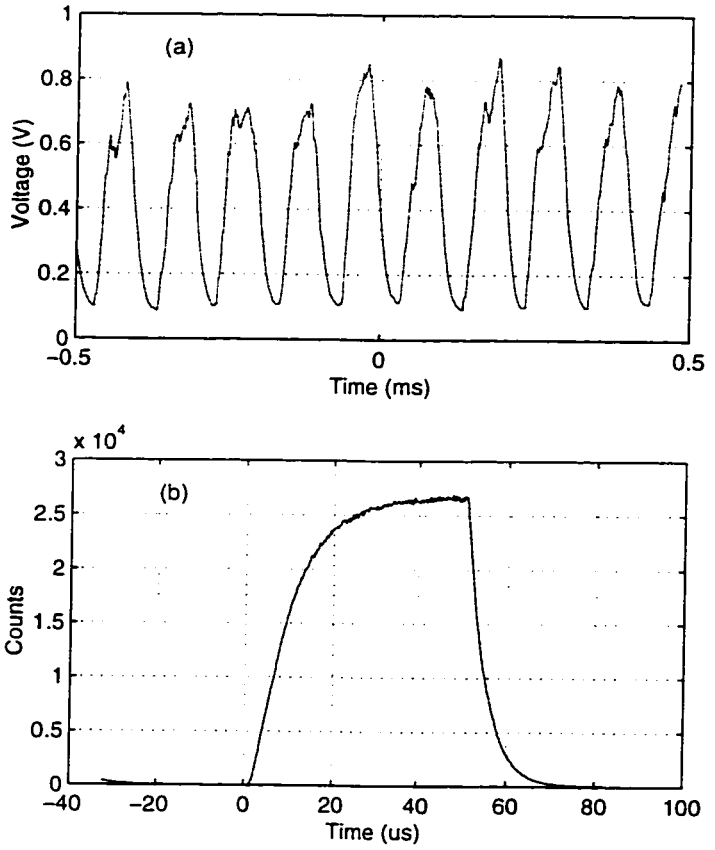

Figure 6.4: Ring-down waveforms showing cavity throughput as recorded on (a) an oscilloscope (300 shots averaged) and (b) a multichannel scalar (5000 shots averaged).

the unstabilized resonator every time that the AOM diffracts light into the first order, because our linewidth was much larger than that used by Meijer [24].

Effectively, the AOM modulation square wave at 10 kHz is convolved with the cavity response, producing an exponential signal build up ('ring-up') and an exponential decay ('ring-down') with equal time constants. For sufficiently fast sampling electronics, both ring-down and ring-up time constants could be measured, and time constant acquisition rates on the order of kHz (depending on the quality of the cavity mirrors) could be achieved. Of course, ring-up time constants have the possibility of additional laser noise, which seems to be the case in the present setup.

On closer inspection of the coupling, however, it was found that there was a variation (about 5%) in the intensity of the coupled light. This RMS variation corresponds to different numbers of cavity modes being excited by the input radiation. In fact, this cavity mode number variation was probably a major source of our baseline noise, which proved to be about 1% from shot to shot at a fixed wavelength in an evacuated environment, and about 4% from shot to shot in room air. By averaging over 300 shots on the oscilloscope and 5000 to 10,000 shots on the scalar, this variation could be significantly reduced. Signal levels for both scalar and scope detection remained high, so that actual noise in the waveform itself remained below 1%, allowing accurate numerical fitting.

Spectra of water vapor in room air and at 5 Torr are given in figure 6.5. Spectra were obtained in one continuous scan. Spectra at ambient pressure used maximum zeroth order feedback (47.6 dB) to achieve the largest possible linewidth (240 - 500 MHz) and cavity coupling. Spectra at low pressures ($<$ 100 Torr) used less zeroth order coupling (58 dB) to achieve a narrower laser linewidth (180 - 240 MHz) and to avoid convolution of the laser line with the absorbtion line [34]. Scan step size in both cases remained limited to 0.001 nm resolution by the current step resolution (0.1 mA) of the LD driver. No baseline adjustments have been made, but the overall baseline noise exceeds that reported by Romanini *et al.* [78, 77], and results from the excitation of multiple transverse modes in the cavity, which were used to improve light throughput. Our MDAL was 2×10^{-8} cm^{-1} for 99.985% reflectors. Its value is comparable to most pulsed CRDS studies [57, 120, 87, 117], and is presently limited by the quality of our mirrors.

Our spectra compare very favorably, in absolute frequency, linestrength and linewidth, to those generated by the HITRAN96 database [84]. HITRAN is an acronym for HIgh Resolution Transmission molecular AbsorptioN database (http://www.hitran.com). The peak located at 813.224 nm, which consistently appeared in our spectra, is not listed in HITRAN96, but can be found in table III of [101], where it is unassigned. The lines presented here belong to rotational transitions within the $2\nu_1 + \nu_2 + \nu_3$,

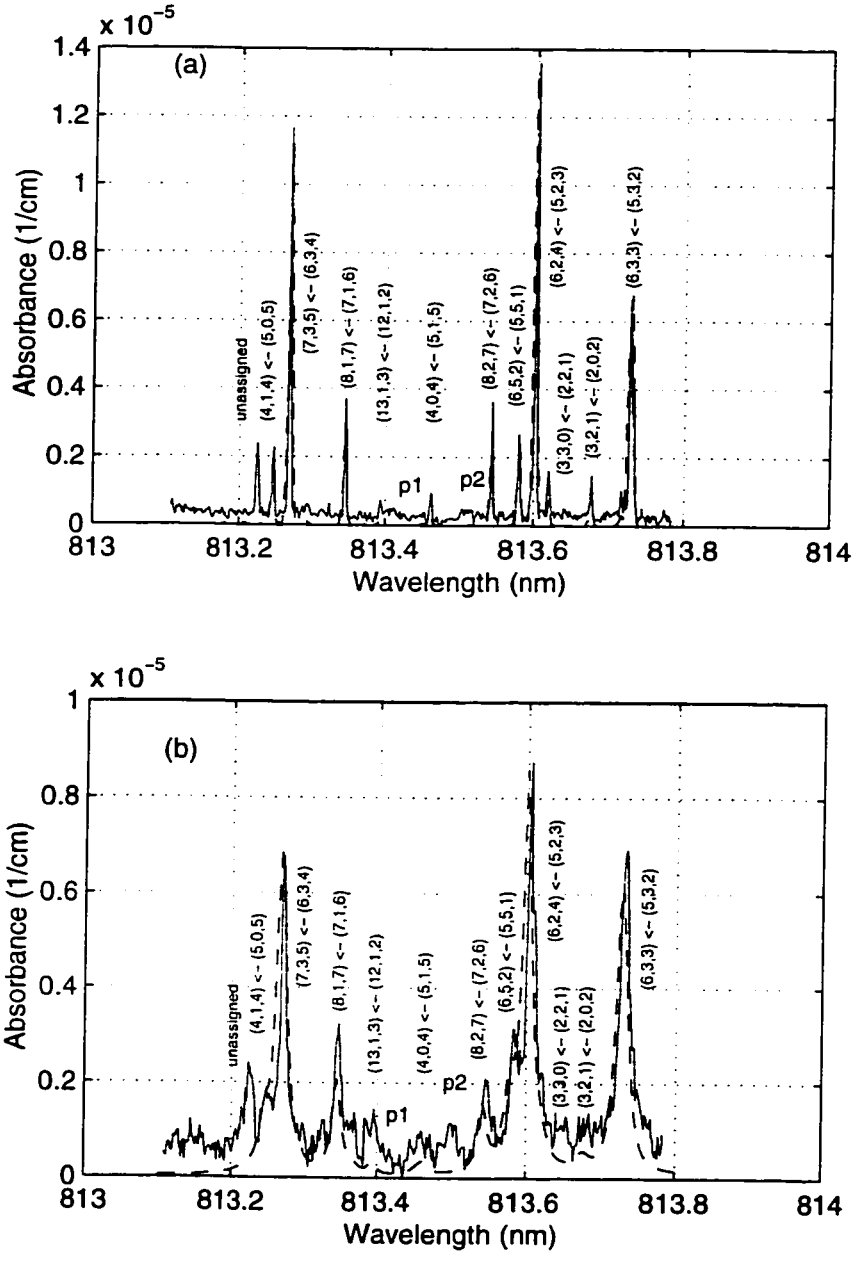

Figure 6.5: Spectrum of (a) water vapor in room air and (b) 5 Torr water vapor in a cell previously evacuated to below 1 mTorr. Spectra based on HITRAN96 are shown as dashed lines. Weakest lines occur at p1 (813.391 nm) and p2 (813.452 nm). Transitions are labeled as (J',K_a',K_c') $\leftarrow$ (J,K_a,K_c).

$3\nu_1 + \nu_2$ and $\nu_1 + \nu_2 + 2\nu_3$ vibrational bands. The weakest peaks recorded in HITRAN96 were measurable with our system. These peaks, located at 813.452 nm (p2 in figure 6.5) and 813.391 nm (p1 in figure 6.5) correspond to linestrengths of 6.33×10^{-26} cm^{-1}/(molecule/cm^2), and 3.40×10^{-26} cm^{-1}/(molecule/cm^2), respectively. The nominal sensitivity of this system to water vapor was 20 ppm in low pressure flows, and 200 ppm at 1 atm pressures.

For the 'open air' CRDS measurements, the baseline, noise, and overall sensitivity were significantly degraded from those of the evacuated cell (the time constant decreased from 10 μs to 6 μs). This degradation is most likely caused by the deposition of dust and other airborne particles or droplets existing in the environment, because it was reproducibly eliminated by evacuating the ring-down cell. Such contamination of the high reflectors that are fundamental to CRDS sensitivity may limit the ultimate sensitivity of trace species detection systems for the ambient environment.

6.4 Summary

We have demonstrated that it is possible not only to stabilize a free-running laser diode in the presence of strong reflections from a ring-down cavity, but also control the linewidth of the laser diode. It is also possible to stabilize the laser diode to only several MHz if high resolution is required. In our application, we are mainly interested in water vapor concentrations at near-atmospheric pressures. Consequently, we used linewidths on the order of a few hundred MHz, comparable to those of pulsed lasers. We have performed CW-CRDS with ring-down repetition rates of 10-50 kHz, and have achieved a MDAL of 2×10^{-8} cm^{-1}, comparable to pulsed CRDS.

The nominal sensitivity (20 ppm at low pressure, 200 ppm at 1 atm) of this system to water vapor can be improved not only by choosing a stronger absorption band of water at 1.3647 μm, but also by designing fast analog detection electronics, averaging over more waveforms, by obtaining better reflectors, and by adding some cavity tracking or feedback to allow mode matching and controlled mode coupling.

The sensitivity enhancement factor of each of these improvements is estimated at 1000, 5, 3, 10, and 10, respectively, leading to detection levels of sub ppb of water vapor under atmospheric conditions (and tens of ppt for low-pressure conditions). The realization of these detections limits in nonevacuated environments, however, will require that means be found to keep the reflectivity of the mirrors at a high constant value during operation of the instrument.

Chapter 7

Cavity-Locked Ring-Down Spectroscopy

The sensitivity limit of CRDS has been defined [83] as the ratio of experimental RMS noise in the ring-down decay, $\sigma_{\ln\tau}$, the decay lifetime, τ, and the effective path length, l_{eff}:

$$\sigma_\alpha = \frac{\sqrt{2}\sigma_{\ln\tau}}{l_{eff}\sqrt{N_p}} \tag{7.1}$$

where $l_{eff} = c\tau = \frac{l_{tot}}{L_{tot}}$, $\sigma_{\ln\tau} = \frac{\sigma\tau}{\tau}$, and N_p is the number of photons reaching the detector. Clearly, increasing the effective path length by increasing either the cavity length or mirror reflectivity, will only decrease σ_α if $\sigma_{\ln\tau}$ is preserved. This approach to increasing CRDS sensitivity is analogous to the use of White cells in simple absorption spectroscopy, and does not fully exploit the noise filtering properties of the optical resonator that are central to CRDS. The key to significant sensitivity improvement therefore lies in the reduction of $\sigma_{\ln\tau}$. Decay constant fluctuations depend on optical noise in the decay waveform (i. e. shot noise depending on $\sqrt{N_p}$), noise introduced by the detection electronics (e.g. amplifier noise, thermal noise in circuit resistance, or detector dark current), noise imposed by data acquisition system (e.g., digital oscilloscope quantization) used to acquire and fit decay waveforms [83], and variations in the experimental conditions (e.g., cavity pathlength changes or laser-cavity coupling). The smallest $\sigma_{\ln\tau}$ reported to date [83] is 0.0025 for a 1 second

integration time. Furthermore, it is clear that under ideal conditions (i.e. no detection or data processing noise), σ_α ultimately depends on the cavity throughput, leading the possibility of shot-noise-limited measurements.

Initially, efforts to use a CW laser in CRDS were directed at optically locking a LD to a high-finesse cavity [75]. This approach was precluded, however, by a lack of long-term stability (i. e. thermal drift) in locking the laser to the same cavity mode. Romanini et al. [78, 77] avoided this optical locking problem altogether by sweeping one resonant mode of their ring-down cavity through the CW laser linewidth. When sufficient buildup of light within the cavity was detected, the input laser beam was deflected with an acousto-optic modulator (AOM), and the cavity ring-down decay was recorded. Using this technique Romanini et al. achieved acquisition rates of several hundred Hz, with greatly reduced baseline noise, and extreme sensitivities. Nevertheless, Romanini et al. observed several limitations of this approach. In particular, the noise in the ring-down decay waveforms was far from shot-noise-limited: pulse-to-pulse variations in the ring-down decay were on the order of a few percent: baseline oscillations close to, but not equal to, the cavity free spectral range appeared and could not be systematically eliminated: and, back reflections from their linear CRD resonator strongly perturbed the external cavity diode laser (ECDL) performance, so that significant optical isolation (35 dB) was required.

In this chapter, an alternate CW-CRDS technique that employs two orthogonally polarized laser beams from a single ECDL is presented. One beam is used to lock continuously a high-finesse external cavity to the output of the ECDL, while the second beam is used to measure the ring-down time of the high-finesse cavity. Despite the greater complexity involved in locking a ring-down cavity (RDC) to an ECDL, there is a significant reduction of the shot-to-shot variation in the decay constant, elimination of baseline oscillations, and decreased optical feedback to the laser. In this contribution, both detection and locking systems involved are described, and their performance and limitations discussed.

7.1 Cavity-Locked CW-CRDS

Light possesses both a direction of propagation and a polarization of the electric field. This fact has recently been exploited by Meijer and co-workers [22] to perform polarization-dependent cavity ring-down spectroscopy on species exposed to magnetic fields. In the experiment described here, we also exploit the two mutually orthogonally components of linearly polarized light: p-polarized light (PPL) and s-polarized light (SPL). We define PPL to be light whose electric field vector lies in the plane of incidence of the RDC reflectors.

It is well-known from the physics of optical interfaces [21] that non-normal incidence of linearly polarized light on any dielectric interface will result in different responses for PPL and SPL. Thus, any optical ring resonator constructed with a geometry using non-normal incidence reflectors (e.g., an isosceles triangle) will actually consist of two nondegenerate Fabry-Perot cavities: a p-polarization cavity (PPC), and an s-polarization cavity (SPC). Moreover, non-normal incidence dielectric mirrors typically have a lower reflectivity for PPL than they do for SPL. Consequently, a ring resonator will consist of a reduced finesse PPC, and a higher finesse SPC. The ring resonator PPC and SPC transverse mode structure remains identical, because it is determined only by geometrical considerations. PPC and PSC free spectral ranges differ by the contribution of the derivative of the mirror phase shift [83], which was estimated to be a few tens of kHz. Moreover, the unequal phase shifts accrued during non-normal reflection of PPL and SPL will result in a fixed frequency difference between the PPC and SPC frequency responses.

Because orthogonal polarizations are easily separated with polarizing optics, the simultaneous use of PPL and SPL provides a straightforward solution for separating the cavity locking problem from the actual ring-down measurement. Constraints on locking the laser are relaxed by the use of the lower finesse PPC. Absolute wavelength accuracy at each point is determined by the PPC finesse and locking servo quality, rather than by laser linewidth or cavity mode sweep range. This improved frequency stability will enable very high resolution spectroscopy ($\ll$ 100 kHz) to be performed with these locked systems. Furthermore, ring cavities do not reflect light directly

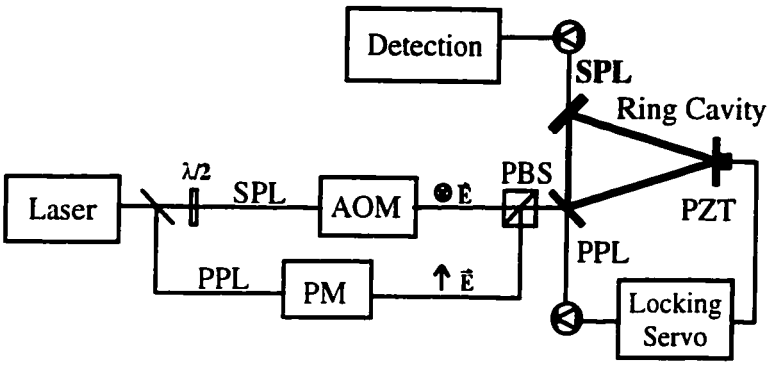

Figure 7.1: CW-CRDS setup using a ring resonator locked to an external cavity diode laser source.

back into the light source, so that optical feedback problems are greatly reduced.

In this experiment, the output of a CW laser is split into two arms (cf. figure 7.1): the PPL arm is used to lock the laser to a single mode of the lower finesse PPC of the ring resonator, while the SPL arm is switched on and off with an AOM to perform CRDS using the high finesse SPC of the ring resonator. The AOM also provides the appropriate frequency shift to the SPL, so that it can couple into the same transverse mode that is used to lock the PPC. Because frequency fluctuations in the laser source appear identically in both polarization arms, if the PPC mode is locked to the laser, then the SPL will consistently couple into the corresponding SPC mode. Both polarization arms can be identically mode matched to the cavity. The ring resonator presented in this paper is locked to an ECDL by means of the Pound-Drever-Hall technique [116]. The observed reduction of shot-to-shot fluctuations in the ring-down time constant, and improved baseline stability lend promise to this approach.

7.2 Experimental Setup

7.2.1 Ring Cavity CW-CRDS Optical Setup

The light source employed in this experiment is a commercial ECDL (New Focus: 6226-H032), tunable from 833.2 nm to 862.5 nm. Its output power varies from about

9 to 13 mW for a 60 mA drive current, over its entire tuning range. Although it is possible to electronically lock the ECDL to the RDC, it was found that the laser would not reliably tune as a single-mode device because of residual back reflections from optical elements normal to the beam path. This behavior was corrected by placing a 25-35 dB isolator (New Focus: 5568) at the output of the laser head. The half-wave plate of this isolator was adjusted to obtain PPL. A Faraday cage was constructed around the laser, controller, and connecting cable to shield the laser from stray EMI that causes instability in the laser's temperature controller.

The reflectors of the ring-down cavity [104] form an isosceles triangle with a long arm length of 19.5 cm and a base length of 2.0 cm. The plano/plano mirrors of the ring (CVI:TLM2-800-45S-1037) have 99.93% reflectivity for SPL at 833 nm, and 99.3% for PPL at 833 nm. The 1 m radius of curvature, concave/plano reflector (REO: run C628, 7.75 mm, 840-880 nm, 1 degree wedge) had a 99.95% reflectivity at 833 nm for both polarizations. The curved mirror is glued to a piezoelectric transducer so that the cavity length can be modulated over an entire free spectral range. CVI mirror absorption and scattering losses on the order of 400 ppm/pass were measured for the PPL and SPL, using a high-precision power meter to detect the reflected and transmitted power from the mirror at 45 degrees (i.e. for a 10 mW input at 830 nm, 9.993 mW were reflected, and 3 nW were transmitted). REO mirror absorption was quoted to not exceed 100 ppm for either polarization.

The silicon photodiode detectors are based on designs by Harb et al.[28]. The photodetectors used to detect the transmitted and reflected PPL locking signals are designed to maximize bandwidth (90 MHz) rather than gain, to render the locking sidebands with minimal distortion and noise. Shot-noise-limited sideband signals were readily attainable for optical powers of hundreds of microwatts in the p-arm. The SPL photodetector is maximized for gain rather than bandwidth (25 MHz), because SPL cavity output light levels are low (several microwatts), and ring-down decays exceed hundreds of nanoseconds (even for the strongest absorption lines).

The optical setup is shown in figure 7.2a. All components are mounted on a vibration-isolated optical table (Newport: VW Series Workstation). It was found that the quality and duration of the locking improved dramatically with optical mount

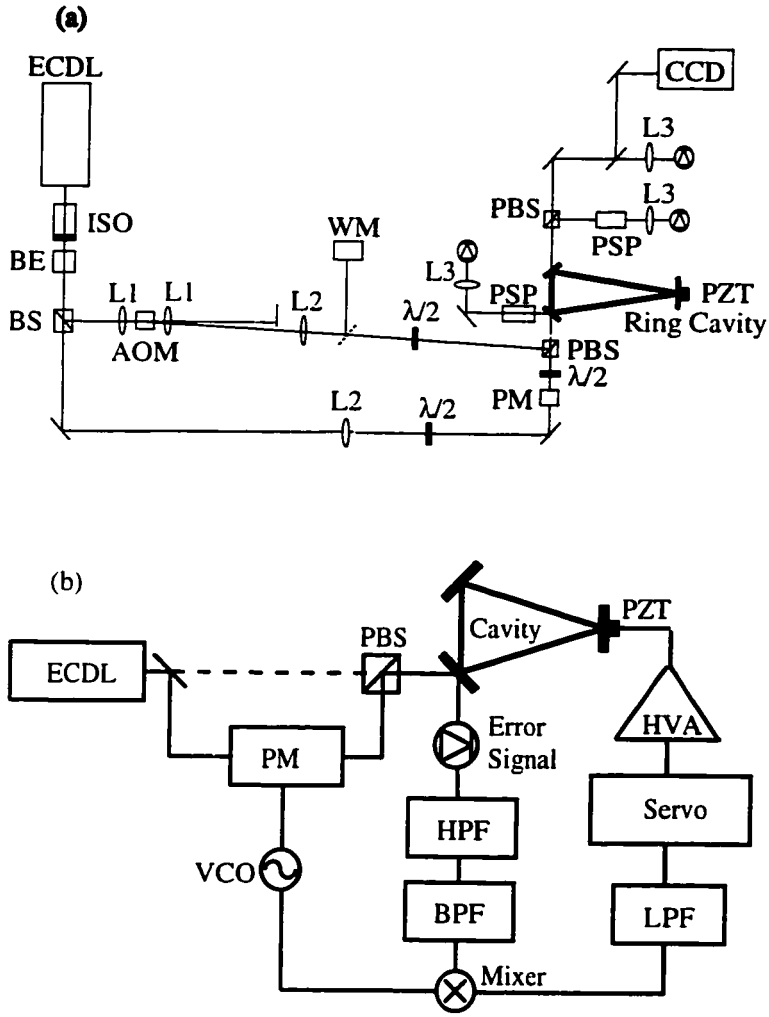

Figure 7.2: CW-CRDS experimental setup (a) optical system, and (b) cavity locking system. In (a) note the following abbreviations: AOM = acousto-optic modulator, BE=Beam Expander, BS= Beam Splitter, ISO = isolator, $\lambda/2$ = halfwave plate, L1= lens f=50 mm, L2 = lens f=1270 mm, L3 = lens f= 60 mm, PBS=polarizing beam splitter, PM = phaser modulator, PSP = polarization separation prism, WM = wavelength meter. In (B) note the follwing abbreviations: BPF = band-pass filter, HPF = high-pass filter, LPF = low-pass filter, PM=phase modulator, PZT = piezoelectric actuator, VCO = voltage controlled oscillator.

stability, and isolation from room air currents. The output beam of the laser isolator is first circularized before it is separated into two arms. One quarter of the light is used in the locking arm (PPL), while three quarters enter the detection arm (SPL). The locking PPL beam is mode matched to the TEM_{00} cavity mode with a 127 cm focal length lens, and travels through an electro-optic resonant phase modulator (PM, New Focus: 4001, 58.5 MHz), a polarizing cube beamsplitter and a 1.0 mm aperture, before entering the ring-down cavity. The PPL reflected from the cavity is used to lock the cavity to the laser, as described in the following section.

The detection beam is focused to a spot size of approximately 60 μm at the center of an AOM (Brimrose: GPM-400-100-960) crystal and recollimated using 5 cm focal length lenses. The AOM is driven by a voltage-controlled oscillator (VCO) with a frequency range of 300 to 535 MHz. The VCO RF output is modulated using a 50 kHz square wave from a function generator (SRS: DS345) and a RF switch. Thus, the AOM not only switches the SPL beam on and off, but also frequency shifts the SPL beam by the 320 MHz difference between SPC and PPC modes of the ring resonator. The first-order output passes through an aperture that blocks the zeroth order. A flipper mount may be used to direct the first-order beam into a fiber coupler for wavelength detection by a wavelength meter with 0.001 nm resolution (Advantest: TQ8325). The beam then passes through a 127 cm focal length lens for mode matching (identical to the PPL), and through a half-wave plate to convert it to SPL. It is reflected by a polarizing cube beamsplitter through an aperture before it enters the ring-down cavity.

Approximately 90% of the laser carrier light is coupled into the TEM_{00} mode of the cavity for PPL, and 85% for SPL. In both arms, the remaining light consists mainly of the TEM_{01} mode (9%) with less than 1% of the total light in the TEM_{10}, TEM_{02}, and TEM_{11} modes. The spatial coupling efficiency remained unchanged over several days. Moreover, the coupling efficiency was constant for 0.3 nm of continuous tuning of the laser wavelength. A scan of the cavity frequency response is given in figure 7.3a where it can be seen that the SPC resonance frequencies are shifted by 282 MHz relative to the PPC, and that most of the laser light in both arms couples into the TEM_{00} cavity mode. We note that when the cavity modes overlap an absorption line

of water, the total amount of dispersion between SPL and PPL changes by several tens of kHz, requiring that the SPL frequency offset be adjusted by changing the VCO frequency driving the AOM.

PPL and SPL exiting the ring-down cavity are resolved using a polarizing cube beamsplitter. PPL is further divided by a 10/90 beamsplitter with 10% going to a CCD camera to visualize the transverse mode either on a TV screen or using laser beam diagnostics software (Coherent: BeamView^{TM}), and 90% going to the transmitted p-arm detector. Cavity modes recorded on a CCD are given in figure 7.3b. For the TEM_{00} mode, a beam waist of 341 μm was measured, which is only slightly larger than the expected 328 μm TEM_{00} eigenmode waist of the ring resonator.

SPL passed through a Glan-Thomson prism to isolate the detection arm photodetector from PPL. The ring-down decay waveform issued by this detector was first amplified with a low-noise, high-speed amplifier (Stanford Research Systems: SR445) before digitization on a 10-bit, 1 GHz oscilloscope (Tektronix: 11402). The decay waveform obtained on the scope was fitted with a personal computer using the Levenberg-Marquardt algorithm with the initial guess being provided by a linear least squares fit of the logarithm of the signal, as first proposed by Naus et al. [61]. Our effective data acquisition rate is presently limited to several hundred Hz by data transfer rates between the oscilloscope and personal computer. The oscilloscope itself can acquire and average waveforms at kHz rates.

All spectral scans were performed in room air, at atmospheric pressure and with a water vapor partial pressure of 12 torr. After assembly, the ring-down cell's only aperture was sealed to prevent dust and particulates from entering the cavity (the only other inlet into the cavity are oversized holes in the piezo mount for electrical wires to the transducer). To obtain spectra, the ECDL was scanned by varying the piezoelectric voltage for fine frequency (0.001 nm) adjustments and the grating position for larger frequency adjustments (0.01 nm).

7.2.2 Locking using the Pound-Drever-Hall Technique

The laser and cavity were locked with a technique devised by Drever, Hall and co-workers[116], which generates an 'error signal' proportional to the difference between the laser and the cavity line centers. In the experimental setup, shown in figure 7.2b, the optical phase modulator was driven by a VCO set to 58.5 MHz. The optical signal reflected from the ring-down cavity passed through a Glan-Taylor prism, so that only PPL arrived at the photodetector. The photodetector electrical output passed through a high-pass filter and 60 MHz band-pass filters before entering a mixer where it was heterodyned with the 58.5 MHz VCO output. The phase shift between the RF and the photodetector output was optimized by adjusting BNC cable length. The mixer output passed through a low pass filter to generate the Pound-Drever-Hall error signal.

The error signal was then processed by a feedback servo circuit consisting of a PI controller and a high voltage amplifier. The piezoelectric transducer exhibited a resonance at 52 kHz which was eliminated by a twin-T passive notch filter at 52 kHz center frequency, having 48 dB maximum attenuation, and a 3dB bandwidth of 2 kHz. The notch filter dramatically improved the feedback loop stability and sensitivity to external perturbations, such as acoustic noise. The complete servo circuit (including the notch filter) had a DC gain of 60 dB, and a 3dB frequency of 455 Hz. The processed error signal from the servo directly controlled the piezoelectric actuator and hence cavity length. Thus, the servo closed the loop for locking the ring-down resonator to the laser.

To lock the cavity to the laser, a manual offset on the high-voltage piezo driver was scanned until the cavity TEM_{00} mode frequency would enter the locking range of the servo loop. The cavity would then remain continuously locked to the laser for up to 10 minutes (typically 5 minutes), before outside mechanical or acoustic vibrations produced a system excursion beyond the servo range. Long-term laser-frequency drift was easily compensated with the manual offset voltage on the high-voltage amplifier, which was also used to bring the system within the locking range after larger laser wavelength changes ($\rangle$ 30 MHz) during spectral scans.

The locked system response was monitored using either the error signal and/or the

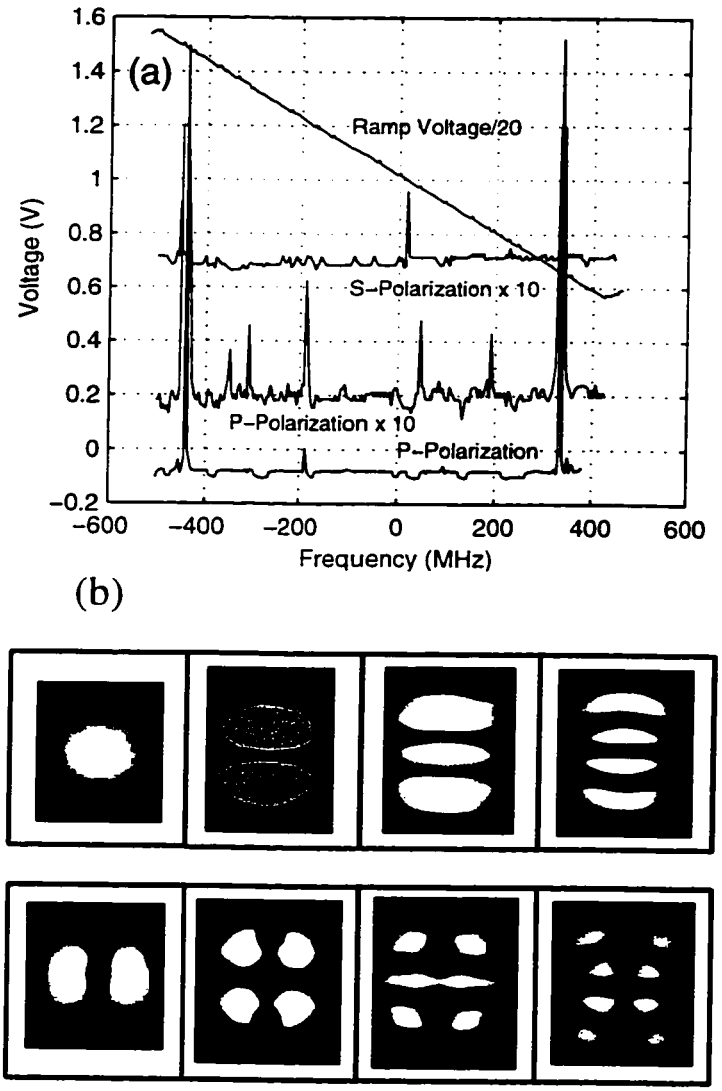

Figure 7.3: (a) Frequency response of the mode cleaner cavity design obtained by sweeping the cavity length through one free spectral range, and (b) CCD images of transverse modes for unoptimized cavity allignment.

transmitted p-arm signal: when the system was locked, these signals were recorded on a signal analyzer, to determine their fluctuations. By using the discriminator slope of the error signal, which converts voltage to optical frequency, fluctuations in the error signal were converted into residual differences between the laser frequency and the cavity resonance frequency. A plot of the frequency fluctuation spectral density is given in figure 7.4 which shows the reduction in laser noise produced by servo locking at lower frequencies. The total jitter between laser and cavity resonances was 1.1 MHz, slightly less than the free-running laser linewidth. Laser and cavity overlap was guaranteed by the servo for the 'average' laser lineshape, i.e. the cavity line was locked to the center of the 'average' laser lineshape. A much faster and complex feedback servo would have been required to dynamically lock the cavity to the laser. The effective laser and cavity linewidth difference accounted for the significant reduction in SPL throughput. Overall, SPL suffered modematching losses of 70%, a linewidth ratio loss of 86%, and mirror absorption/scattering losses on the order of 850 ppm per pass over 3100 passes, while PPL suffered respective losses of 40%, 30%, and 850 ppm per pass over 300 passes. Thus for a 900 μW SPL input, 2.3 μW were expected at the output, and 1.9 μW were measured. Similarly, 1.0 mW of PPL was injected, 325 μW of output were expected, and 315 μW were actually obtained.

Shot-to-shot fluctuations of about 4% in the fitted decay waveform intensities at each wavelength indicated that laser-cavity coupling was sufficiently reproducible to perform CRDS. Thus, the servo adequately ensured that laser light coupled only into the TEM_{00} mode of the cavity, and that coupling occurred for every trigger of the AOM. Therefore, the maximum potential data acquisition rate was 50 kHz, the AOM on/off modulation rate. As mentioned above, our actual data acquisition rate remained limited by detection electronics to only several hundred Hz.

7.3 Results and Discussion

Using the locked cavity stabilization scheme described above, we were able to obtain a spectrum of water vapor present in the ambient air. Figure 7.5a shows two-shot and

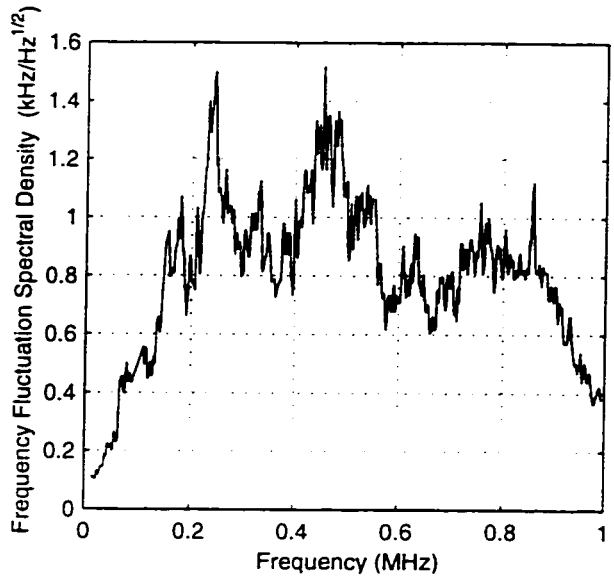

Figure 7.4: Spectral Density of laser-cavity frequency fluctuation response for a locked system.

averaged SPL ring-down waveforms. Figure 7.5b presents the residual obtained after fitting an exponential decay to the averaged waveform. Single-shot decays exhibited high frequency intensity noise whose phase was random with respect to the AOM (and oscilloscope) triggering signal. Hence, this noise was reduced to less than 0.05% of the decay waveform intensity by averaging 64 or more decay waveforms. Typically, 256 shots were averaged using the digital oscilloscope to obtain an averaged decay waveform (ADW), and to ensure that the only noise remaining on the ADW was scope quantization noise. Possible sources for this high frequency noise include amplifier noise and pickup, high-voltage amplifier and servo loop noise, as well as imperfectly compensated piezoelectric transducer electrical and mechanical resonances.

Although averaging greatly reduced the amplitude of high frequency residuals in the decay waveform, it enhanced a low frequency, quasi-sinusoidal residual (seen in figure 7.5b) whose phase remained fixed with respect to the triggering signal. It was found that the amplitude and period of this residual depended only on the intensity and period of the triggering signal. In fact, this residual could be reproduced exactly

by fitting artificially generated (low-pass filter on a square wave output of a function generator) decay waveforms to an exponential decay, as shown in figure 7.5c. Thus, it was finally determined that this regular residual was caused by input channel cross-talk within the digital oscilloscope. During subsequent data analysis, this reproducible residual was subtracted from the averaged ring-down decay waveforms prior to exponential decay fitting.

The dependence of $\sigma_{\ln \tau}$ on the number of shots averaged, N, is given in figure 7.5d, and shows a clear $\sqrt{N}$ dependence up to 64 shots. When more than 64 shots were averaged, the overall noise on the decay waveform could not be further reduced, and was observed to be limited by digitization noise imposed by the oscilloscope. Single shot $\sigma_{\ln \tau}$ was less than 4×10^{-3} and could be reduced to less than 5×10^{-4} for 64 shot ADWs which is comparable to recent results by Romanini et al. [76]. It should be noted that $\sigma_{\ln \tau}$ for a given series of shots never exceeded the fit uncertainty in each shot by more than 5%. However, to guarantee that all waveforms were indeed digitization limited, 256 shot ADWs were used, even though they did not result in any sensitivity gain over 64 shot ADWs. Ten ADWs were then recorded at each wavelength. Each spectral element was taken to be an average of 7 to 10 ADW ring-down decay constants, because ADWs that showed a significant decrease in intensity when the apparatus was perturbed by external vibrations during the experiment were discarded. The $\sigma_{\ln \tau}$ of averaged decay constants was 2×10^{-4}. The noise producing these variations in the ADW decay constant was primarily excess technical noise in the detection electronics and not oscilloscope quantization noise, so that under true shot-noise-limited detection conditions, these decay constant variations could be futher reduced.

Figure 7.6 shows an absorption spectrum of water vapor present in ambient room air. The resolution of the reported spectrum is 0.002 nm, except about the absorption peaks where resolution was increased to 0.001 nm. Ten ADWs were recorded at each wavelength. Each spectral element represents an average of 7 to 10 ADW ring-down The MDAL of 5×10^{-9} cm^{-1} in our spectra is comparable to that initially reported by Romanini *et al.* [78], and is comparable to most pulsed CRDS studies [62, 87, 57, 83]. It exceeds, however, the baseline noise reported by Romanini et al. [77] for the same

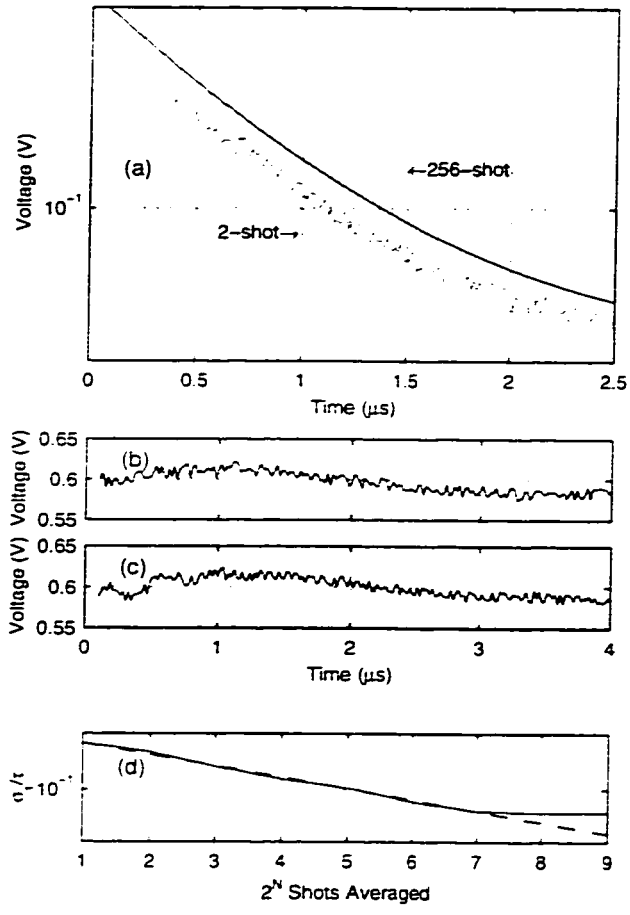

Figure 7.5: (a) Ring-down decays recorded on an oscilloscope with 2 shots and 256 shots. (b) residual from an exponential fit of a 256-shot waveform (magnified 100 times). (c) residual from a simulated exponential decay of a low-pass filter (magnified 100 times). and (d) dependence of $\sigma_{\ln \tau}$ on the number of shots averaged (measured =solid line. predicted = dashed line).

model ECDL by a factor of 25 because not only was our cavity half the length of that used by Romanini et al., but our mirrors had only a 99.93% reflectivity compared to the 99.999% reflectivity used by Romanini et al., i. e. our empty cavity losses were 70 times larger.

By locking the RDC to the laser source, the shot-to-shot fluctuations in decay constant were reduced by a factor of almost 100 compared to a free-running, multi-mode laser diode system [66]. Shot-noise limited detection was precluded by the quality of our detectors, by the laser linewidth, and by the limited SPC throughput. This illustrates, in fact, the trade off involved when mirror reflectivity is used to enhance sensitivity. While higher mirror reflectivity increases the empty cavity decay constant, thereby making detection of relative changes in the decay constant easier (slower detector and electronics can be used), the resulting decrease in the intensity of the detected signal limits the signal-to-noise ratio on the output decay waveforms. The increased noise on the decay waveforms leads to greater uncertainty in the fitted exponential, and hence greater uncertainty in the decay constant, which decreases sensitivity. Perhaps the use of a very narrow linewidth laser such as a CW Nd:YAG laser would allow very sensitive, shot-noise-limited measurements to be made, owing to their extremely narrow linewidths ($\langle$ 100 Hz).

Our spectra compare very favorably, in absolute frequency, linestrength, and linewidth, to those generated by the HITRAN96 database [84] (http://www.hitran.com). The lines presented here belong to rotation transitions within the $3\nu_1+\nu_2$, $2\nu_1+\nu_2+\nu_3$, and $\nu_1+3\nu_2+\nu_3$ vibrational overtone bands [101]. The weakest peaks, recorded in HITRAN96, that are measurable with our system, are located at 833.674 nm and 833.206 nm, and correspond to linestrengths of, 4.126 $\times 10^{-26}$ $cm^{-1}/(molecule/cm^2)$ and 1.259 $\times 10^{-26}$ $cm^{-1}/(molecule/cm^2)$, respectively. These are somewhat weaker than previously reported water lines recorded with a 45.7 cm long linear cavity mirrors having with R=99.97% [66]. The nominal sensitivity of this system to water vapor is 5 ppm at 1 atm pressure.

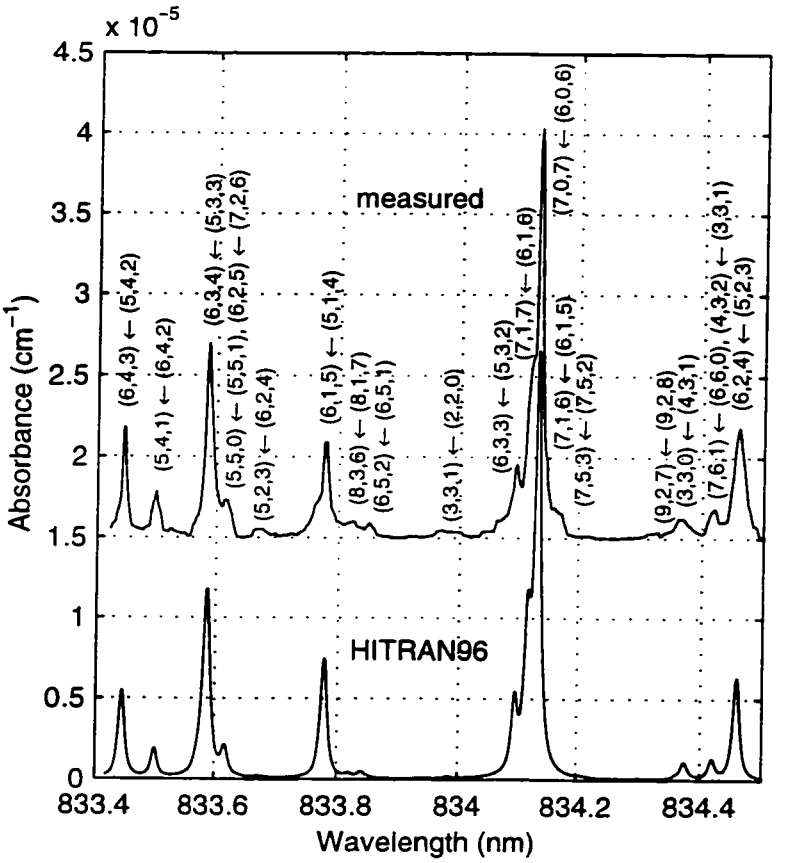

Figure 7.6: Spectrum of water vapor in room air obtained using a ECDL locked to the ring-down cavity. Spectrum based on HITRAN96 is shown in dashed lines. Weakest lines occur at 833.206 nm and 833.674 nm. Transitions are labeled as (J',K'_a, K'_c)← (J,K_a,K_c).

7.4 Summary

It is possible to use a single-beam, dual-arm approach to CRDS to continuously lock a narrow-band external-cavity diode laser to a high-finesse resonator with one arm, while performing CRDS on the locked system using a second, orthogonally-polarized arm. By using a ring resonator as the cavity ring-down cell, the two orthogonal polarizations see different mirror reflectivities at non- normal incidence and, therefore, a single resonator can be simultaneously used as a low- finesse resonator for laser locking, and as a high-finesse resonator for CRDS. By frequency-shifting one arm of a split laser beam with an acousto-optic modulator and then rotating its polarization, the two arms of the laser beam (one s- and the other p-polarized with respect to the ring-down cavity mirrors) can become simultaneously resonant in the cavity. In this manner, the cavity may remain continuously locked to the laser output, ensuring that both arms will couple efficiently into a single mode of the cavity, while the light in one polarization is switched on and off to perform decay time measurements. Presently, this measurement technique remains limited by cavity throughput, so that determination of the ring-down decay constant is limited by technical noise in the photodetectors.

CW-CRDS using such a cavity-locked system achieving ring-down repetition rates of 50 kHz, and a MDAL on the order of 10^{-9} cm^{-1} was performed. Combination overtone spectra of water vapor in the ambient environment between 833.4 and 834.5 nm, with nominal sensitivities of 5 ppm at 1 atm were obtained. This sensitivity can be dramatically improved by choosing a stronger absorption band of water vapor (such as 1.3647 μm), a narrower linewidth laser source (e.g., a CW IR- OPO) and allowing the use of better reflectors and better designed photodetectors. The realization of these improvements, leading to shot-noise-limited measurements with estimated noise levels of 10^{-12} cm^{-1} to even 10^{-13} cm^{-1} and spectral resolution on the order of a hundred Hz, may make CRDS one of the most sensitive, high-resolution spectroscopic tools.

Chapter 8

Optical Heterodyne Detection in CRDS

In all existing CW-CRDS systems, the light leaking out of the RDC is generally detected with a photosensitive device – a photodiode or a photomultiplier tube – which produces an electrical current proportional to the instantaneous flux of photons. In any ring-down experiment, the light level exiting the cavity decays to zero. Therefore, the detected electrical current level will continuously decrease while other electrical noise sources do not, and eventually obscure the desired signal. Because CRDS sensitivity depends directly on the ability to fit an exponential decay to measure the decay constant, and noise introduced on the detected waveform degrades the fit accuracy, any electrical noise in the detection system results in reduced sensitivity. Previous efforts to improve ring-down sensitivity primarily focused on increasing the RDC throughput and lengthening the decay constant. Little effort was made to reduce detection system noise.

Optical heterodyne detection is a method that is well-known in optical communications (cf. figure 8.1a): the desired signal amplitude, $\vec{E}_S$, is made to interfere on the surface of a photodetector with another (stronger) wave, called the local oscillator (LO), $\vec{E}_{LO}$. When the LO and signal frequencies differ by $\delta\nu$, the total detector current, I_D, which is proportional to the square of the total field amplitude, has a

term combining the signal and LO that oscillates at $\delta\nu$:

$$\begin{aligned} I_D &\propto \|\vec{E}_S + \exp(-i(2\pi\delta\nu t + \Phi))\vec{E}_{LO}\|^2 \\ &= \|\vec{E}_S\|^2 + \|\vec{E}_{LO}\|^2 + 2Re[\exp(-i(2\pi\delta\nu t + \Phi))\vec{E}^*_{LO} \cdot \vec{E}_S] \\ &\propto I_S + I_{LO} + \|I_{H0}\| \cos(2\pi\delta\nu t + \Phi) \end{aligned} \tag{8.1}$$

where the three terms on the bottom line are individually proportional to the corresponding terms above them. The heterodyne current from I_D is the last term, $I_H(t) = \|I_{H0}\cos(2\pi\delta\nu t + \Psi) \propto 2Re[e^{-i(2\pi\delta\nu t+\Psi)}\vec{E}^*_{LO} \cdot \vec{E}_S]$, where Ψ is a random phase term that depends on the difference between the local oscillator and the signal optical path lengths, as well as any transient behavior at the turn off time of $\vec{E}_S$. This heterodyne current can be obtained with simple analog or digital electronics (that also reject any DC signal, which leads to additional noise elimination). Because the heterodyne signal is linear in the LO and signal amplitudes, a strong LO signal can render the I_D much larger that is direct-detection on counterpart I_S. Moreover, if the LO signal is large enough, then I_D can exceed the technical noise of the detection system, and the dominant noise on the demodulated signal will simply be noise inherent to this signal itself (e.g. shot noise of the detected light).

The basic idea of optical heterodyne detection for ring-down was proposed by Levenson *et al.* [52], and is illustrated in figure 8.1a. A laser produces both the radiation which enters the RDC and can be extinguished by means of a modulator to produce I_S, and the radiation which constitutes the LO. The LO and RDC output are combined by means of a beamsplitter, and are directed onto a photodetector. It should be noted that both decay signal and LO electric fields must overlap exactly on the photodetector (to avoid extraneous beating), and that they must have identical polarizations to produce the necessary interference.

Two detectors can also be used after the beamsplitter, and their electrical signals differenced (cf. figure 8.1b). If the beamsplitter divides the LO and signal beams equally, then the heterodyne signals reaching each detector are equal, but opposite in sign, because beamsplitters posses the unitarity property. The difference current will therefore equal $2I_H(t)$. The difference current can once again be demodulated to yield the desired decay signal with standard electronic schemes. An important advantage

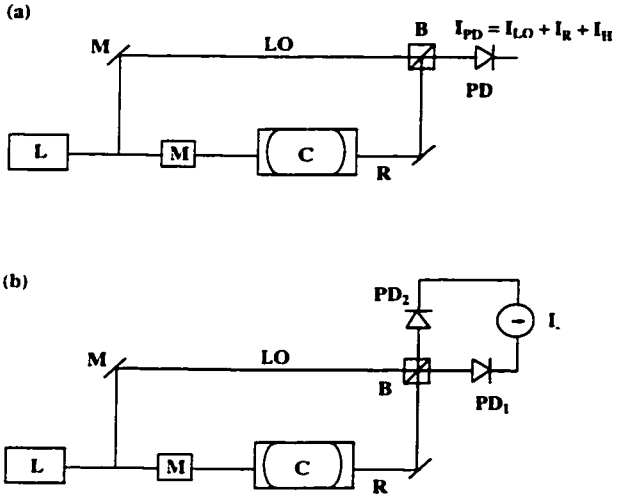

Figure 8.1: CRDS setup using (a) single detector or (b) dual differential heterodyne detection for RDC output signals.

of the differential heterodyne detection method is that variations in the LO amplitude (i.e. noise) are rejected as common mode noise. However, the differential detection requires that the two photodetectors be matched in their response, gain, and technical noise floor, otherwise this scheme will yield results no better than those obtained using the worse detector of the pair.

8.1 Experimental Setup

Overlapping the LO and ring-down signal electric fields in a linear RDC setup could prove difficult. However, in the locked CW-CRDS setup described in the previous chapter and shown in figure 8.2, the two orthogonal polarizations of light [p-polarized (PPL) and s-polarized (SPL)] exit the same RDC and exist in the same TEM_{00} modes, so that spatial overlap of the LO and signal is automatic. In this case, the TEM_{00} mode frequency difference (used by the AOM to shift the SPL) was measured to 282.7 MHz when SPL throughput was maximized.

The optical heterodyne signal was obtained by projecting part of the s- and p-polarized outputs of the cavity into a single linear polarization [50] using the birefringent wave plate, W, and the polarization beam-splitter, PBS, shown in figure 8.2.

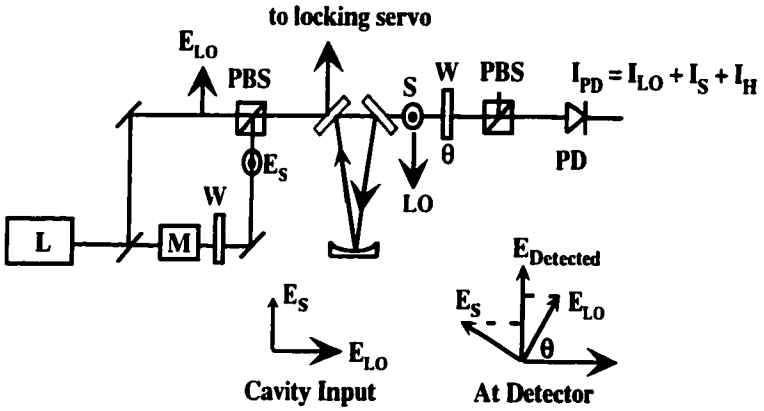

Figure 8.2: Apparatus for heterodyne detection CRDS. The RDC is described in the previous chapter.

Adjusting the wave plate varies the fractions of the s- and p-polarization amplitudes that reach the detector, and the maximum heterodyne signal level is obtained when half of each is in the detected polarization. Since both waves are emitted from TEM_{00} modes of the same cavity, optimal spatial overlap of the LO and signal is automatic. The cavity also filters out amplitude fluctuations of the PPL LO beam, but servo instability can introduce low-frequency variations in the relative phase Φ.

The photodetector consisted of an EG&G Inc. FFD-60 silicon PIN photodiode operated at 70 V bias, and an AC-coupled broadband transimpedance amplifier. An RF spectrum analyzer (HP:8590A) was used (in the linear-scaling sample-detection mode, with zero span and 3 MHz resolution and video bandwidth) as an RF detector. The center frequency was set to 282.7 MHz and the AOM frequency fine-tuned to maximize the beat signal with both waves incident on the cavity. The video output of the spectrum analyzer produced a voltage proportional to the RF heterodyne amplitude, $(I_{LO}I_{S0})^{1/2}\exp(-t/2\tau)$. That voltage was digitized and averaged using a 10-bit digital oscilloscope (Tektronix:11402), and subsequently relayed to a computer for analysis. Because the heterodyne phase Φ fluctuates owing to transient laser-cavity detuning, mixing the photodetector current with an RF local oscillator derived from the AOM electronics proved less reliable as a detection scheme.

8.2 Results and Discussion

In this case of ring-down decay signal detection, the direct detection signal is given by $I_S(t) = I_{S0}e^{-\frac{t}{\tau}}$. Under ideal conditions, the heterodyne signal amplitude is $\|I_{H0}\| = 2(I_{LO}I_S)^{1/2}$ and the heterodyne signal is

$$I_H(t) = \begin{cases} 2(I_{LO}I_{S0})^{1/2}\cos(2\pi\delta\nu t + \Phi), & t < 0 \\ 2(I_{LO}I_{S0})^{1/2}\cos(2\pi\delta\nu t + \Phi)\exp(-t/2\tau), & t > 0, \end{cases} \tag{8.2}$$

where light build-up in the cavity is stopped at $t = 0$. The exponential decay time of the heterodyne signal (which is linear in the optical amplitude of the cavity output rather than the usual amplitude square of the cavity output intensity decay) is twice that of the the direct detection ring-down intensity signal $I_S(t)$.

The initial ringdown amplitude is set by the conditions existing when the driving field is turned off, and any fluctuations that this amplitude may contribute can be normalized out. When technical noise at baseband and at the difference frequency is absent from the local oscillator beam (e.g. frequency filtering by a high finesse resonator), the electronic power signal-to-noise ratio, S/N, for heterodyne detection depends on: the heterodyne signal $I_H(t)$, the noise power of the detection system, $\eta\Delta\nu$, and the shot noise on the local oscillator, $2eI_{LO}(\Delta\nu)R$, where e is the elementary electronic charge, and R and $\Delta\nu$ are the impedance and bandwidth of the data collection system, respectively

$$S/N = \frac{< I_H^2 > R}{\eta\Delta\nu + 2eI_{LO}R\Delta\nu} = \frac{2I_{LO}I_S R}{\eta\Delta\nu + 2eI_{LO}R\Delta\nu} \tag{8.3}$$

The electrical amplitude signal-to-noise ratio is the square root of the quantity in equation 8.3. When $eI_{LO}R >> \eta$, the S/N becomes independent of the local oscillator, reaching the shot noise limit for the ring-down current:

$$S/N = I_s/(e\Delta\nu) \tag{8.4}$$

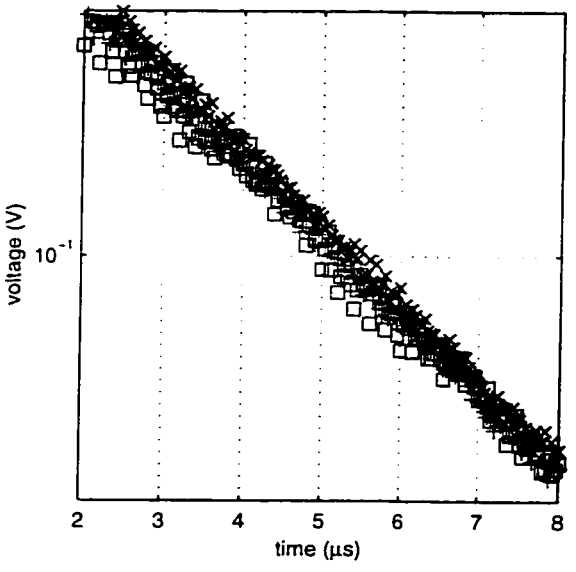

Figure 8.3: Three successive traces of the RF current amplitude on a linear scale. Note that the exponential decay of the field amplitude is twice that seen by direct detection.

Figure 8.3 shows three successive two-shot traces of the heterodyne detected ring-down current, obtained with the an optical LO power of 150 μW, and initial ring-down power of 1.8 μW at the detector. The exponential decay time of 2.2 $\pm$ 0.002 μs is twice that observed under the same conditions by direct detection [64]. The plateau for $t < 0$ permits data normalization so that fluctuations in $(I_{LO}I_{S0})^{1/2}$ can be effectively suppressed. The insert in figure 8.4 shows a 36 dB signal-to-noise ratio for this plateau for a 1 MHz resolution bandwidth. This baseline noise power at -72 dBm is due entirely to the photodetector system; at this LO power, the shot noise level would be $\sim$ 15 dB lower.

Figure 8.4 compares the square of a 256-trace averaged heterodyne-detected ring-down decay with a 256-trace averaged direct-detected decay on a semi-logarithmic plot. The square of the heterodyne current signal is proportional to the direct detection signal, and has the same decay time τ. The ring-down decay obtained via direct detection exhibits linearity over three ring-down lifetimes before becoming obscured by background photocurrent. The heterodyne power is linear over six lifetimes before

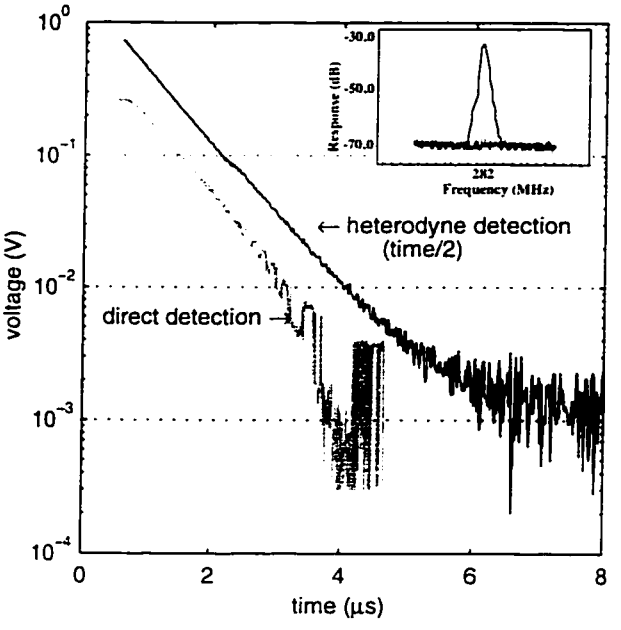

Figure 8.4: Averages of 256 ring-down decays for direct detection and heterodyne detection with time scale of the latter halved to equalize decay times. The insert show signal power levels for unoptimized single detector heterodyne detection. For direct detection, the signal did not exceed the technical noise.

plateauing at the technical noise level of the system. Since the photodetection noise, $\eta\Delta\nu$, is relatively constant in time, its level could be subtracted out, extending the linear regime. However, because of their wide dynamic range, the heterodyne signals exhibit quantization noise caused by the limited (10-bit) resolution of the digital oscilloscope. Simply upgrading the electronics would improve the sensitivity.

Figure 8.5 shows an absorption spectrum of water vapor present in ambient room air. The present sensitivity to water vapor at atmospheric pressures is about 1 part per million. The MDAL is 1.7×10^{-9} cm^{-1}, and corresponds to a MDFS of 6×10^{-5} for an average of 256 shots, i.e., a shot-to-shot fractional deviation of 1×10^{-3}. This value of MDFS is about a factor of 50 above the expected noise level for a truly shot-noise-limited measurement at this PPL power level, without quantization error.

The present single-detector heterodyne detection system wastes half of the light emanating from the cavity. A dual-differential-heterodyne-detection scheme (with photodetectors at both outputs of the polarized beam splitter, and detector outputs

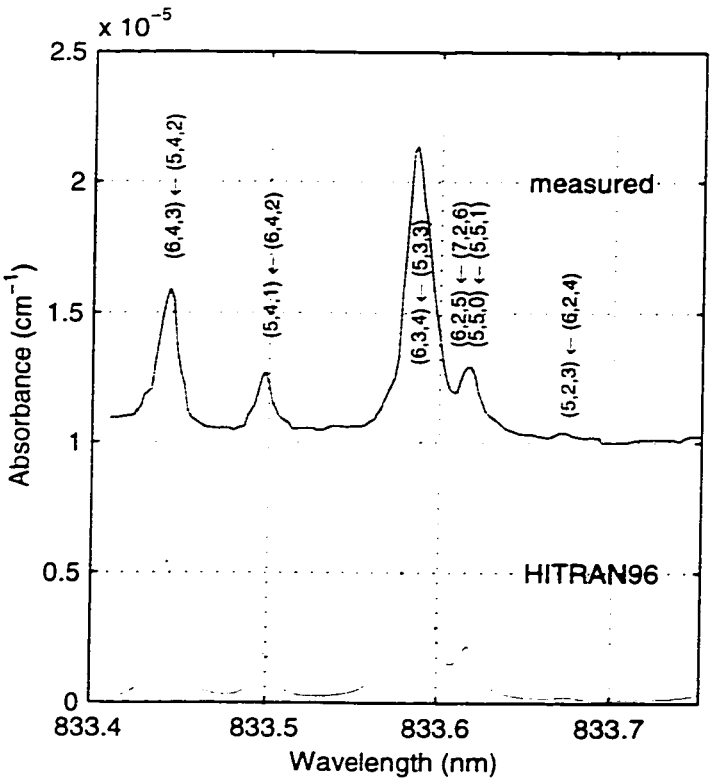

Figure 8.5: Spectrum of water vapor in room air obtained using a ECDL locked to the ring-down cavity. and single detector heterodyne detection. Spectrum based on HITRAN96 is showed in dashed lines. and transitions are indicated.

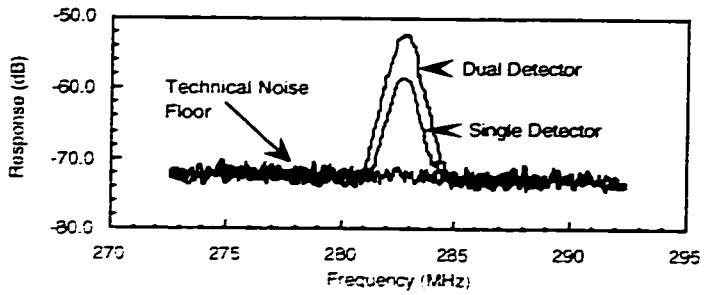

Figure 8.6: Signal-to-noise ratio of heterodyne detector signals for the single detector scheme and the dual detector schemes.

differenced electronically) collects all the light exiting the cavity, and produces twice as much ring-down current, i.e. a 6 dB increase in signal-to-noise ratio (cf. figure 8.6). When properly balanced, such a system can also reject whatever noise might be present on the LO beam [92]. We demonstrated the increase in signal in such a system, but also found an increase in technical noise (twice the number of transimpedance amplifiers), which reduced its advantage.

8.3 Summary

Polarization-selective heterodyne detection schemes proposed by Levenson *et al.* [52], and based on the locked cavity CW-CRDS setup described in chapter 7, enhance the sensitivity of cavity ring-down spectroscopy. Initial experiments have demonstrated a signal-to-noise ratio 31 dB above the detection system technical noise, and it is expected that minor refinements to the electronics should yield shot-noise-limited operation. Under shot-noise-limited conditions, the sensitivity and precision with which gas phase absorption coefficients can be measured will depend only on the cavity length and finesse. Using current mirror coating technology, it is expected that differential aborbances on the order of 10^{-13} cm^{-1} will be detected based on single-shot, millisecond-long decay waveform measurements.

Chapter 9

Conclusions

9.1 Summary

This thesis has demonstrated pioneering research in the field of cavity ring-down spectroscopy. In CRDS, a laser light source excites a high-finesse optical resonator, and we detect the light that leaks out of the resonator after the source has been extinguished, is detected. CRDS typically exploits pulsed laser sources, but two alternative schemes using continuous wave (CW) sources were demonstrated. In the first system, an acousto-optic modulator was used to stabilize the linewidth of a laser diode source in the presence of optical feedback from the resonator. Spectra of water vapor at 810 nm were obtained with a sensitivity of 200 pm in ambient air, and 20 ppm in a static gas cell at pressures of several torr, for a 10 μs decay constant. In the second system, a ring resonator was locked to an external cavity diode laser using the Pound-Drever-Hall method. Electronic locking guaranteed that only a single mode of the resonator was excited at each shot. Spectra of water vapor at 830 nm were measured witha sensitivity of 5 ppm in ambient air for a 1 μs decay constant. However, insufficient (2 μW) light throughput by the resonator precluded shot-noise-limited detection and reduced sensitivity. Therefore, an optical heterodyne detection scheme proposed by Levenson was implemented to improve CRDS signal acquisition: by mixing the signal used to lock the resonator to the laser with the exponential decay signal, and demodulating the resulting heterodyne signal, an improvement of 35 dB in

the signal level was achieved. Thus, the detected signal exceeded the technical noise of the detector, leading to a water vapor sensitivity of 1 ppm at 830 nm. Thus, CRDS evolved within the framework of this thesis research from using pulsed laser sources exciting many cavity modes, to using CW laser sources exciting several cavity modes, and finally to using CW laser sources exciting only a single mode. These system improvements resulted in a net sensitivity improvement by a factor of 400.

9.2 Future Work

The sensitivity of CRDS depends directly on the experimental ability to measure resonator losses accurately. Losses are generally determined from the exponential decay rate of light exiting the resonator after the light source is turned off. The accuracy of measuring the decay rate depends on noise superposed on the decay during its measurement, as well as the ability to 'freeze' and fit the signal to obtain the decay parameters. The amount of noise superposed on the signal depends on the quality of the detectors used: technical detector noise must be minimized, especially for small light levels, to preclude detection noise from overwhelming the signal. Alternately, light levels can be increased, such as with heterodyne detection.

9.2.1 Shot-Noise-Limited Detection

Because ring-down cavities have a high finesse, which typically entails a linewidth of 1 to 100 kHz, the linewidth of the laser source used should be as narrow as possible to maximize cavity throughput. For example, a CW Nd:YAG non-planar ring oscillator (NPRO) laser could be used to investigate transitions of CO_2. The detectors themselves should be designed to produce signals whose only noise component is the shot-noise present in the light signal itself. In fact, because shot-noise is always present in any optical signal (unless measures are taken to produce squeezed light), the best signal-to- noise (SNR) achievable in CRDS will be the shot noise SNR. If the optical signal is accurately rendered into an electronic one, then no noise should be introduced into the electronic signal during signal analysis. In particular, if the decay

constant is extracted using a logarithmic amplifier, and analog detection electronics, then these electronics must not only have low noise characteristics, but also an accurate time base. The implementation of such electronics may well prove to be the most arduous task. Alternatively, the signal can be digitized using commercial electronics. In this case, adequate temporal (horizontal) and voltage (vertical) resolution are crucial: the sample rate of the former must exceed the Nyquist sampling rate by at least a factor of 5 (to guarantee a good quality fit), while the latter should simply be made as good as possible. However, it should be noted that for truly shot-noise-limited detection, the noise introduced by digitization will almost certainly exceed the shot noise. Hence, for true shot-noise-limited detection and analysis in CRDS, digitization should be avoided completely.

9.2.2 Optical Locking

In order to enable inexpensive, portable systems, the design of a cavity ring-down spectrometer must be simplified to the basics: a laser source, an optical resonator, and a detector. Furthermore, the laser source should be a diode laser. In order to maximize light throughput for the relatively broad diode laser linewidths available, the laser should be locked to the cavity via optical feedback, which will reduce its linewidth to that the of the optical resonator, thereby maximizing cavity throughput. Once optical locking is achieved, the laser can be turned off, and the ring-down decay detected. Previous attempts by Lehmann indicated that care must be taken to ensure that the diode laser is locked to the same mode at every shot, and this could prove to be a challenge, should this approach be revisited.

9.2.3 Access to Fundamental Transitions

Most of CRDS has been performed in the UV, the visible, or the near-IR, on overtone transitions that tend to be relatively weak compared to their fundamental counterparts. Therefore, interesting extensions of CRDS to the mid-infrared should be explored. With the advent of FT-limited OPO's that can continuously tune from 3 to 5 μm, or quantum cascade lasers, which are becoming available and can tune

from 5 to 15 μm in smaller bands, operating in pulsed or CW modes, the possibilities of extending CRDS and achieving record sensitivities is slowly becoming a reality. In particular, for detection of organic molecules, be they of biological or man-made origin, benign or toxic, these laser sources will prove their utility.

9.2.4 Applications

Many different possible applications for CRDS systems are envisaged, both in industrial and research settings. The utility of CRDS for fundamental chemistry research, be it high resolution spectroscopy of weakly absorbing species, spatially resolved spectroscopy of reactants, or kinetic studies deducing rate constants, is growing as a fast rate, with new applications appearing every month in the literature. Industrially, the technique has tremendous potential for low concentration detection, be it in process control, hazardous contaminant monitoring, or quality control for chemicals entering a manufacturing plant. However, the potential of CRDS for biological and medical applications must not be underestimated: trace toxin or metabolite detection from exhaled human breath, monitoring of anaesthesiological gases during operations, and species identification at the output of gas chromatographs are all possible future CRDS applications. Finally, the application of CRDS to environmental research and monitoring should also be mentioned, that can include not only measurement of greenhouse gases in remote arctic areas, but possibly even exhaust and industrial emissions detection.

Bibliography

[1] M.C. Abrams, S.P. Davis, M.L.P. Rao, R. Engleman, and J.W. Brault. High-resolution fourier transform spectroscopy of the meinel system of oh. *Astro. J. Suppl. Ser.*, 93(1):351, 1994.

[2] G. P. Agrawal and N. K. Dutta. *Semiconductor Lasers.* VanNostrand Reinhold, New York, 1993.

[3] J. S. Ames, editor. *Prismatic and Diffraction Spectra.* Harper and Brothers, New York, 1898.

[4] K. An, C. Yang, R. R. Dasary, and M. S. Feld. Cavity ring-down technique and its application to the measurement of ultraslow velocities. *Opt. Lett.*, 20(9):1068, 1995.

[5] D. Z. Anderson, J. C. Frisch, and C. S. Masser. Mirror reflectometer based on optical cavity decay time. *Appl. Opt.*, 23(8):1238, 1984.

[6] V. M. Baev, J. Eschner, E. Paeth, R. Schüler, and P. E. Toschek. Intracavity spectroscopy with laser diodes. *Appl. Phys. B*, B55(6):463, 1992.

[7] V. M. Baev, V. F. Gamalij, B. D. Lobanov, E. F. Martynovich, E. A. Sviridenkov, A. F. Suchkov, and V. M. Khulgurov. Application of lasers utilizing color centers in alkali halide crystals to intracavity laser. *Sov. J. Quantum. Electron.*, 9:51, 1979.

[8] G. C. Bjorklund, M. D. Levenson, W. Length, and C. Ortiz. Frequency modulation (fm) spectroscopy. *Appl. Phys. B*, 32:145, 1983.

[9] R. Böhm, A. Stephani, V. M. Baev, and P. E. Toschek. Intracavity absorption spectroscopy with a nd^{+3}-doped fiber laser. *Opt. Lett.*, 18(22):1955, 1993.

[10] M. G. H. Boogaarts and G. Meijer. Measurement of the beam intensity in a laser desorption jet-cooling mass spectrometer. *J. of Chem. Phys.*, 102(13):5269, 1995.

[11] G. D. Boyd and H. Kogelnik. Resonant modes in optical cavities. *Bell. Sys. Tech. J.*, 41:1347, 1962.

[12] R. J. Cattolica. Oh radical nonequilibrium in methane-air flat flames. *Comb. Flam.*, 44:43, 1982.

[13] P. P. Cherrier and J. Reid. High-sensivity detection of tritiated water vapor using tunable diode lasers. *Nucl. Inst. Meth. Phys. Res.*, A257:412, 1987.

[14] L. A. Coldren and S. W. Corzine. *Diode Lasers and Photonic Integrated Circuits.* John Wiley and Sons, New York, 1995.

[15] E. U. Condon and G. H. Shortley, editors. *The theory of atomic spectra.* Cambridge University Press, Cambridge, UK, 1951.

[16] D. E. Cooper and R. E. Warren. Frequency modulation spectroscopy with lead-salt diode lasers: a comparison of single-tone and two-tone techniques. *Applied Optics*, 26(17):3726, 1987.

[17] W. Demtröder. *Laser Spectroscopy.* Springer Verlag, Berlin, 1996.

[18] A. M. DeRiva, G. Zavattini, S. Marigo, C. Rizzo, G. Ruoso, G. Carugno, R. Onofrio, S. Carusotto, M. Pap, F. Perrone, E. Polacco, G. Cantatore, F. Della Valle, P. Micossi, E. milotti, P. Pace, and E Zavattini. Very high q frequency-locked fabry-perot cavity. *Rev. Sci. Inst.*, 67(8):2680, 1996.

[19] G. W. F. Drake, editor. *Atomic, Molecular, and Optical Physics.* American Institute of Physics, Woodbury, NY, 1996.

[20] P. Elleaume, M. Velghe, M. Billardon, and J. M. Ortega. Diagnostic techniques and uv-induced degradationof the mirrors used in the orsay storage ring free-electron laser. *Appl. Opt.*, 24(17):2762, 1985.

[21] W. C. Elmore and M. A. Heald. *Physics of Waves.* Dover Publications Inc., New York, 1969.

[22] R. Engeln, G. Bierden, E. van den Berg, and G. Meijer. Polarization dependent cavity ring down spectroscopy. *J. Chem. Phys.*, 107(12):4458, 1997.

[23] R. Engeln and G. Meijer. A fourier transform cavity ring down spectrometer. *Rev. Sci. Instrum.*, 67(8):2708, 1996.

[24] R. Engeln and G. Meijer. Phase shift cavity ring down absorption spectroscopy. *Chemical Physics Letters*, 262(1-2):105, 1996.

[25] R. Engeln, E. van den Berg, G. Meijer, L. Lin, G. M. H. Knippels, and A. F. G. van der Meer. Cavity ring down spectroscopy with a free-electron laser. *Chem. Phys. Lett.*, 269(3-4):293, 1997.

[26] J. M. Flaud, C. Camy-Peyret, A. Bykov, O. Naumenko, T. Petrova, A. Scherbakov, and L. Sinitsa. The high-resolution spectrum of water vapor between 11600 and 12750 cm^{-1}. *J. Mol. Spec.*, 183(2):300, 1997.

[27] D. A. Gilmore, P. Vujkovic-Cvijin, and G. H. Atkinson. Intracavity absorption spectroscopy with a titanium:sapphire laser. *Opt. Comm.*, 77(5):385, 1990.

[28] C. C. Harb, M. B. Gray, H. A. Bachor, R. Schilling, P. Rottengatter, I. Freitag, and H. Welling. Suppression of the intensity noise in a diode-pumped nd:yag nonplanar ring laser. *IEEE Journal of Quantum Electronics*, 30(12):2907, 1994.

[29] J. M. Herbelin and J. A. McKay. Development of laser mirros of very high reflectivity using the cavity- attenuated phase-shift method. *Appl. Opt.*, 20(19):3341, 1981.

[30] J. M. Herbelin, J. A. McKay, M. A. Kwok, R. H. Ueunten, D. S. Urevig, D. J. Spencer, and D. J. Benard. Sensitive measurement of photon lifetime and true reflectances in an optical cavity by a phase-shit method. *Appl. Opt.*, 19(1):144, 1980.

[31] D. Herriot. Off-axis paths in spherical interferometers. *Applied Optics*, 3:523, 1964.

[32] G. Herzberg. *Molecular Spectra and Molecular Structure.* Van Nostrand, New York, 1950.

[33] J. T. Hodges, J. P. Looney, and R. D. van Zee. Response of a ring-down cavity to an arbitraty excitation. *J. Chem. Phys.*, 105(23):10278, 1996.

[34] J. T. Hodges, J. P. Looney, and R. D. vanZee. Laser bandwidth effects in quantitative cavity ring-down spectroscopy. *Appl. Opt.*, 35(21):4112, 1996.

[35] D. L. Huestis, R. A. Copeland, K. Knutsen, T. G. Slanger, R. T. Jongma, M. G. H. Boogaarts, and G. Meijer. Branch intensities and oscillator strenths for the herzberg absorption systems in osygen. *Can. J. Phys.*, 72(11-12):1109, 1994.

[36] D. Voelkel J. Scherer and D. Rakestraw. Probing flames with infrared cavity ringdown absorption spectroscopy. *Comb. Res. Fac.*, 18(4):1, 1996.

[37] C. B. Johnson. A review of ultraviolet detector technology. *Proc. SPIE*, 1243:2, 1990.

[38] R. T. Jongma, M. G. H. Boogaarts, I. Holleman, and G. Meijer. Trace gas detection with cavity ring-down spectroscopy. *Rev. Sci. Instrum.*, 66(4):2821, 1995.

[39] A. A. Kachanov, A. Charvat, and F. Stoeckel. Intracavity laser spectroscopy with vibronic solid-state laser. i. spectrotemporal transient behavior of a ti:sapphire laser. *J. OSA B*, 11(12):2412, 1994.

[40] A. A. Kachanov, A. Charvat, and F. Stoeckel. Intracavity laser spectroscopy with vibronic solid-state lasers: Ii. influence of the nonlinear mode coupling on the maximum sensitivity o f ti:sapphire laser. *J. OSA B*, 12(6):970, 1995.

[41] A. A. Kachanov, V. R. Mironenko, and I. K. Pashkovich. Quantum threshold of the sensitivity of an intracavity traveling-wave laser spectrometer. *Sov. J. Q@uant. Electron.*, 16(1):146, 1989.

[42] A. A. Kachanov, D. Romanini, A. Chavrat, Abel, and V. R. Kovalenko. Recent advances in iclas. *Pers. Comm.*, 2:1, 1997.

[43] G. R. Kirchoff. *Ann. d. Physik*, 109(148):275, 1860.

[44] M. Kotterer and J. P. Maier. Electronic spectrum of c_6h:$^2\pi$-$x^2\pi$ in the gas phase detected by cavity ringdown. *Chem. Phys. Lett.*, 266(3-4):342, 1997.

[45] H. W. Kroto. *Molecular Rotation Spectra.* Dover, New York, 1992.

[46] R. J. Lang and K. Kobayashi. *IEEE Journal of Quantum Electronics*, QE-16:347, 1980.

[47] K. K. Lehmann. Ring-down cavity spectroscopy cell using continuous wave excitation for trace species detection. *U. S. Patent*, 5 528 040, 1996.

[48] K. K. Lehmann and D. Romanini. The superposition principle and cavity ring-down spectroscopy. *J. Chem. Phys.*, 105(23):10263, 1996.

[49] L. Lehr and P. Hering. Quantitative nonlinear spectroscopy: a direct comparison of degenerate four-wave mixing with cavity ring-down spectroscopy applied to nah. *IEEE J. Quant. Electron.*, 33(9):1465, 1997.

[50] M. D. Levenson and G. L. Eesley. Polarization selective optical heterodyne detection for dramatically improved sensitivity in laser spectroscopy. *Appl. Phys.*, 19:1, 1979.

[51] M. D. Levenson and S. S. Kano, editors. *Introduction to Nonlinear Laser Spectroscopy.* Academic Press Inc., Boston, 1988.

[52] M. D. Levenson, B. A. Paldus, C. C. Harb, T. G. Spence, J. S. Harris, and R. N. Zare. Optical heterodyne detetion in cavity ring-down spectroscopy. *Opt. Lett.*, submitted december 1997.

[53] Li Li, Xingbin Xie, and Ming-Chia Lai. Temperature measurement via oh spectrum in a flat c_3h_8o-2 flame by degenerate four-wave mixing. *Opt. Las. Eng.*, 24(1):33, 1995.

[54] R. J. Maniero. Reaction mechanisms in hydrogen-nitric oxide flames. *Combust. Sci. Technol.*, 266(3-4):342, 1997.

[55] J. Martin, B. A. Paldus, P. Zalicki, E. H. Wahl, T. G. Owano, J. S. Harris Jr., C. H. Kruger, and R. N. Zare. Cavity ring-down spectroscopy with fourier-transform-limited light pulses. *Chem. Phys. Lett.*, 258(1-2):63, 1996.

[56] J. Martin, Y. Zhao, S. Balle, K. Bergmann, and M. P. Fewell. Visible-wavelength diode laser with weak frequency-shifted optical feedback. *Optics Communications*, 112:109, 1994.

[57] G. Meijer, M. G. H. Boogaarts, and A. M. Wodtke. Coherent cavity ring-down spectroscopy. *Chem. Phys. Lett.*, 217(1-2):112, 1994.

[58] H. C. Miller, J. E. McCord, J. Choy, and G. D. Hager. Measurement of the radiative lifetime of o_2 (a^delta_g) using cavity ring-down spectroscopy. In *Proceedings of the 1996 Conference on Lasers*, Portland, OR, 1996. OSA.

[59] J. H. Moore, C. C. Davis, and M. A. Coplan. *Building Scientific Apparatus: A Practical Guide to Design and Construction.* Addison-Wesley, Reading, 1989.

[60] K. Nakagawa, T. Katsude, A. S. Shelkovnikov, M. de Labachelerie, and M. Ohtsu. Highly sensitive detection of molecular absorption using a high finesse optical cavity. *Opt. Comm.*, 107(5-6):369, 1994.

[61] H. Naus, W. Ubachs, I. van Stokkum, and P. F. Levelt. Investigation of cavity ring-down transients. In American Physical Society, editor, *ILS-XII 12th Interdisciplinary Laser Science Conference*, page 122, Rochester, New York, 1996. OSA.

[62] A. O'Keefe and D. A. G. Deacon. Cavity ring-down optical spectrometer for absorption measurements using pulsed laser sources. *Rev. Sci. Inst.*, 59(12):2544, 1988.

[63] A. O'Keefe, J. J. Scherer, A. L. Cooksy, R. Sheeks, J. Heath, and R. J. Saykally. Cavity ring-down dye laser spectroscopy jet-cooled metal clusters: Cu_2 and cu_3. *Chem. Phys. Lett.*, 172(3-4):214, 1990.

[64] B. A. Paldus, C. C. Harb, T. G. Spence, J. Xie, J. S. Harris, and R. N. Zare. Cavity-locked ring-down spectroscopy. *J. Appl. Phys.*, submitted october 1997.

[65] B. A. Paldus, J. Martin, J. S. Harris, and R. N. Zare. Optimization of system parameters for a laser diode-based cavity ring-down spectrometer. in preparation.

[66] B. A. Paldus, J. Martin, J. Xie, J. S. Harris, and R. N. Zare. Laser diode cavity ring-down spectroscopy using an acousto-optic modulator. *J. Appl. Phys.*, 82(7):3199, 1997.

[67] J. B. Paul, C. P. Collier, J. J. Scherer, D. J. Rakestraw, A. O'Keefe, and R. J. Saykally. Cavity ringdown laser spectroscopy. *CLEO '96*, 9, 1996.

[68] J. Pearson, A. J. Orr-Ewing, M. N. R. Ashfold, and R. N. Dixon. Spectroscopy and predissociation dynamics of the a^1a" state of hno. *J. Chem. Phys.*, 106(14):5850, 1997.

[69] K. Petermann. *Laser Diode Modulation and Noise*. Kluwer Academic Publishers, Dordrecht, 1988.

[70] L. Pierrot. Water vapor partition function dependence on temperatur. *Private Communication*, 1(1):1, 1997.

[71] A. C. R. Pipino, J. W. Hudgens, and R. E. Huie. Evanescent wave cavity ring-down spectroscopy with a total-internal reflection minicavity. *Rev. Sci. Instr.*, 68(8):2978, 1997.

[72] S. Prucker, W. Meier, and W. Stricker. A flat flame burner as calibration source for combustion research: Temperatures and species concentrations of premixed $h_2$air flames. *Rev. Sci. Inst.*, 65(9):2908, 1994.

[73] G. Rempe, R. J. Thompson, H. J. Kimble, and R. Lalezari. Measurement of ultralow losses in an optical interferometer. *Opt. Lett.*, 17(5):363, 1992.

[74] H. Riris, C. B. Carlisle, D. E. Cooper, R. U. Martinelli, and R. J. Menna. Design of an open path near-infrared diode laser sensor: application to oxygen, water and carbon dioxide vapor detection. *Applied Optics*, 33(30):7059, 1994.

[75] D. Romanini, J. Gambogi, and K. K. Lehmann. Cavity ring down spectroscopy with cw diode laser excitation. In T. A. Miller, editor, *50th International Symposium on Molecular Spectroscopy*, page 284, Ohio State University, Columbus, Ohio, 1995. ACS.

[76] D. Romanini, A. A. Kachanov, N. Sadeghi, and F. Stoeckel. *Priv. Comm.*, 1997.

[77] D. Romanini, A. A. Kachanov, N. Sadeghi, and F. Stoeckel. Cavity ring-down spectroscopy with an external cavity diode laser. *Chemical Physics Letters*, 270(5-6):538, 1997.

[78] D. Romanini, A. A. Kachanov, N. Sadeghi, and F. Stoeckel. Cw cavity ring-down spectroscopy. *Chem. Phys. Lett.*, 264(3-4):316, 1997.

[79] D. Romanini, A. A. Kachanov, and F. Stoeckel. Cavity ring-down spectroscopy: Broad band absolute absorption measurements. *Chem. Phys. Lett.*, 270(5-6):546, 1997.

[80] D. Romanini and K. K. Lehmann. Ring-down cavity absorption spectroscopy of the very weak hcn overtone bands with six, seven, and eight stretching quanta. *J. Chem. Phys.*, 99(9):6287, 1993.

[81] D. Romanini and K. K. Lehmann. Calculation f the herman-wallis effect in π-σ vibrational overtone transitions in a linear molecule: Comparison with hcn experimental results. *J. Chem. Phys.*, 105(1):68, 1996.

[82] D. Romanini and K. K. Lehmann. Line-mixing in the 106←000 overtone transition of hcn. *J. Chem. Phys.*, 105(1):81, 1996.

[83] D. D. Romanini and K. K. Lehmann. Cavity ring-down overtone spectroscopy of hcn, $h^{1}3cn$ and $hc^{1}5n$. *J. Chem. Phys.*, 102(2):633, 1995.

[84] L. S. Rothman, R. L. Hawkins, R. B. Wattson, and R. R. Gamache. The hitran molecular database: editions of 1991 and 1992. *J. Quant. Spec. Rad. Trans.*, 48(5-6):469, 1992.

[85] J. J. Scherer, J. B. Paul, C. P. Collier, and R. J. Saykally. Cavity ring-down laser absorption spectroscopy and time-of-flight mass spectroscopy of jet-cooled silver silicides. *J. Chem. Phys.*, 103(1):113, 1995.

[86] J. J. Scherer, J. B. Paul, C. P. Collier, and R. J. Saykally. Cavity ring-down laser absorption spectroscopy and time-of-flight mass spectroscopy of jet-cooled copper silicides. *J. Chem. Phys.*, 102(13):5190, 1995.

[87] J. J. Scherer, J. B. Paul, A. O'Keefe, and R. J. Saykally. Cavity ringdown laser absorption spectroscopy: History, development, and application to pulsed molecular beams. *Chem. Rev.*, 97(1):25, 1997.

[88] J. J. Scherer, J. B. Paul, and R. J. Saykally. Cavity ring-down laser absorption spectroscopy of jet-cooled aluminum dimer. *Chem. Phys. Lett.*, 242:395, 1995.

[89] J. J. Scherer and D. J. Rakestraw. Cavity ringdown laser absorption spectroscopy detection of formyl (hco) radical in a low pressure flame. *Chem. Phys. Lett.*, 265(1-2):169, 1997.

[90] J. J. Scherer and D. J. Rakestraw. Determination of methyl radical concentrations in a methane/air flame by infrared cavity ring-down laser absorption spectroscopy. *J. Chem. Phys.*, 107(16):6196, 1997.

[91] J. J. Scherer, D. Voelkel, D. J. Rakestraw, J. B. Paul, C. P. Collier, R. J. Saykally, and A. O'Keefe. Infrared cavity ringdown laser absorption spectroscopy (ir-crlas). *Chem. Phys. Lett.*, 245(2-3):273, 1995.

[92] B. L. Schumaker. Noise in homodyne detection. *Opt. Lett.*, 9:189, 1984.

[93] V. Sick, M. N. Bui-Pham, and R. L. Farrow. Detection of methyl radicals in a flat flame by degenerate four-wave mixing. *Opt. Lett.*, 20(19):2036, 1995.

[94] A. E. Siegman. *Lasers.* University Science Books, Mill Valley, CA, 1986.

[95] O. H. W Siegmund, M. A. Gummin, J. Stock, and D. Marsh. Detection of photons. In T. D. Guyenne and J. Hunt, editors, *Photon Detectors for Space Instrumentation*, volume ESA SP-356, page 356, Paris, 1992. European Space Agency.

[96] J. A. Silver and D. C. Hovde. Near-infrared diode laser airborne hygrometer. *Rev. Sci. Inst.*, 65(5):1691, 1994.

[97] K. Singh and J. J. O'Brien. Intensities and self-broadening coefficients of weak water vapor lines in the 720-nm region determined by intracavity laser absorption spectroscopy. *J. Mol. Spec.*, 99(1):167, 1994.

[98] T. G. Slanger, D. L. Huestis, P. C. Cosby, H. Naus, and G. Meijer. O_2 photoabsorption in the 40950-41300 cm^{-1} region: new herznerg band, new absorption lines and improved spectroscopic data. *J. Chem. Phys. A*, 105(21):9393, 1996.

[99] T. G. Spence, B. A. Paldus, C. C. Harb, R. L. Byer, and R. N. Zare. Locked-laser cavity ring-down spectroscopy. *J. OSA B*, (in preparation), 1998.

[100] F. Stoeckel, M.-A. Melieres, and M. Chenevier. Quantitative measurements of very weak h_2o absorption lines by time resolved intracavity laser spectroscopy. *J. Chem. Phys.*, 76(5):2192, 1982.

[101] R. A. Toth. Measurements of $h_2^{16}o$ line positions and strengths: 11610 to 12861 cm^{-1}. *J. Mol. Spec.*, 166(1):176, 1994.

[102] C. H. Townes and A. L. Schawlow, editors. *Microwave Spectroscopy.* Dover Publications, New York, 1975.

[103] G. Tsatsaronis. Prediction of propagating laminar flames in methane, oxygen, nitrogen mixtures. *Comb. Flam.*, 33:217, 1978.

[104] A. Ueda, N. Uehara, K. Uchisawa, and et al. Ultra-high quality cavity with 1.5 ppm loss at 1064 nm. *Optical Review*, 3(5):369, 1996.

[105] L. A. Vainshtein. *Open resonators and open waveguides.* Golem Press, Boulder, CO. 1969.

[106] G. Vanasse, editor. *Spectrometric Techniques*, volume IV. Academic Press, New York, 1985.

[107] S. E. Vinogradov, A. A. Kachanov, S. A. Kovalenko, and E. A. Sviridenkov. Nonlinear dynamics of a multimode dye laser with an adjustable resonator diespersion and implications for the sensitivity of in-resonator laser spectroscopy. *JETP Lett.*, 55(10):581. 1992.

[108] E. H. Wahl, T. G. Owano, C. H. Kruger, Y. Ma, P. Zalicki, and R. N. Zare. Spatially resolved measurements of absolute ch_3 concentration in a hot-filament reactor. *Diam. Rel. Mat.*, 6(2-4):476, 1997.

[109] E. H. Wahl, T. G. Owano, C. H. Kruger, P. Zalicki, Y. Ma, and R. N. Zare. Measurement and absolute ch_3 concentration in a hot-filament reactor using cavity ring-down spectroscopy [diamond cvd]. *Diam. Rel. Mat.*, 5(3-5):373, 1996.

[110] R. Waynant and M. Ediger, editors. *Electro-Optics Handbook.* McGraw Hill, New York, 1994.

[111] Richard J. Weiss. *A Brief History of Light, and Those That Lit the Way.* World Scientific, Singapore, 1996.

[112] M. D. Wheeler, A. J. Orr-Ewing, M. N. R. Ashfold, and T. Ishiwato. Predissociation lifetimes of the $a^2\sigma^n u = 1$ state of the sh radical determines by cavity ring-down spectroscopy. *Chem. Phys. Lett.*, 268(5):421, 1997.

[113] J. U. White. Very long optical paths in air. *J. Opt. Soc. Amer.*, 66(5):411, 1976.

[114] J. Xie, B. A. Paldus, E. H. Wahl, J. Martin, T. G. Owano, C. H. Kruger, J. S. Harris, and R. N. Zare. Near-infrared cavity ringdown spectroscopy of water vapor in an atmospheric flame. *Chem. Phys. Lett.*, accepted November 1997.

[115] A. Yariv. *Quantum Electronics.* John Wiley and Sons, New York, 1989.

[116] J. Ye, L. S. Ma, and J. L. Hall. Sub-doppler optical frequency reference at 1.064 μm by means of ultrasensitive cavity-enhanced frequency modulation spectroscopy of a $c_2$hd overtone transition. *Opt. Lett.*, 21(13):1000, 1996.

[117] T. Yu and M. C. Lin. Kinetics. *J. Amer. Chem. Soc.*, 115:4371, 1993.

[118] P. Zalicki, Y. Ma, R. N. Zare, E. H. Wahl, J. R. Dadamio, T. G. Owano, and C. H. Kruger. Methyl radical measurement by cavity ring-down spectroscopy. *Chem. Phys. Lett.*, 234(4-6):269, 1995.

[119] P. Zalicki, Y. Ma, R. N. Zare, E. H. Wahl, T. G. Owano, and C. H. Kruger. Measurement of the methyl radical concentration profile in a hot-filament reactor. *Appl. Phys. Lett.*, 67(1):144, 1995.

[120] P. Zalicki, Y. Ma, R. N. Zare, E. H. Wahl, T. G. Owano, and C. H. Kruger. Measurement of the methyl radical concentration profile in a hot-filament reactor. *Appl. Phys. Lett.*, 67(1):144, 1995.

[121] P. Zalicki and R. N. Zare. Cavity ring-down spectroscopy for quantitative absorption measurements. *J. Chem. Phys.*, 102(7):2708, 1995.

[122] L. Zhu and C. F. Ding. Photolysis of glyoxal at 193, 248, 308, and 351 nm. *Chem. Phys. Lett.*, 257(5):487, 1996.

[123] L. Zhu and C. F. Ding. Temperature dependence of the near uv absorption spectra and photolysis products of ethyl nitrate. *Chem. Phys. Lett.*, 265(1):177, 1997.

IMAGE EVALUATION TEST TARGET (QA-3)

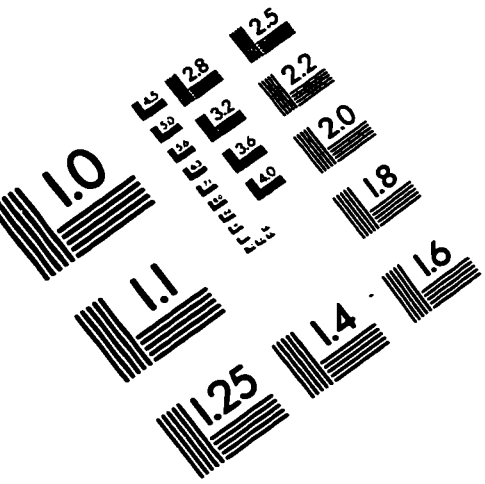

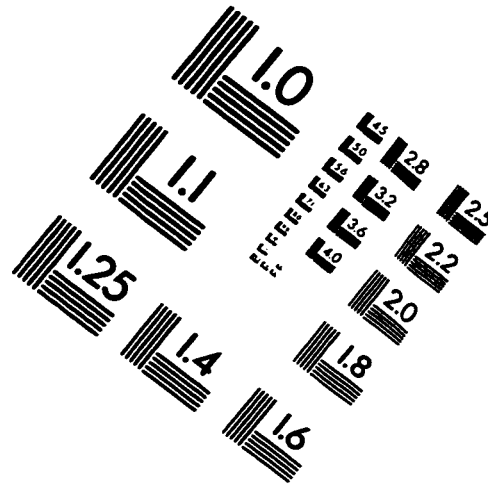

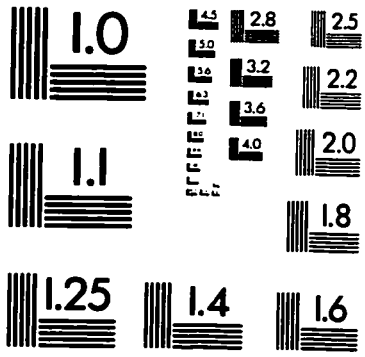

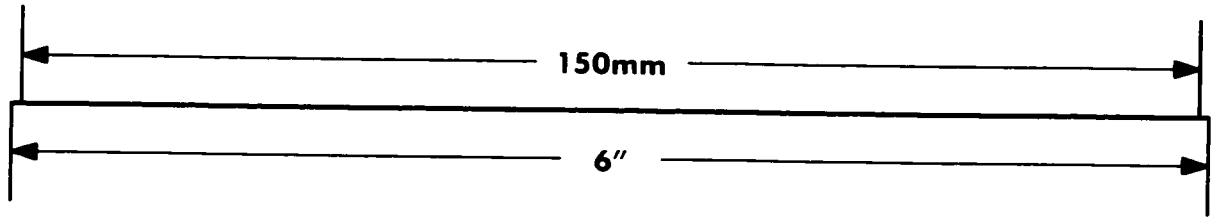

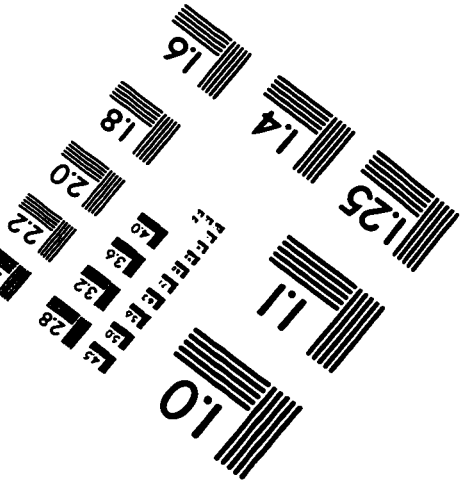

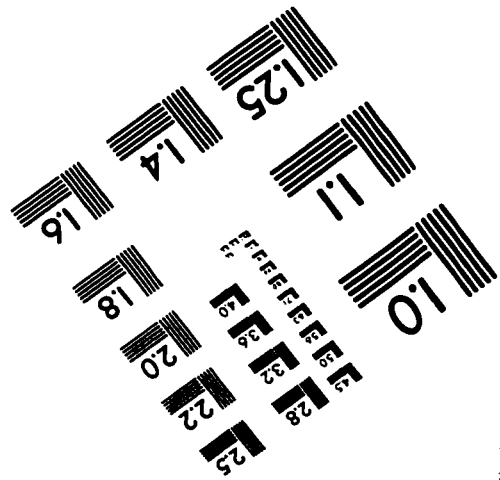

APPLIED IMAGE, Inc
1653 East Main Street
Rochester, NY 14609 USA
Phone: 716/482-0300
Fax: 716/288-5989

© 1993, Applied Image, Inc., All Rights Reserved